THE UNIVERSITY OF HULL

Numerical Simulation of Noise Attenuating Perforated Combustor Liners and the Combustion Instability Issue in Gas Turbine Engines

being a Thesis submitted for the Degree of Doctor of Philosophy

in the University of Hull

by

Jianguo Wang, B.Eng.

January 2017

Abstract

Combustion instability represents a significant problem in the application of low emission lean premixed combustion for gas turbines and has become one of the primary concerns in modern gas turbine industry. Effusion cooling has become common practice in gas turbine combustors and when calibrated, perforated combustor liners are able to attenuate combustion instability within a wide frequency range. However, the acoustic attenuation effect of perforated liner absorbers varies with a considerable number of flow and geometry influencing factors. The traditional approach of designing perforated combustor liners relies heavily on expensive and lengthy trial-and-error experimental practice. Computational fluid dynamics (CFD), especially large eddy simulation (LES) method has gained recognition as a viable tool for the simulation of unsteady flows and the phenomenon of combustion instability in gas turbine combustors. However, detailed resolution of the many small scale features, such as effusion cooling holes, is computationally very expensive and restricts the routine simulation of detailed engine geometries.

In this thesis, a novel homogenous porous media model is proposed for the simulation of acoustic attenuation effect of gas turbine perforated liners. The model is validated against a number of well-acknowledged experiments and is shown to be able to predict acoustic attenuation properties of gas turbine liners both in the linear and non-linear absorption regimes and also the effect of bias flow, grazing flow and the temperature of flow on the acoustic properties of the liners. The model is applied to a large eddy simulation of a lab-scale premixed combustor "PRECCINSTA" and is demonstrated to successfully represent noise attenuation effects of perforated liner absorbers in both cold flow and reacting flow conditions. This model is able to provide a significant reduction in the overall computational time in comparison to directly resolved geometries, and can be applied as such a viable option for routine engineering simulation of perforated combustor liners.

Keywords: Perforated Liner; Porous Media Model; CFD; Gas Turbine Combustion Instability.

Acknowledgement

First, I would like to express my sincere appreciation to my supervisor Professor Philip Rubini. This thesis would be impossible without his careful academic guidance and kind financial support. I am grateful to him also for offering me this chance of study four years ago and having allowed me a liberal research environment since then. The research under his supervision has been helpful in many ways.

Thanks are given to Dr. Qin Qin and all my other colleagues. The solid theory background and the rigorous academic attitude in Dr. Qin Qin greatly benefited my theory learning and experimental work. The easy-going and cooperative working atmosphere thanks to all other colleagues is one important reason why the last four years have been such a pleasant experience.

I would also like to thank my parents that they are healthy, persevering and have always been so encouraging. Only with their spiritual support and inspiration could I have been able to fully concentrate on this work. Appreciation also goes to all my friends who enriched my everyday life regardless of by playing football with me or by arranging those trips to this beautiful country.

Last but not least, please allow me to express my gratitude to the University of Hull and China Scholarship Council for their generous financial support, without which I would not be able to start this research at the beginning.

Contents

List of Symbols

Latin Letters

A	Area of an Orifice
c	Speed of Sound
C_b	Bias Flow Resistance Coefficient
C_d	Discharge Coefficient
C_g	Grazing Flow Resistance Coefficient
C_i	Inertial Resistance
C_v	Viscous Resistance
d	Diameter of Perforation
D	Separation Distance between Orifice Centre Lines
D_T	Diameter of a Impedance Tube
E	Acoustic Energy
f	Frequency
$G(x, x', \Delta)$	Filter Function
h	Total Enthalpy
He	Helmholtz Number
J_m	Bessel Funciton of the First Kind of Order m
k	Wave Number
K_m	Modified Bessel Function of the Second Kind of Order m
k_s'	Stokes Wave Number
K_R	Rayleigh Conductivity
K_{R0}	Rayleigh Conductivity without Presence of Mean Flow
K_{RJ}	Jing-modified Rayleigh Conductivity
l	Length of a Tube
l_c	Depth of Cavity
l_e	End correction length
l_{eff}	Effective Thickness
l_{thic}	Thickness of a Liner
L_i	i_{th} Mode of Acoustic Energy Loss
M	Mean Flow Mach Number Through an Orifice

$\mathrm{M_b}$	Bias Flow Mach Number
$\mathrm{M_g}$	Grazing Flow Mach Number
p	Acoustic Pressure
p'	Turbulent Pressure Fluctuation
$\hat{p}$	Instantaneous Pressure
p_0	Static Pressure
P	Pressure
P	Acoustic Signal Amplitude
q'	Heat Release Rate Oscillation
$\hat{q}$	Instantaneous Volume Flow Rate
Q	Absorption Quality Factor
Q	Resonance Parameter
r_0	Radius of Perforations
r	Normalzied Specific Acoustic Resistance
r_b	Bias Flow Induced Normalzied Specific Resistance
r_g	Grazing Flow Induced Normalzied Specific Resistance
$r_{\mathrm{g-b}}$	Normalzied Specific Resistance in Combined Flow Cases
R	Reflection Coefficient
Re	Reynolds Number
R_s	Orifice Surface Resistance
Sh	Shear Number
St	Strouhal Number
$\mathrm{St_{ac}}$	Acoustical Strouhal Number
S_ϕ	Source Term for the Transport Equation of Scalar ϕ
s_l	Area of Perforated Liner Surface
S_p	Momentum Source Term due to Porous Media Model
s_p	Cross-sectional Area of Flow Duct
t	Time
T	Transmission Coefficient
T	Temperature
U_{sup}	Superficial Velocity

u, v, w	Velocity Components in x, y, z Directions
$\vec{u}$	Velocity Vector
u_i	Velocity in Direction i
U	Overall Flow Velocity in Orifices
U_{ac}	Acoustic Particle Velocity in Orifices
U_b	Mean Bias Flow Velocity in Orifices
V	Volume
x	Normalized Specific Acoustic Reactance
z	Normalized Specific Acoustic Impedance
z_n	Normalized Acoustic Impedance
Z	Specific Acoustic Impedance
Z_c	Characteristic Acoustic Impedance
Z_q	Acoustic Impedance

Greek Letters

α	Absorption Coefficient
α	Permeability of Porous Material
γ	Inertia of an Orifice
δ	Resistance Term in Rayleigh Conductivity
δ	Boundary Layer Thickness Displacement
ε	Turbulent Energy Dissipation Rate
σ	Porosity
θ	Perforation Angle
κ	Turbulent Kinetic Energy
μ	Dynamic Viscosity of Air
μ_{eff}	Turbulent Effective Viscosity
ν	Kinematic Viscosity of Air
ν'	Effective Kinematic Viscosity
π	Mathemetical Constant
ρ	Denstiy of Air
τ_{ij}	Viscous Stress
ψ	Fok's Function

ϕ	Diameter
ϕ	General Scalar in Navier-Stokes Equations
ϕ	Fuel/Air Equivalence Ratio
ω	Angular Frequency
Γ	General Diffusion Coefficeint
Δ	Change of Magnitude
Δ	Cut-off Width of Large Eddy Simulation Filter

Subscripts

1,2	Microphones 1 and 2
+, -	Positive, Negative Direction
ac	Acoustical
b	Bias Flow
c	Cavity
d	Downstream
eff	Effective
g	Grazing Flow
reson	Resonance
sup	Superficial
u	Upstream

Mathematical Operations

div	Divergence of a Vector
exp	Exponential Operator
grad	Gradient of a Scalar
RMS	Root Mean Square
Σ	Sum

1. Introduction and Review

1.1 Background Review

The combustion process in a gas turbine engine converts chemical energy of the fuel into kinetic and thermal energy of the flue gas. The flue gas of high momentum and temperature is then passed through a turbine to provide shaft power for electricity generation in power plants or work as the propulsion sources for ships, vehicles and aircrafts. While the academic principle of energy conversion is easy to understand, practical issues exist for a gas turbine engine to achieve stable and enduring performance. The inferior durability of engine parts when exposed to a high temperature environment and thermo-acoustic instabilities are two of the primary concerns among these problems.

The lifespan of combustor walls and downstream turbine blades is limited by the effect of creep due to constant exposure at high temperature reacting flow conditions up to 1800K-2000K (Zhu et al., 1999; Eliaz et al., 2002). To mitigate this problem, one useful approach is to apply thermal barrier coating to the surface of high temperature parts (Padture et al., 2002; Gleeson, 2006). Another technique widely applied in industry is to make perforations on the combustor walls through which cool air is injected into the combustor. An air cooling film is thereby formed to prevent direct contact of the combustor wall with high temperature reacting flows. Cooling air is readily obtained by bleeding from the turbo engines bypass air flows (Eckert, 1984; Dowling & Stow, 2003).

In addition to the adverse creep effect at high temperatures, the lifespan and performance stability of a turbine engine can be seriously damaged by the thermal-acoustic instability issues in the combustor. Figure 1 provides an example of an annular combustor which has been seriously damaged by mechanical vibrations due to the large amplitude thermo-acoustic oscillations in the combustion chamber (Goy et al., 2005). Thermo-acoustic instability is caused by a close coupling between unstable flow dynamics and the acoustic field in the combustion chamber. The coupling mechanism is described in Figure 2 (Rayleigh, 1878; Putnam & Dennis,

1953; Zinn & Lieuwen, 2005). It consists of the following sequence of events: First, perturbations in the local fuel/air mixture ratio due to unsteady flow fields bring about heat release rate changes near the reaction zone. Then, Flow unsteadiness and heat release variations set off acoustical pressure oscillations in the combustion chamber. The acoustic wave then travels downstream and is bounced back by the boundaries of the combustor to the core reaction zone and in turn impacts on local heat release rates and turbulent flow dynamics. Pressure fluctuations accumulate in the combustion chamber when interactions between unsteady flow dynamics, acoustical oscillations and unstable heat release rate synchronize and enhance each other. The combustor pressure spectrum in an incidence of combustion instability often features a strong peak in the frequency domain. Large amplitude pressure oscillations are likely to cause serious engine vibration if they takes place near one of the natural acoustical modes of the combustor system (Lieuwen & Yang, 2005; Zinn & Lieuwen, 2005).

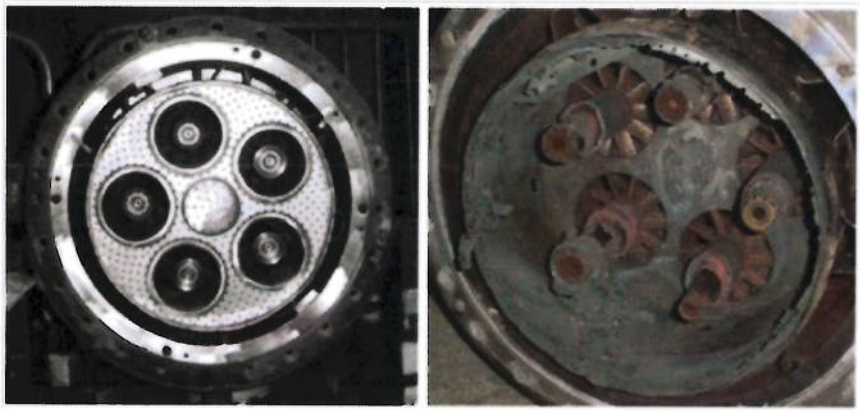

Figure 1 An annular combustor damaged by combustion instability issue

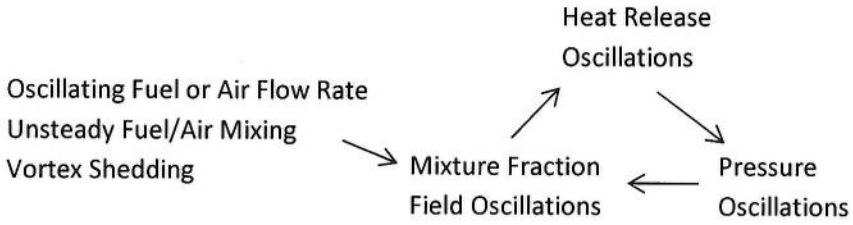

Figure 2 Feedback loop responsible for the development of combustion instability(Zinn & Lieuwen, 2005)

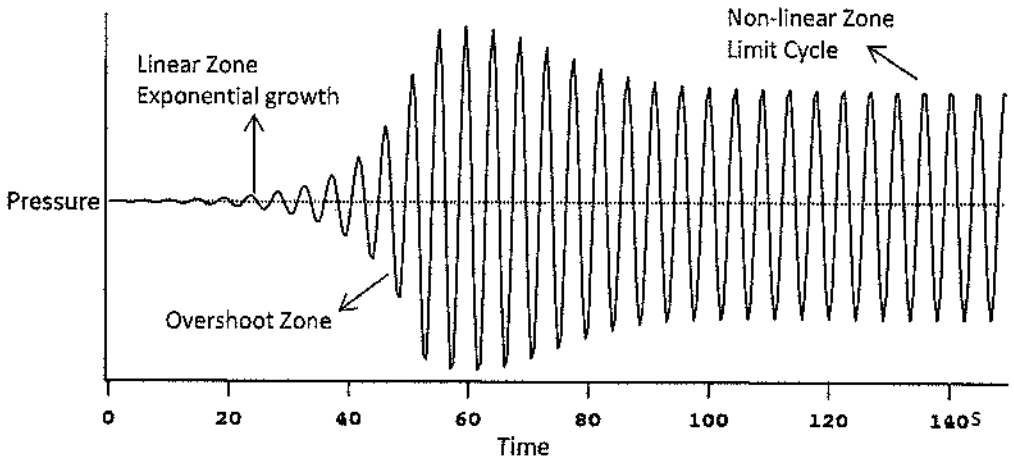

Figure 3 Evolution of the pressure oscillations in a combustor in the event of combustion instability (Zinn & Lieuwen, 2005)

Putnam et al. (Putnam & Dennis, 1953; Lieuwen, 2002) quantified the criteria and proposed that for a combustion instability to develop and sustain:

$$\iint p'(x,t)q'(x,t)\,\mathrm{d}t\mathrm{d}V \geq \iint \sum L_i(x,t)\mathrm{d}t\mathrm{d}V \qquad (1)$$

Where $p'(x,t)$,$q'(x,t)$, t, V, $L_i(x,t)$, are the transient pressure oscillation strength, heat release rate oscillation strength, period of the oscillation, combustor volume, and the i_{th} mode of acoustic energy loss respectively. The integration result on the left hand side of Equation (1) represents the net energy added to the acoustic field by the thermo-acoustic coupling, and the right hand side represents the total energy dissipated by acoustic energy dampers. Thermo-acoustic oscillation will be amplified if the energy being added to the acoustic field exceeds that being removed, and the amplification will not stop until the balance between the energy gain and the energy loss is attained in the combustor. The sustainable large amplitude pressure oscillation is referred to as "limit cycle combustion instability" by Lieuwen (2002) as shown in Figure 3. If the loss term is not sufficient, the amplitude of pressure oscillations might grow until the structure of the combustor fails.

A number of experimental investigations (Lieuwen et al., 1998; Lieuwen & Yang, 2005; Huang & Yang, 2009) have found that the lean premixed combustion process

is more susceptible to combustion instability issues. This is because that same magnitude of variation in the mixture fraction tends to lead to a larger variation in the heat release rate for leaner premixed combustion process than that for richer fuel/air ratio. Stronger heat release fluctuation then triggers pressure oscillation of larger amplitudes. Regardless of its susceptibility to combustion instability issue, lean premixed combustion technology however, could noticeably reduce NOx emissions thanks to the lower temperatures in the reaction zone (Lefebvre, 2010). Lean premixed combustion approach is therefore the preferred future combustion technology in order to meet the ever more stringent NOx emission restrictions (Lieuwen & Yang, 2013). The rising industrial preference of lean premixed combustion approach in turn brings the controlling of the combustion instability problem under more intensive research efforts since the last decade (Huang & Yang, 2009).

It is also worthwhile to note that while combustion instability takes place more often in lean premixed combustion reactors, it is however not an uncommon problem in other engines such as rocket engines, ramjet engines, aftercombustor of turbojet engines (Bloxsidge et al., 1988; Culick & Yang, 1995; Culick & Kuentzmann, 2006). Even the industrial furnaces and the flue gas exit of motor engines could be badly affected by instability problems provided that the energy feeding loop between unsteady flow dynamics and acoustic field is sustained (Barrere & Williams, 1969; Culick & Yang, 1995; Dowling & Morgans, 2005; Lahiri, 2014). Large amplitude pressure oscillation is thus a common concern and practical noise attenuating devices have to be applied in order to achieve durable and steady performances of these configurations.

Two measures are applied in gas turbine industry to dissipate large amplitude pressure oscillations in gas turbine combustors: active control measures and passive control measures (Paschereit et al., 1998; Candel, 2002). Active control is to interrupt the accumulation of pressure oscillations by cutting off the acoustic energy gain due from unsteady flow dynamics (Poinsot et al., 1989; Candel, 1992; McManus et al., 1993). This strategy is often achieved by modulating the fuel supply when large pressure oscillation in the combustor is captured by the pressure

sensors. Active control has achieved satisfactory instability attenuation effect in some lab-scale tests (Annaswamy & Ghoniem, 2002; Bothien et al., 2008). However, active control systems are sophisticated to design, expensive to configure and high system robustness is hard to achieve when it comes to their applications in some real turbines engines (Cohen & Banaszuk, 2003; Scarpato, 2014).

In addition to active control methods, there exist two commonly applied passive control devices, namely Helmholtz resonators and perforated combustor liner absorbers (Steele et al., 2000; Noiray et al., 2007; Zhao & Morgans, 2009; Zhao & Li, 2015). These two devices attenuate acoustic energy thanks to the acoustic impedance mismatch between solid wall structures and void perforation regions on the combustor walls. Helmholtz resonators, when calibrated, are able to achieve strong attenuation effect near their resonance frequencies. However, attenuation bandwidth due to Helmholtz resonance effect is often very narrow. Multi-resonators are required to attenuate noises of wide frequency range (Bellucci et al., 2001; Zhao & Morgans, 2009). In addition, the extra size and weight required by Helmholtz resonators renders it less cost-effective or even impossible to be configured on those compact engines such as military aircrafts engines.

By contrast, the perforated combustor liner, as exemplified by Figure 4, is frequently employed for the purpose of wall cooling and secondary air supply. Therefore, application of perforated liner absorber takes little extra space and weight. In addition, attenuation of noise by perforated liner absorbers takes place within a much wider frequency range compared with the single-neck Helmholtz resonators thanks to the stronger acoustic resistance of those small perforations and the inertial resistance of transverse cooling flows (Jing & Sun, 1999; Dowling & Stow, 2003; Lahiri, 2014).

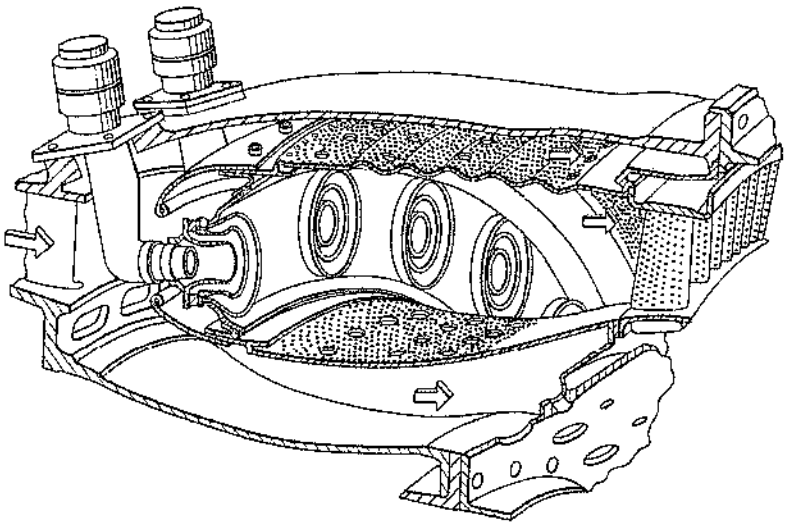

Figure 4 An annular premixed swirler combustor configured with the effusion cooling liner, designed by GE (Farmer et al., 2003)

There exist a large number of literatures studying how acoustic properties of perforated liners are affected by a variety of flow and geometry factors. Important geometry factors include perforation rate (Grace et al., 1998; Lee & Kwon, 2004; Jung et al., 2007), perforation shape and size (Ronneberger, 1972; Chanaud, 1994; Grace et al., 1998; Ahuji & Gaeta Jr, 2000; Laurens et al., 2013), liner thickness (Jing & Sun, 1999; 2000) and cavity geometry (Liu & Herrin, 2010; Rupp et al., 2012; Zhao et al., 2015). Important flow parameters include sound pressure level (Ingard & Ising, 1967; Jing & Sun, 2002; Tayong et al., 2010), bias flow speed, grazing flow speed and simultaneous bias/grazing flows (Kirby & Cummings, 1998; Jing & Sun, 1999; Jing et al., 2001; Sun et al., 2002; Eldredge & Dowling, 2003; Medeiros, 2015), and also the temperature of acoustic signals and grazing flows (Elnady et al., 2004; Rademaker et al., 2011; R.Kabral, 2014).

Despite the large number of existing literatures, most of these works have focused on only one or two of these numerous influencing factors. Experimental setups and the ranges of investigated factors are often quite different across different experiments as well. In addition, the noise attenuation performance of a perforated liner is not only decided by the perforated liner itself, it is also dependent upon periphery acoustic boundary conditions, the dimension of perforated liners in relation to the noise propagation ducts (Eldredge & Dowling, 2003) and the signal

incident angle as well (Liu, 2011). As a consequence, the acoustic properties of a perforated liner absorber require to be experimentally tested on a case by case basis. Neither a universal empirical model is possible to be able to predict acoustic properties a perforated liner in various conditions.

Lahiri (2014) is one of the few people who experimentally investigated nearly all the influencing factors for a number of perforated liners. He found that acoustic attenuation properties of these perforated liners was largely determined by only three parameters, namely, bias flow Mach number M_b, porosity σ and zero flow Helmholtz resonance frequency f_{reson}. Grazing flow could alter the attenuation effect of these liners only if it was more than three times faster than the bias flow. Perforation geometry details such as orifice cross section shape and perforation pattern was found to have fairly weak influence on the overall attenuation effect without the presence of mean bias flow and their influence was further reduced to inappreciable levels in the presence of mean bias flow. Similar finding of the very minor effects of perforation details has been confirmed by a number of other researchers as well (Chanaud, 1994; Grace et al., 1998; Ahuji & Gaeta Jr, 2000; Andreini et al., 2012; Gaeta & Ahuja, 2016).

1.2 Motivations

The fast expanding computational resources in the last two decades have significantly boosted the application of numerical experiments to reduce the cost and time required by real experiments. An obvious example is the increasing application of computational fluid dynamics (CFD) method. CFD method has unique advantages over experimental method in terms of flow variable "measurement" in harsh environments such as in transonic flows (MacManus & Doran, 2008; Stankowski et al., 2016) or reacting flows in engine combustors (Roux et al., 2005; Gicquel et al., 2012). On the other hand, CFD method often involves modelling approximations such as those for turbulence and combustion. Its validity in solving a certain type of fluid dynamics problems has to be established before its large scale application. However, CFD method received very little validation and

application effort in the investigation of acoustic properties of the perforated liners until some recent works emerged.

Most of the existing CFD investigations managed to obtain the acoustic properties of lab-scale perforated liners by resolving the exact geometries of those perforations in the liner (Boudier et al., 2007; Dassé et al., 2008; Mazdeh, 2012; Zhang & Bodony, 2012; Liu & Ji, 2014; Scarpato, 2014; Fan & Guo, 2016). However, there are often hundreds or thousands of small holes in a real gas turbine perforated liner. Resolving every single hole is computationally too expensive and the required computational time will be even longer if reacting swirling flow is involved. Some other authors resolved one individual perforation region and simply applied periodical boundary conditions in between neighbouring perforation regions (Dassé et al., 2008; Mendez & Eldredge, 2009). However, periodical boundary condition is not applicable to simulate the highly transient swirling flows in real gas turbine combustors. Therefore, while the method of resolving real holes is theoretically achievable (Scarpato, 2014; Zhao et al., 2015), it is not a feasible option for the full simulation of real gas turbine combustor perforated liners due to the excessive computational cost.

In addition to resolving every individual perforation, treating the perforated liner as a homogenous boundary is theoretically applicable thanks to the aforementioned finding by Lahiri et al (Chanaud, 1994; Grace et al., 1998; Ahuji & Gaeta Jr, 2000; Andreini et al., 2012; Lahiri, 2014; Gaeta & Ahuja, 2016) that perforation details such as perforation pattern and orifice shapes display minor impact on the overall acoustic impedance of a liner surface.

Mendez and Nicoud (2008) proposed a homogenous model where a perforated plate was treated as two disjoint homogeneous boundaries and the pressure drop due to bias flow was accounted for by the discharge coefficient of the liner. This method was later refined (Mendez & Eldredge, 2009) so that time-dependent acoustic phenomenon was accounted for by including a reactance term. Jourdain and Eriksson (2014) numerically analysed the flow governing equations in the vicinity of the holes and proposed another 'dynamic porous wall' model. Acoustic

results of the liners from this numerical model matched those from large eddy simulation resolving exact hole geometries. However, acoustic resistance in these models is in effect manually imposed by defining the discharge coefficient of the perforated liners. The discharge coefficient of a perforated liner varies with a number of geometry and flow parameters and thus has to be tuned accordingly. Besides, integration of these numerical models into CFD packages requires modifications of the governing equations within the perforated liner region which is not readily realisable in engineering practice. In addition, these models are currently only applicable to single phase non-reacting flows.

Acoustic impedance of a liner is the ratio of transient pressure difference to the resultant neck particle velocity due to this pressure difference. A flow experiences pressure loss through orifices and the pressure drop is attributable to two sources of resistance effect (Crandall, 1954), namely inertial flow resistance and viscous flow resistance. Therefore, acoustic impedance of perforated liners is achievable only if a homogenous model is able to represent the inertial and viscous resistance a flow is subjected to across the perforations.

1.3 Objectives and Outlines

In this work, a novel porous media model will be proposed and applied to treat the perforated liner as a homogenous flow region. The underlying numerical principle of this model will be analysed and the methodology of how to define the porous media region will be provided. It will be demonstrated that this porous media model is able to significantly reduce the computational cost by substantially reducing the number of meshes acquired in the liner region. The novelty and objective of this research is to validate that the proposed porous media model is able to obtain acoustic properties of perforated liners in a variety of liner geometry and flow conditions. To achieve this objective, effects of a number of significant influencing factors on acoustic properties of perforated liners are reproduced and compared with the results from a number of well-acknowledged experiments and specifically self-designed experiments as well.

Firstly, some important Rayleigh conductivity and acoustic impedance models and experimental measurement strategies are briefly reviewed in Chapter 2. These reviewed models and experimental methods will either be applied for the purpose of CFD validations or have been the cornerstones of past study in this area. Methodologies about how to define CFD calculations and how to impose relevant properties for the proposed porous media region are elaborated in Chapter 3. Validation of the proposed methodology against experimental results starts from Chapter 4 and ends in Chapter 7. Validity of the proposed CFD method is firstly looked into in terms of obtaining the acoustic properties of perforated panel absorbers without the presence of mean flow in Chapter 4. Then, effects of bias flow on the acoustic attenuation performance of liners are reproduced and compared to a few well-acknowledged experiments in Chapter 5. Chapter 6 reports the effects of grazing flow, temperature of the flow and simultaneous bias/grazing flow on acoustic impedance of perforated liners. In Chapter 7, large eddy simulation method is tested in terms of its capability in capturing the self-excited pressure fluctuation modes in the lab-scale gas turbine combustor "PRECCINSTA". The proposed porous media model is then applied to represent the perforated combustor liners and its capability in capturing noise attenuation effect of those perforated liners in swirling flow conditions is tested. Findings from each chapter are finally summarized in Chapter 8 along with the perspectives and outlook of this research work.

2. Review of Modelling and Experimental Strategies

Early study of acoustic properties of perforated liners started with investigations into acoustic conductivity or impedance of perforated liners in various flow conditions. A number of numerical or empirical models were obtained either by analytical derivations or experimental regressions. Some of these models have become the theory cornerstones of this area and some of them will be applied in the following chapters to support the CFD validations as well. These models are therefore reviewed in this chapter.

CFD method will be validated by numerically reproducing experimental tests. The experimental data collecting and processing strategies will be followed in the CFD simulations as well. Despite the vast difference in the studied parameters and test rig setups across different experiments, there are only three pressure collecting and processing strategies that have been applied in these experiments chosen for CFD validations. These three experimental strategies are reviewed in this chapter as well.

2.1 Acoustic Impedance and Rayleigh Conductivity

Rayleigh (1940) first put forward the concept of acoustic conductivity by making an electro-acoustic analogy. Acoustic conductivity of a perforation is related to the ratio of instantaneous volume flow rate $\hat{q}$ to the driving transient pressure difference $\Delta\hat{p}$:

$$K_R = i\omega\rho\frac{\hat{q}}{\Delta\hat{p}} \tag{2}$$

For a single orifice perforation in an infinite plate of negligible thickness, Rayleigh conductivity in the zero mean flow condition is equal to the ratio of the orifice cross section area to the orifice effective thickness.

$$K_{R0} = \frac{A}{l_{eff}} \tag{3}$$

By similar electro-acoustic analogy, acoustic impedance is compared to electrical impedance and is defined to be the ratio of driving pressure difference to the consequential volume flow rate through the orifice (Pierce, 1981):

$$Z_q = \frac{\Delta\hat{p}}{\hat{q}} = \frac{\Delta\hat{p}}{\hat{v}A} \tag{4}$$

Normalized acoustic impedance is acquired by normalizing the acoustic impedance by the characteristic impedance of the medium:

$$z_n = \frac{Z}{\rho c} = \frac{\Delta\hat{p}}{\hat{v}A\rho c} \tag{5}$$

Relationship between Rayleigh conductivity and normalized acoustic impedance can be found by combing Equation (3) and Equation (5):

$$z_n = \frac{ikA}{K_R} \tag{6}$$

Definition of the specific acoustic impedance and the normalized specific acoustic impedance are given by:

$$Z = \frac{\Delta\hat{p}}{\hat{v}} \tag{7}$$

$$z = r + ix = \frac{\Delta\hat{p}}{\hat{v}\rho c} \tag{8}$$

where r and x are normalized specific resistance and normalized specific resistance reactance respectively.

Howe (1979) proposed his Rayleigh conductivity model for an orifice in an infinite plate of negligible thickness by relating Rayleigh conductivity to the bias flow Strouhal number. Jing and Sun (1999) later refined Howe's model by accommodating the impact of liner thickness into the conductivity model. Luong et al.(2005) analytically derived a simpler expression of Rayleigh conductivity based on a Bernoulli-type equation (Cummings, 1984; 1986). Mendez et al.(Mendez & Eldredge, 2009; Jourdain & Eriksson, 2014) managed to integrate Bernoulli-type analytical models into their CFD codes, however, discharge coefficient remains to be manually defined. Most of these Rayleigh conductivity models are analytically derived and are thus theoretically superior to purely empirical models. However, Rayleigh conductivity models are not direct algebraic parametrical descriptions of the acoustic conductivity, but have to be resolved numerically.

In comparison, most of acoustic impedance models provide parametric descriptions of acoustic impedance for the perforated liners and complex numerical solution of these models is not required. Crandall (1954) pioneered the modern study of acoustic impedance of a tube in a plate. He analytically derived a formula relating specific acoustic impedance of the orifice to its geometric parameters such as orifice thickness and a viscous term. Based on Crandall's work, other authors such as Maa (1996; 1998), Atalla and Sgard (2007) came up with their own models for micro-perforated panel absorbers. Impact of mean flows such as bias flow and grazing flow is accommodated in a few other models such as that of Bauer's and Bellucci's (Bauer, 1977; Heidelberg et al., 1980; Betts, 2000; Bellucci et al., 2004). Acquisition of these acoustic impedance models often started with theoretical analysis and ended up with important factors decided by empirical regressions (Zinn, 1970; Melling, 1973; Dean, 1975; Rice, 1976).

2.2 Rayleigh Conductivity Models

2.2.1 Howe's Model

Howe (1979; 1998) looked into the Rayleigh conductivity of an circular orifice in an infinitely thin wall in the presence of mean bias flow through the hole. He assumed that bias flow velocity is not too high so that fluid can be treated as incompressible and not too low so that viscous effect could be neglected at other regions than the rim of aperture. A vortex sheet forms in the orifice due to the bias flow injection and it carries on travelling downstream of the orifice with the same speed of bias flow. Vortex sheds periodically at the downstream due to upstream and downstream pressure fluctuation and the periodic vortex shedding is responsible for the attenuation of acoustic energy. Derivation based on these assumptions brings Rayleigh conductivity to:

$$K_R = 2r(\gamma - i\delta) \tag{9}$$

$$\gamma - i\delta = 1 + \frac{\frac{\pi}{2}J_1(\mathrm{St})e^{-St} + iK_1(\mathrm{St})\sinh(\mathrm{St})}{St\left[\frac{\pi}{2}J_1(\mathrm{St})e^{-St} - iK_1(\mathrm{St})\cosh(\mathrm{St})\right]} \tag{10}$$

where J_1 and K_1 are the modified Bessel functions of the 1st order of the first kind and second kind respectively. St is Strouhal number based on orifice size and mean bias flow velocity, $\mathrm{St} = \omega r_0 / U_b$. γ is the inertia of the air in the orifice and δ stands for the flow resistance responsible for acoustic absorption. Both terms are dependent on the orifice Strouhal number. Howe's model has been applied and proved to be in good agreement with experimental results by several different authors (Hughes & Dowling, 1990; Eldredge & Dowling, 2003; Mendez & Eldredge, 2009). Howe's model has become a foundation model for a few later Rayleigh conductivity modelling efforts.

2.2.2 Jing and Sun's Model

The thickness the orifice and the plate is assumed to be infinitesimal in Howe's model, however, thickness of a real perforated plate is not negligible. According to Jing and Sun (1999), effective length of an orifice in a plate should be the sum of the end correction length of the orifice and the plate thickness $l_{\mathrm{eff}} = l_{\mathrm{e}} + l_{\mathrm{thic}}$ and they improved Howe's Model by including the effect of plate thickness.

$$K_{RJ} = \frac{A}{l_{\mathrm{eff}}} = \frac{A}{l_{\mathrm{e}} + l_{\mathrm{thic}}} \tag{11}$$

$$\frac{1}{K_{RJ}} = \frac{l_{\mathrm{e}} + l_{\mathrm{thic}}}{A} = \frac{1}{K_R} + \frac{l_{\mathrm{thic}}}{\pi {r_0}^2} = \frac{1}{2r(\gamma - i\delta)} + \frac{2l_{\mathrm{thic}}}{2\pi r r_0} \tag{12}$$

Therefore, modified Rayleigh conductivity is transformed to:

$$K_{RJ} = 2r\left(\frac{1}{\gamma - i\delta} + \frac{2l_{\mathrm{thic}}}{\pi r_0}\right)^{-1} \tag{13}$$

where K_{RJ} represents the Jing-modified Rayleigh conductivity. Jing's model is an improvement on the basis of Howe's model. This model has been validated by other researchers to be in very close agreement with experimental results (Jing & Sun, 1999; Scarpato et al., 2012; Scarpato et al., 2013; Lahiri, 2014).

2.2.3 Luong and Cummings

Luong et al. (2005) started his Rayleigh conductivity modelling effort from Howe's model of Equation (9). However, rather than relating Rayleigh conductivity to flow shear number, he looked into a Bernoulli-type equation (Cummings, 1984; 1986):

$$l_{\text{eff}}\frac{dU_{\text{ac}}}{dt}+\frac{1}{2{C_d}^2}(U_{\text{b}}+U_{\text{ac}})|U_{\text{b}}+U_{\text{ac}}|=\frac{\Delta p_0+p\cos(wt)}{\rho} \quad (14)$$

where l_{eff} represents the effective thickness of the orifice, $p\cos(wt)$ represents the acoustic pressure difference across the orifice and U_{ac} and U_{b} are the acoustic particle velocity and mean bias flow velocity in the orifice respectively. Term $1/(2{C_d}^2)(U_{\text{b}}+U_{\text{ac}})|U_b+U_{\text{ac}}|$ is the pressure drop across the orifice. A simplified expression of Rayleigh conductivity is finally arrived at to be:

$$K_R=K_{R0}\frac{\omega l_{\text{eff}}/U_b}{(\omega \text{l}_{\text{eff}})/U_b\ +i/{C_d}^2} \quad (15)$$

where $K_{R0}=\frac{A}{\text{l}_{\text{eff}}}$ and is the zero flow Rayleigh conductivity. This expression holds in both linear and nonlinear regimes provided that acoustic velocity is no larger than bias flow velocity.

2.2.4 Mendez's Application

Inspired by Luong et al. (2005) and by referring to Cummings's Equation (14), Mendez et al. (2008; 2009) successfully derived an acoustic impedance model for perforated liners. Pressure drop caused by particle velocity through an orifice is expressed as:

$$\Delta P=\rho l_{\text{eff}}\frac{dU}{dt}+\frac{\rho U^2}{2{C_d}^2} \quad (16)$$

The "acoustic impedance jump model" for perforated liners is obtained by linearizing Equation (16) by the orifice velocity U:

$$Z_s=\frac{\partial(\Delta P)}{\partial U}=\frac{\rho U}{\sigma C_d}+i\frac{\rho\omega l_{\text{eff}}}{\sigma} \quad (17)$$

This numerical model described in Equation (16) is then integrated into their LES code AVBP. A high degree of agreement is achieved between acoustic impedance results acquired from the model and that from large eddy simulations and experiments (Mendez & Eldredge, 2009).

2.3 Acoustic Impedance Models

2.3.1 Crandall's Work

Crandall (1954) analytically derived the flow impedance of a tube by accrediting the pressure loss across the orifice to inertial and viscous resistive forces. The momentum equation across the orifice is then investigated by considering viscous and thermal effect while ignoring any end radiation effect and mean bias flows. The normalized specific acoustic impedance is arrived at:

$$z = \frac{ikl_{\text{thic}}}{\sigma F(k_s' r_0)} \tag{18}$$

where ikl_{thic} stands for inertia of the air in the tube. $F(k_s' r_0)$ introduces viscous and thermal effect which was later carefully explained by Melling (1973).

$$F_x = 1 - \frac{2J_1(x)}{xJ_0(x)} \tag{19}$$

$k_s' = \sqrt{-i\omega/\nu'}$ represents Stokes wave number,ν′ represents effective kinematic viscosity which accommodates kinematic viscosity and thermal conductivity effect.

The analytical solutions to Equation (19) exist at low or high limits of shear numbers:

$$z \approx \frac{8\nu' l_{\text{thic}}}{c\sigma r_0^2} + i\frac{k}{\sigma}\frac{4l_{\text{thic}}}{3}, \qquad \text{Sh} < 2 \tag{20}$$

$$z \approx \frac{\sqrt{2\omega\nu'}}{c\sigma r_0} l_{\text{thic}} + il\left(\frac{k}{\sigma} + \frac{\sqrt{2\omega\nu'}}{c\sigma r_0}\right), \text{Sh} > 10 \tag{21}$$

where Shear number $\text{Sh} = r_0\sqrt{\omega/\nu'}$. When shear number is small ($\text{Sh} < 2$), flow in the orifice is similar with steady flow in a narrow tube, and the flow resistance is referred to as Poiseuille-type resistance. When shear number is large ($\text{Sh} > 10$), flow impedance of the orifice becomes a frequency dependent Helmholtz-type resistance (Melling, 1973).

2.3.2 Maa's Model

Based on Crandall's work (Crandall, 1954), Maa (1998) proposed his acoustic impedance model for micro-perforated panel absorbers (MPP absorbers) within

medium shear numbers. According to him, the acoustic impedance of a MPP absorber is determined by porosity of the plate, thickness of the plate, orifice size and the cavity geometry. The normalized specific acoustic resistance and reactance of perforated liners is approximately as:

$$r = \frac{8\mu l_{\text{thic}}}{\sigma \rho c r_0^2}\left(\left(1+\frac{\text{Sh}^2}{32}\right)^{0.5} + \frac{\sqrt{2}}{16}\text{Sh}\frac{r_0}{\text{l}_{\text{thic}}}\right) \quad (22)$$

$$x = \frac{k l_{\text{thic}}}{\sigma}\left(1+\left(9+\frac{\text{Sh}^2}{2}\right)^{-0.5} + \frac{1.7 r_0}{l_{\text{thic}}}\right) \quad (23)$$

This model is demonstrated to be able to predict acoustic impedance for MPP absorbers if $1 < \text{Sh} < 10$ and d/l_{thic} is not far away from 1. This model is particularly useful for micro-perorated panel absorbers. However, it is generally not applicable to plates with large perforations because the Shear number for larger perforations will easily go beyond $1 < \text{Sh} < 10$ range at relatively low noise frequencies.

2.3.3 Atalla's Model

Atalla and Sgard (2007) treated perforated screen as an "equivalent fluid" following Johnson-Allard approach (Johnson et al., 1987; Champoux & Allard, 1991). The density of the medium is modified by dynamics tortuosity of the perforate region and an acoustic impedance model for a perforated panel backed with an air cavity under signal normal incidence condition is finally derived to be:

$$z = \left(\frac{4 l_{\text{thic}}}{d} + 8\frac{l_e}{d}\right)\frac{R_s}{\sigma \rho c} + \frac{1}{\sigma}(2 l_{\text{e}} + l_{\text{thic}})ik - i\cot(k l_c) \quad (24)$$

where $R_s = \sqrt{\mu\omega\rho/2}$ stands for the orifice surface resistance. l_{e} represents the end correction length, $l_{\text{e}} = 0.85r(1\text{-}1.14\sqrt{\sigma})$ if $\sigma < 0.16$. Unlike Maa's model (Maa, 1998) which is only applicable to micro-perforated panel absorbers, Atalla's model is applicable to perforations of both small and large diameters.

2.3.4 Bellucci's Model

Assuming shear number is large ($\text{Sh} > 10$), Bellucci et al.(2004) transformed Equation (18) into:

$$z = \frac{ikl_{\text{eff}}}{\sigma}\left[\left(1+\frac{\sqrt{2}}{\text{Sh}}\right) - i\left(\frac{\sqrt{2}}{\text{Sh}}\right)\right] \quad (25)$$

where $l_{\text{eff}} = l_{\text{e}} + l_{\text{thic}}$. End correction length l_{e} takes in account the correction factors due to bias flow, nonlinear effect and orifice interaction effect.

$$l_{\text{e}} = l_{\text{Hel}} f_\sigma f_{\text{bias}} f_{\text{nonlinear}} \quad (26)$$

$$l_{\text{Hel}} = 2 \cdot 0.8216\, r_0 \left[1 + \frac{(0.77\text{He})^2}{1+0.77\text{He}}\right]^{-1} \quad (27)$$

$$f_\sigma = 1 - \sqrt{\sigma/2} \quad (28)$$

$$f_{\text{bias}} = \frac{0.3(6.0/\text{St}^2)+1}{6.0/\text{St}^2+1} \quad (29)$$

$$f_{\text{nonlinear}} = 1 - 0.3/\text{St}_{\text{ac}}^{0.6} \quad (30)$$

l_{Hel} represents the end correction length without flow, $\text{He} = kr_0$ and is the orifice Helmholtz number. f_σ is a correction factor due to acoustic interaction effect between neighbouring orifices. f_{bias} and $f_{\text{nonlinear}}$ are the correction factors due to bias flow and nonlinearity effects. St represents bias flow Strouhal number $\text{St} = \omega r_0/U_b$. Similarly, St_{ac} represents acoustical Strouhal number $\text{St} = \omega r_0/|U_{ac}|$

The effect of bias flow and nonlinear effect on acoustic resistance is taken into account by:

$$r = \frac{\xi}{c\sigma} G\left(\frac{U_b}{|U_{ac}|}\right)|U_{ac}| \quad (31)$$

$G(x)$, ξ are piecewise functions and have different expressions depending on the relative magnitude of mean bas flow velocity $U_{\text{b}}$and acoustical particle velocity U_{ac}. Combining all above terms, Bellucci's model is written as:

$$z = \frac{\xi}{c\sigma} G\left(\frac{U_b}{|U_{ac}|}\right)|U_{ac}| + \frac{ik}{\sigma}(l_{\text{thic}} + l_{\text{e}})\left[\left(1+\frac{\sqrt{2}}{\text{Sh}}\right) - i\left(\frac{\sqrt{2}}{\text{Sh}}\right)\right] \quad (32)$$

2.3.5 Betts's and Bauer's Model

Betts (2000) proposed a 'Perforate Bias Flow Intermediate Frequency (PBFIF) model'. The resistance term is composed of 50% of the Poiseuille-type resistance,

100% of Helmholtz-type resistance and an expanded term to take into account non-linear and inertial effect.

$$z = \frac{4\nu l}{c\sigma C_d r_0^2} + \frac{\sqrt{2\omega\nu}l}{c\sigma C_d r_0} + \frac{1-\sigma^2}{\sigma C_d}\left|\mathrm{M_B^{eff}}\right| + i\left(\frac{kl_{\mathrm{thic}}}{\sigma C_d} + \frac{\sqrt{2\omega\nu}l_{\mathrm{thic}}}{c\sigma C_d r_0} + \frac{16 r_0 \psi}{3\pi}\right) \quad (33)$$

$$\mathrm{M_B^{eff}} = \mathrm{M_B} + \frac{1}{2c\sigma C_d}\left(\sqrt{2}\mathrm{RMS}(|U_{ac}|)\right) \quad (34)$$

where U_{ac} stands for acoustical particle velocity in the orifice ψ is the Fok's function (Fok & Brocklesby, 1941). Similar to Bett's model, Bauer (1977) proposed his empirical acoustic impedance model by simply combing the viscous resistance term $\frac{\sqrt{8\mu\rho\omega}}{\rho c\sigma}\left(1+\frac{l_{\mathrm{thic}}}{d}\right)$ of Ingard (1953), grazing flow resistance term $\frac{0.3\mathrm{M_g}}{\sigma}$ of Dean (1975), bias flow resistance term $1.15\mathrm{M_b}/\sigma$ of Zinn (1970) and a constant end correction length of $0.25d$ of Rice (1976).

$$z = \frac{\sqrt{8\mu\rho\omega}}{\rho c\sigma}\left(1+\frac{l_{\mathrm{thic}}}{d}\right) + \frac{0.3\mathrm{M_g}}{\sigma} + \frac{1.15\mathrm{M_b}}{\sigma} + i\frac{k(l_{\mathrm{thic}}+0.25d)}{\sigma} \quad (35)$$

All aforementioned analytical and empirical acoustic impedance models can be used to obtain acoustic impedance of perforated plate absobers in signal normal incidence scenarios. However, these models are often not easily applicable in more complex situations. Acoustic attenuation effect of perforated plate absorbers does not only depends on the normal incident Rayleigh conductivity, it is also related to the surrounding boundaries such as the signal incidence angle, the size of the perforated plate and the surrounding acoustic reflection boundaries conditions. Therefore, while these models are able to generate acoustic attenuation effect for a perforated plate absorber in signal normal incident scenarios, they cannot be used as a standalone method for the acquisition of acoustic properties of real gas turbine liners in much more complex geometric, acoustic and flow field conditions in real gas turbine engines. The acoustic damping performance of perforated liners therefore requires experimental tests to be carried out under specific conditions of interests. Three common experimental methods for the investigation of perforated liner acoustic properties are described in next section.

2.4 Experimental Methods

2.4.1 Normal Signal Incidence Impedance Tube

The two-microphone method in an impedance tube (Seybert & Ross, 1977; Chung & Blaser, 1980) has been applied in many experiments which will be cited for CFD validations in this work (Jing & Sun, 1999; Sun et al., 2002; Bellucci et al., 2004; Lee & Kwon, 2004). The two-microphone method is also referred to as the transfer function method and it enables simultaneous investigation of acoustic impedance and noise attenuation properties of the test sample within a wide frequency range and is thus superior to the one-microphone standing wave method which is only able to test a single frequency within one test (Oldfield, 2006).

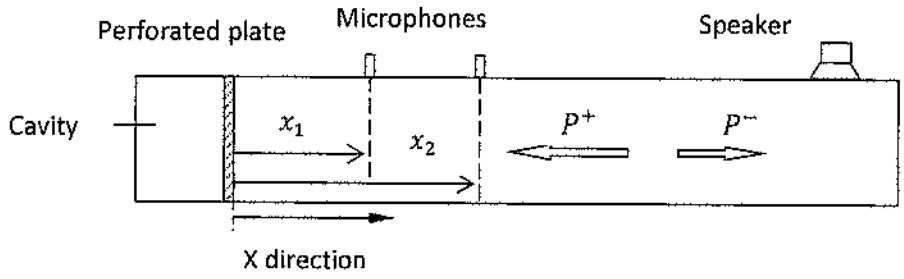

Figure 5 Typical impedance tube setup using two-microphone method

Figure 5 shows a typical impedance tube setup using two-microphone method. Sound signal is excited at one end of the impedance tube. Plane wave forms and travels downstream of the impedance tube until it perpendicularly incidents on the test sample where part of the plane wave will be reflected back to the impedance tube and the rest will be absorbed by the absorber. Two microphones are installed in front of the test sample with distances of x_1 and x_2 respectively. Pressures at the microphones are the superimposition of two acoustic pressures travelling in the positive x direction and negative x direction and pressure at the microphones at a given instant could be decomposed to be:

$$p_1 = P^+ \exp(-kx_1) + P^- \exp(ikx_1) \quad (36)$$

$$p_2 = P^+ \exp(-ikx_2) + P^- \exp(ikx_2) \quad (37)$$

Solve for P^+ and P^-, the amplitudes of the waves travelling in the positive direction and in the negative direction are obtained:

$$P^+ = \frac{p_1 \exp[-ikx_1] - p_2 \exp[-ikx_2]}{\exp(-2ikx_1) - \exp(-2ikx_2)} \quad (38)$$

$$P^- = \frac{p_1 \exp[ikx_1] - p_2 \exp[ikx_2]}{\exp(2ikx_1) - \exp(2ikx_2)} \quad (39)$$

Acoustic reflection coefficient of the panel absorber is then defined:

$$R = \frac{P^-}{P^+} \quad (40)$$

At the test sample surface ($x = 0$), acoustic pressure and acoustic velocity as a result of signal reflection are respectively (Kuttruff, 2007):

$$p = P^+ + P^- \quad (41)$$

$$v = \frac{P^+}{Z_c} - \frac{P^-}{Z_c} \quad (42)$$

Therefore, the complex normalized specific acoustic impedance of the panel absorber is:

$$z = r + ix = \frac{p}{vZ_c} = \frac{P^+ + P^-}{P^+ - P^-} = \frac{1+R}{1-R} \quad (43)$$

According to electro-acoustic analogy, the perforated liner absorber is comparable to an electric circuit as shown in Figure 6(a), the acoustic particle velocity driven by the transient acoustic pressure overcomes the flow resistance r of the orifice, undertakes the inertia of the air mass m in the orifice and interacts with an acoustic compliance of the air in the cavity. The normalized specific acoustic impedance of absorber is therefore expressed as (Kinsler et al., 1999)

$$z = r + ix = r + i\left(\omega m - \frac{1}{\omega c}\right) \quad (44)$$

The perforated liner absorber is also comparable to an oscillating mass on a spring as shown in Figure 6(b). The flow resistance of the orifice is compared to a resistance the spring has to overcome during oscillations.

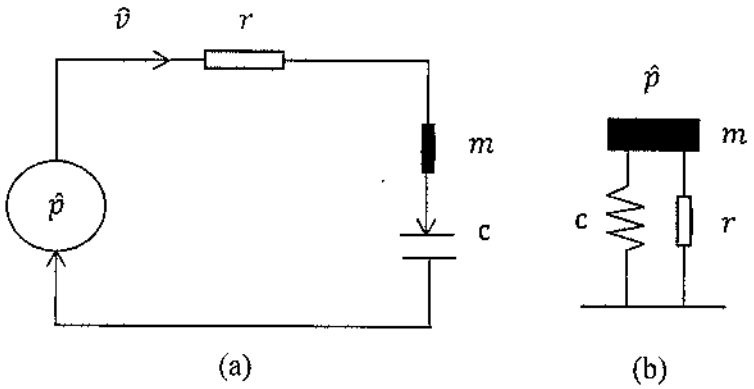

Figure 6 Analogy of a perforated liner absorber: (a) equivalent electrical circuit (b) equivalent mechanical system of an oscillating mass on a resistive spring

The acoustical energy that is not reflected by the absorber is consumed by the acoustical resistance:

$$\alpha = 1 - |R|^2 = \frac{4r}{(1+r)^2 + x^2} \qquad (45)$$

The resonance frequency of a multi-perforated panel absorber corresponds to the frequency at which the acoustic reactance is zero. The calculated absorption coefficient calculated by Equation (45) reaches maximum at the resonance frequency as well. Detailed derivations for the resonance frequency of perforated plate absorbers can be found in (Kuttruff, 2007):

$$f_{\text{reson}} = \frac{c}{2\pi}\sqrt{\frac{A}{V l_{\text{eff}}}} \qquad (46)$$

where c is the speed of sound which is a function of temperature, $c \propto \sqrt{T}$, A is the total opening area on the perforated panel, l_{eff} is the effective length of perforations and V is the volume of air cavity.

In addition to resonance frequency, absorption coefficient curves are often described by its absorption bandwidth as well. Absorption bandwidth is quantified by "Q factor" which is defined to be the ratio of resonance frequency to the

bandwidth across frequencies which display 50% of the optimum acoustic energy absorption effect:

$$Q = f_{\text{reson}} / \Delta f_{1/2} \qquad (47)$$

Absorption coefficient curves with larger Q factors are "narrower" than absorption coefficient curves with smaller Q factors.

Acoustic signal frequencies tested by the two-microphone method are restricted by the microphone separation distance. The signal frequencies should be high enough so that the phase difference between the two microphones is distinguishable; and the frequencies should be small enough so that the phase difference between the two microphones does not exceed 180°. Therefore, the upper and lower frequency limits of an acoustical signal which is tested by the two-microphone method are:

$$\frac{0.05c}{x_2 - x_1} < f < \frac{0.45c}{x_2 - x_1} \qquad (48)$$

The diameter of impedance tube imposes limit on the test signal frequencies as well. The first cut-off frequency of a circular impedance tube is $f = c/2D_{\text{T}}$ and only those acoustic signals with lower frequencies than the cut-off frequency is able to travel in the impedance tube as a plane wave. In addition, microphones should be placed far away from the test samples so that they will not be affected by acoustic field distortions near the test sample $x_1 > 2D_{\text{T}}$.

Two-microphone method calls for prior microphone calibration to match the phase and magnitude response of the two microphones. Highly precise calibration of microphones is sometimes very difficult to achieve (Krüger & Quickert, 1997). Another simplified one-microphone transfer function method has been proposed by Chu (1986) where only a single microphone is required to collect pressures sequentially at two different locations. Microphone calibration is circumvented by using this method, however, similar data processing approach as described for the two-microphone method is then followed in the one-microphone method. This method is applied in those experiments by Jing and Melling et al. (Melling, 1973; Jing & Sun, 2002).

2.4.2 Grazing Signal Incidence in Open Flow Ducts

Perforated liner absorbers are installed parallel with the grazing flow duct in experiments such as that by Eldredge and Dowling (2003) and that by (Houston et al., 2015b). The downstream flow duct is present in these experiments as shown in Figure 7. The incident acoustic energy is either reflected by the absorber or absorbed by the absorber or transmitted into the downstream flow duct. Acoustic energy absorption coefficient of the liner absorber is obtainable by applying two-microphone method in the upstream duct and downstream duct respectively. However, normal incidence acoustic impedance is not obtainable by the two-microphone method in this signal grazing incidence scenario.

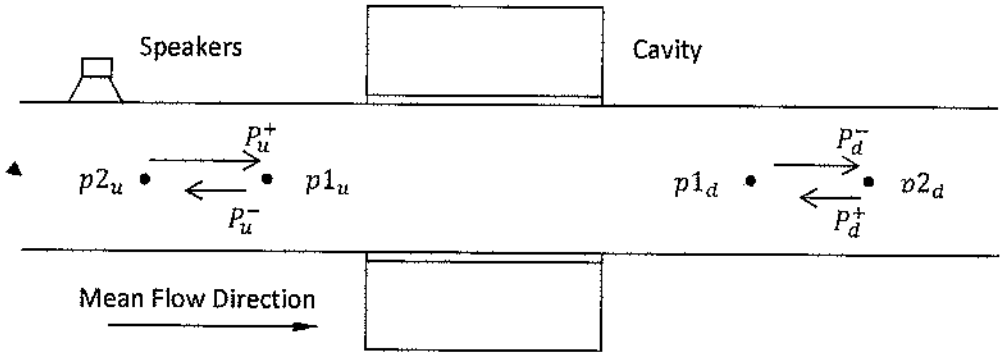

Figure 7 Typical setup of a side branched liner absorber on open flow ducts

Suppose sound signal travels in the same direction with the mean grazing flow, Pressure signal $\mathrm{p1_u}$ and $\mathrm{p2_u}$ recorded by the two upstream microphones are decomposed into two waves travelling in opposite directions:

$$p1_u = P_u^+ \exp\left(-ik\left(1+\mathrm{M_g}\right)x_{1\mathrm{u}}\right) + P_u^- \exp\left(ik\left(1-\mathrm{M_g}\right)x_{1\mathrm{u}}\right) \quad (49)$$

$$p2_u = P_u^+ \exp\left(-ik\left(1+\mathrm{M_g}\right)x_{2\mathrm{u}}\right) + P_u^- \exp\left(ik\left(1-\mathrm{M_g}\right)x_{2\mathrm{u}}\right) \quad (50)$$

Solve for P_u^+ and P_u^-:

$$P_u^+ = \frac{p1_u \exp\left[-ik\left(1-\mathrm{M_g}\right)\mathrm{x_{1u}}\right] - p2_u \exp\left[-ik\left(1-\mathrm{M_g}\right)\mathrm{x_{2u}}\right]}{\exp(-2ikx_{1\mathrm{u}}) - \exp(-2ikx_{2\mathrm{u}})} \quad (51)$$

$$P_u^- = \frac{p1_u \exp\left[ik\left(1+\mathrm{M_g}\right)x_{1\mathrm{u}}\right] - \mathrm{p2_u} \exp\left[ik\left(1+\mathrm{M_g}\right)x_{2\mathrm{u}}\right]}{\exp(2ikx_{1u}) - \exp(2ikx_{2u})} \quad (52)$$

Same decomposition operation is applied to the two downstream microphones:

$$p1_d = P_d^+ \exp\left(ik(1-\mathrm{M_g})x_{1\mathrm{d}}\right) + P_d^- \exp\left(-ik(1+\mathrm{M_g})x_{1\mathrm{d}}\right) \quad (53)$$

$$p2_d = P_d^+ \exp\left(ik(1-\mathrm{M_g})x_{2\mathrm{u}}\right) + P_d^- \exp\left(-ik(1+\mathrm{M_g})x_{2\mathrm{d}}\right) \quad (54)$$

Solve for P_d^+ and P_d^-, we arrive at:

$$P_d^+ = \frac{p1_d \exp\left[ik(1+\mathrm{M_g})x_{1\mathrm{d}}\right] - p2_d \exp\left[ik(1+\mathrm{M_g})x_{2\mathrm{d}}\right]}{\exp(2ikx_{1\mathrm{d}}) - \exp(2ikx_{2\mathrm{d}})} \quad (55)$$

$$P_d^- = \frac{p1_d \exp\left[-ik(1-\mathrm{M_g})x_{1\mathrm{d}}\right] - p2_d \exp\left[-ik(1-\mathrm{M_g})x_{2\mathrm{d}}\right]}{\exp(-2ikx_{1d}) - \exp(-2ikx_{2d})} \quad (56)$$

Transmission coefficient and reflection coefficient of the perforated liner absorber are defined as:

$$T = \frac{P_d^-}{P_u^+}, \quad R = \frac{P_u^-}{P_u^+} \quad (57)$$

Acoustic energy carried by the propagating waves in the presence of grazing flow is calculated by (Blokhintsev, 1956):

$$E = (1 \pm \mathrm{M_g})^2 |P^{\pm}|^2 \quad (58)$$

According to principle of energy conservation, the amount of acoustic energy entering the liner section is equal to the addition of the acoustic energy absorbed by the liner absorber and that transmitting the liner section. Therefore, acoustic energy dissipation coefficient in cases where signal and grazing flow travels in the same direction is expressed as:

$$\alpha_+ = \frac{E_u^+ + E_d^- - E_u^- - E_d^+}{E_u^+ + E_d^-} = 1 - \frac{E_u^- + E_d^+}{E_u^+ + E_d^-} \quad (59)$$

In those cases of non-reflecting downstream exits, Equation (59) is reduced to:

$$\alpha_+ = 1 - \frac{E_u^- + E_d^+}{E_u^+} = 1 - \left(\frac{1-\mathrm{M_g}}{1+\mathrm{M_g}}\right)^2 |R|^2 - |T|^2 \quad (60)$$

where R is reflection coefficient, T is the transmission coefficient.

According to Equation (58), absorption coefficient of the liner absorber will be different from the one calculated by Equation (59) if sound signal propagation direction is opposite to the mean flow direction. And the average absorption

coefficient of the liner absorber will be $\alpha = (\alpha_+ + \alpha_-)/2$. However, the terms α_+ alone is referred to as "absorption coefficient" by Eldredge and Dowling (2003).

2.4.3 In-situ Impedance Method

Two-microphone transfer function method is a reliable method because it is safe from acoustic distortions near the test samples. This method is widely applied in impedance tubes to acquire the normal incidence acoustic impedance of the test samples. Acoustic energy absorption coefficient of a perforated liner absorber is also obtainable by this transfer function method in grazing signal incidence cases as described in the previous section. However, normal incidence acoustic impedance is not obtainable by this method in grazing signal incidence situations because of the difficulty in setting up normal incidence impedance tubes.

Dean (1974) proposed an in-situ measurement method in order to test the normal incidence acoustic impedance in grazing signal incidence situations. In this method, two microphones are placed flush with the flow duct wall near the cavity and flush with cavity bottom wall respectively as shown in Figure 8. The cross dimension of the cavity has to be much smaller than the wavelength of the tested signal so that pressure phase difference across the cross dimension is minor. Multiple in-situ measurements should be carried out in situations where the cross dimension of liner is not significantly smaller than the wavelength of the test signal.

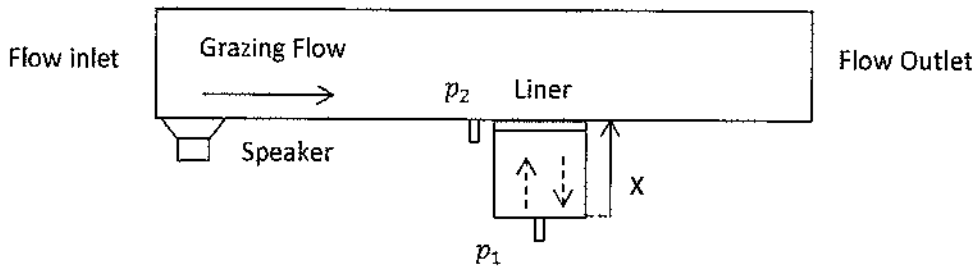

Figure 8 Typical test rig setup and microphone positions for normal incidence acoustic impedance measurement by the in-situ impedance method

The pressure inside the cavity is a superimposition of the incident wave on the cavity bottom wall p^+ and the reflected wave p^- .

$$p^+ = Pe^{i(\omega t - kx)} \; ; \; p^- = Pe^{i(\omega t + kx)} \tag{61}$$

The two waves travelling in the opposite direction result in a standing wave in the cavity:

$$p = 2Pe^{i\omega t}\cos(kx) \tag{62}$$

$$p_1 = 2Pe^{i\omega t} \tag{63}$$

And the resulting acoustic velocity is:

$$u = i\frac{2P}{\rho c}e^{i\omega t}\sin(kx) \tag{64}$$

The normalized specific acoustic impedance at the surface of the liner ($x = l_c$) is:

$$Z_{x=l_c} = \frac{p_2}{u_{x=l_c}} = -i\frac{p_2}{p_1}/\sin(kl_c) \tag{65}$$

And the normalized specific acoustic impedance of the liner backed absorber is:

$$z = -i\frac{1}{\sigma}\left[\frac{p_2}{p_1} - \cos(kl_c)\right]/\sin(kl_c) \tag{66}$$

where l_c is the depth of the cavity and σ is the porosity which is defined by the ratio of total opening area to the overall liner surface area.

The in-situ impedance measurement method is adopted by a number of experiments studying grazing flow effects (Kirby & Cummings, 1998; Jing et al., 2001; Malmary et al., 2001; Lee & Ih, 2003; Elnady et al., 2004). Other more complex in-situ impedance methods exist as well. Watson and Jones (2013) summarized four much more complex in-situ impedance methods: Linearized Euler Equations, Convected Helmholtz Equations, Single Mode Method and Straight-forward Method. These methods requires complicated numerical data processing process (Watson et al., 1999; Jones et al., 2003) and is not elaborated in this work.

Experimental methods are able to provide acoustic damping properties of certain perforated liner absorbers on a case by case basis. This is an obvious advantage over empirical models which cannot reflect the impact of external influencing factors such as acoustic boundary conditions and surrounding geometries. However, on the other hand, the case by case experimental tests often cause very high time

and economical cost due to the large number of variables. CFD method retains the advantages of experimental method in terms of reflecting impacts of external acoustic boundary conditions and surrounding geometries. However, a complete and practical CFD method to model acoustic damping effect of perforated liners is yet neither established nor validated.

3. CFD Methodologies

Computational fluid dynamics (CFD) is able to obtain a numerical solution to a fluid dynamics problem by solving its flow governing equations in the spatial and temporal domain under pre-defined boundary conditions. A complete CFD simulation setup requires four components to be appropriately defined (Anderson & Wendt, 1995). First, the fluid dynamics problem has to be resolved on sufficiently small finite volumes and time steps so that flow structures of all interested scales and transience are numerically well represented. Second, the spatial and temporal discretization methods are to be decided for the calculation of time marching acoustic problems, should it be with first order accuracy or second order accuracy, numerically explicit or implicit, upwind difference discretization or central difference discretization. Third, flow and acoustic boundary conditions to a large degree determines or significantly affects flow and acoustic fields in the calculation domain and should be carefully imposed. Fourth, appropriate flow governing equations are to be chosen, should it be incompressible or compressible flow, laminar flow or turbulent flow, turbulence structures resolved by the RANS method or LES method. In addition, the porous media model was originally designed to represent those isotropic and highly porous materials such as polyester foams. The methodology about how to apply porous media model to stand for those scarcely and one-directionally perforated liners is to be established in this chapter.

3.1 Governing Equations

The flow governing Navier-Stokes equations are a set of equations which describe how local density, velocities and energy change due to the influence of local temporal variation effect, convective effect, diffusive effect and other source effects. The partial differential form of Navier-Stokes equations for a three-dimensional compressible flow include (Versteeg & Malalasekera, 2007):

Mass conservation equation:

$$\frac{\partial \rho}{\partial t} + \mathrm{div}(\rho \vec{u}) = 0 \qquad (67)$$

Momentum equations:

$$\frac{\partial(\rho u)}{\partial t} + \text{div}(\rho u \vec{\text{u}}) = -\frac{\partial p}{\partial x} + \frac{\partial \tau_{xx}}{\partial x} + \frac{\partial \tau_{yx}}{\partial y} + \frac{\partial \tau_{zx}}{\partial z} + S_{Mx} \quad (68)$$

$$\frac{\partial(\rho v)}{\partial t} + \text{div}(\rho v \vec{\text{u}}) = -\frac{\partial p}{\partial y} + \frac{\partial \tau_{xy}}{\partial x} + \frac{\partial \tau_{yy}}{\partial y} + \frac{\partial \tau_{zy}}{\partial z} + S_{My} \quad (69)$$

$$\frac{\partial(\rho w)}{\partial t} + \text{div}(\rho w \vec{\text{u}}) = -\frac{\partial p}{\partial z} + \frac{\partial \tau_{xz}}{\partial x} + \frac{\partial \tau_{yz}}{\partial y} + \frac{\partial \tau_{zz}}{\partial z} + S_{Mz} \quad (70)$$

where u, v, w are the components of the velocity vector $\vec{\text{u}}$ in x, y, z directions. τ_{ij} represents a viscous stress in the j direction exerted on a surface perpendicular in i direction, S_M is the momentum source term to include other sources or sinks of the momentum such as body forces.

Energy (enthalpy) equation:

$$\frac{\partial(\rho h)}{\partial t} + \text{div}(\rho h \vec{\text{u}}) = \text{div}(k \text{ grad } T) + \frac{\partial p}{\partial t} + \left[\frac{\partial(u\tau_{xx})}{\partial x} + \frac{\partial(u\tau_{yx})}{\partial y} + \frac{\partial(u\tau_{zx})}{\partial z} + \frac{\partial(v\tau_{xy})}{\partial x} + \frac{\partial(v\tau_{yy})}{\partial y} + \frac{\partial(v\tau_{zy})}{\partial z} + \frac{\partial(w\tau_{xz})}{\partial x} + \frac{\partial(w\tau_{yz})}{\partial y} + \frac{\partial(w\tau_{zz})}{\partial z}\right] + S_h \quad (71)$$

where h represents the specific total enthalpy and S_h is the enthalpy source term.

For Newtonian fluid, the viscous shear stress is proportional to the deformation rate of fluid speed:

$$\tau_{xx} = 2\mu\frac{\partial u}{\partial x} + \lambda \text{ div } u;\ \tau_{yy} = 2\mu\frac{\partial v}{\partial y} + \lambda \text{ div } u;\ \tau_{zz} = 2\mu\frac{\partial w}{\partial z} + \lambda \text{ div } u \quad (72)$$

$$\tau_{xy} = \tau_{yx} = \mu(\frac{\partial u}{\partial y} + \frac{\partial v}{\partial x});\ \tau_{xz} = \tau_{zx} = \mu(\frac{\partial u}{\partial z} + \frac{\partial w}{\partial x});\ \tau_{yz} = \tau_{zy} = \mu(\frac{\partial v}{\partial z} + \frac{\partial w}{\partial y}) \quad (73)$$

where μ is dynamic viscosity of the fluid and λ is the second viscosity.

Combining continuity, momentum and energy equations, a general form of flow governing equation is attainable by introducing a general scalar ϕ:

$$\frac{\partial(\rho\phi)}{\partial t} + \text{div}(\rho\phi\vec{\text{u}}) = \text{div}(\Gamma \text{ grad } \phi) + S_\phi \quad (74)$$

Equation (74) is reduced to mass conservation, momentum and energy equations by designating ϕ to be *1, u, v, w* and h_0 and choosing appropriate expressions for the general diffusion coefficient Γ and the source term S_ϕ.

Last, thermodynamic relationships between pressure p, enthalpy h, temperature T and density ρ are employed to mathematically close the set of equations.

$$p = p(\rho, T); h = h(\rho, T) \qquad (75)$$

Up to now, seven unknowns u, v, w, h_0, p, T, ρ appear in seven independent equations. Therefore, the set of equations are mathematically closed and solutions to the seven parameters are theoretically attainable.

3.2 Simulation of Turbulent Flows

The Navier-Stokes equations are mathematically closed and precise solutions to these equations are thus theoretically obtainable, however, a general solution of these non-linear second order partial differential equations is still beyond capability of contemporary mathematics. Therefore, these partial differential equations have to be resolved by finite difference discretization methods. Features of all spatial and temporal scales can be directly resolved if the discretized equations are solved on sufficiently small grids and time steps. For example, laminar flow is often comprised of highly uniform and steady flow structures. Therefore, a direct simulation solution to a laminar flow is obtainable based on moderate grids and time steps.

However, many more flow conditions in industry world fall into turbulent flow regime. Direct numerical simulation (DNS) of turbulent flows has to be carried out on very fine meshes and small time steps due to the necessity to resolve micro-scale instantaneous turbulent eddies. As a consequence, the computational overhead is excessive and DNS is not feasible for engineering applications. Two common turbulence modeling strategies exist to avoid direct calculation of the instantaneous small scale turbulent eddies: time-averaging Reynolds averaged Navier-Stokes method (RANS) and spatial-averaging large eddy simulations (LES).

3.2.1 Time-averaging RANS Method

Reynolds averaged Navier-Stokes method (RANS) decomposes transient velocities and pressures as the addition of time-averaged mean part $\bar{\phi}$ and time-dependent turbulent part ϕ'.

$$u = \tilde{u} + u';\ v = \tilde{v} + v';\ w = \tilde{w} + w';\ p = \bar{p} + p' \qquad (76)$$

Substituting Equation (76) in to Equation (67)-(73) and apply some mathematical simplifications, The Reynolds averaged governing equations of a three dimensional compressible flows then become:

$$\frac{\partial \tilde{\rho}}{\partial t} + \operatorname{div}\left(\tilde{\rho}\tilde{\mathbf{u}}\right) = 0 \qquad (77)$$

$$\frac{\partial(\tilde{\rho}\tilde{u})}{\partial t} + \operatorname{div}\left(\tilde{\rho}\tilde{u}\tilde{\mathbf{u}}\right) = -\frac{\partial \bar{P}}{\partial x} + \operatorname{div}(\mu \operatorname{grad} \tilde{u}) + \left[-\frac{\partial\left(\overline{\rho u'^2}\right)}{\partial x} - \frac{\partial(\overline{\rho u'v'})}{\partial y} - \frac{\partial(\overline{\rho u'w'})}{\partial z}\right] + S_{Mx} \qquad (78)$$

$$\frac{\partial(\tilde{\rho}\tilde{v})}{\partial t} + \operatorname{div}\left(\tilde{\rho}\tilde{v}\tilde{\mathbf{u}}\right) = -\frac{\partial \bar{P}}{\partial y} + \operatorname{div}(\mu \operatorname{grad} \tilde{v}) + \left[-\frac{\partial(\overline{\rho u'v'})}{\partial x} - \frac{\partial\left(\overline{\rho v'^2}\right)}{\partial y} - \frac{\partial(\overline{\rho v'w'})}{\partial z}\right] + S_{My} \qquad (79)$$

$$\frac{\partial(\tilde{\rho}\tilde{w})}{\partial t} + \operatorname{div}\left(\tilde{\rho}\tilde{w}\tilde{\mathbf{u}}\right) = -\frac{\partial \bar{P}}{\partial z} + \operatorname{div}(\mu \operatorname{grad} \tilde{w}) + \left[-\frac{\partial(\overline{\rho u'w'})}{\partial x} - \frac{\partial(\overline{\rho v'w'})}{\partial y} - \frac{\partial\left(\overline{\rho w'^2}\right)}{\partial z}\right] + S_{Mz} \qquad (80)$$

And the general scalar governing equation is written as:

$$\frac{\partial\left(\tilde{\rho}\tilde{\Phi}\right)}{\partial t} + \operatorname{div}\left(\tilde{\rho}\tilde{\Phi}\tilde{\mathbf{u}}\right) = \operatorname{div}\left(\Gamma_{\Phi} \operatorname{grad} \tilde{\Phi}\right) + \left[-\frac{\partial(\overline{\rho u'\varphi'})}{\partial x} - \frac{\partial(\overline{\rho v'\varphi'})}{\partial y} - \frac{\partial(\overline{\rho w'\varphi'})}{\partial z}\right] + S_{\Phi} \qquad (81)$$

The averaging operation introduces six extra Reynolds stress terms:

$$\tau_{xx} = -\overline{\bar{\rho}u'^2}, \qquad \tau_{yy} = -\overline{\bar{\rho}v'^2}, \qquad \tau_{zz} = -\overline{\bar{\rho}w'^2}, \tag{82}$$

$$\tau_{xy} = \tau_{yx} = \overline{-\bar{\rho}u'v'}, \qquad \tau_{xz} = \tau_{zx} = -\overline{\bar{\rho}u'w'}, \qquad \tau_{yz} = \tau_{zy} = -\overline{\bar{\rho}v'w'} \tag{83}$$

Many turbulence models to mathematically close the Reynolds averaged Navier-Stokes equations have been proposed, such as mixing length model, one equation Spalart–Allmaras model, two-equation $\kappa - \varepsilon$ models, $\kappa - \omega$ models and Reynolds Stress models (Launder & Spalding, 1972; Gibson & Launder, 1978; Spalart & Allmaras, 1992; Wilcox, 1998). Two-equation $\kappa - \varepsilon$ model was developed by applying Boussinesq's hypothesis of isotropic turbulence viscosity and that Reynolds stress is proportional to the deformation rate of the flow velocity in all directions (Pope, 1975; Schmitt, 2007):

$$\tau_{ij} = -\overline{\bar{\rho}u_i'u_j'} = \mu_{\text{eff}}\left(\frac{\partial u_i}{\partial x_j} + \frac{\partial u_j}{\partial x_i}\right) - \frac{2}{3}\rho\kappa\delta_{ij} \tag{84}$$

where μ_{eff} is the dynamic effective eddy viscosity and κ is the turbulence kinetic energy. The dynamic effective eddy viscosity in $\kappa - \varepsilon$ model is computed by:

$$\mu_{\text{eff}} = \rho C_\mu \frac{\kappa^2}{\varepsilon} \tag{85}$$

Where $C_\mu = 0.09$ and ε is the turbulence kinetic energy dissipation rate. The six unknown Reynolds stresses are successfully accounted for by two unknowns κ and ε. Turbulence kinetic energy and its dissipation rate are resolved in two extra transport equations:

$$\frac{\partial(\bar{\rho}k)}{\partial t} + \operatorname{div}\left(\bar{\rho}k\tilde{\vec{u}}\right) = \operatorname{div}\left(\frac{\mu_{\text{eff}}}{\sigma_k}\operatorname{grad} k\right) + 2\mu S_{ij}S_{ij} - \rho\varepsilon \tag{86}$$

$$\frac{\partial(\bar{\rho}\varepsilon)}{\partial t} + \operatorname{div}\left(\bar{\rho}\varepsilon\tilde{\vec{u}}\right) = \operatorname{div}\left(\frac{\mu_{\text{eff}}}{\sigma_\varepsilon}\operatorname{grad}\varepsilon\right) + C_{1\varepsilon}\frac{\varepsilon}{\kappa}2\mu S_{ij}S_{ij} - C_{1\varepsilon}\rho\frac{\varepsilon^2}{\kappa} \tag{87}$$

where $S_{ij} = \frac{1}{2}\left(\frac{\partial \tilde{u}_i}{\partial x_j} + \frac{\partial \tilde{u}_j}{\partial x_i}\right)$ and the term $2\mu S_{ij}S_{ij}$ represents the kinetic energy transferred from mean flow to the turbulent flow. The turbulent kinetic energy is dissipated at the rate of ε in the second equations.

3.2.2 Spatial Filtering LES Method

Large eddies in turbulent flows are anisotropic and their evolution is to a large degree decided by the interactions between the mean flow and flow boundaries. Large eddies are able to directly extract kinetic energy from the mean flow and thus has noticeable impact on the mean flow field. By contrast, small scale eddies tend to be more isotropic and has very little effect on the development of large scale flows (Versteeg & Malalasekera, 2007). Large eddy simulation (LES) is a simulation method by which large eddies are directly resolved in space and time while the small eddies are removed and only the effect of smaller eddies on the mean flow is modelled.

Large eddy simulation starts with a space high-pass filtering operation in order to separate flow scales into the resolved large scales and modeled small scales:

$$\overline{\Phi}(x,t) = \iiint_{-\infty}^{\infty} G(x,x',\Delta)\,\Phi(x',t)dx_1' d\,x_2'\,dx_3' \tag{88}$$

where Δ is the cutoff width, $\Phi(x,t)$ is the original variable and $\overline{\Phi}(x,t)$ is the filtered large scale part of the variable. Cut-off width Δ is an indicative measure of the critical size of eddies, eddies larger than cut-off width are directly resolved while smaller eddies are rejected. In finite volume method, it is often a common practice to define the cut-off width as the local mesh size $\Delta = \Delta_x$ (Versteeg & Malalasekera, 2007). Therefore, meshes of high resolution are required in order to directly resolve eddies of small scales. The spatially filtered three dimensional compressible Navier-Stokes equations are:

$$\frac{\partial \bar{\rho}}{\partial t} + \operatorname{div}\left(\bar{\rho}\vec{\bar{u}}\right) = 0 \tag{89}$$

$$\frac{\partial(\bar{\rho}\,\bar{u})}{\partial t} + \operatorname{div}\left(\bar{\rho}\bar{u}\vec{\bar{u}}\right) = -\frac{\partial \bar{p}}{\partial x} + \mu\,\operatorname{div}\left(\operatorname{grad}(\vec{u})\right) - \left(\operatorname{div}\left(\bar{\rho}\,\overline{u\vec{u}}\right) - \operatorname{div}\left(\bar{\rho}\bar{u}\vec{\bar{u}}\right)\right) + S_{Mx} \tag{90}$$

$$\frac{\partial(\bar{\rho}\bar{v})}{\partial t} + \operatorname{div}(\bar{\rho}\bar{v}\vec{u}) = -\frac{\partial \bar{p}}{\partial y} + \mu \operatorname{div}(\operatorname{grad}(v)) - \left(\operatorname{div}\left((\bar{\rho}\,\overline{v\vec{u}}\right)\right) - \operatorname{div}(\bar{\rho}\bar{v}\vec{u})\right) + S_{My} \quad (91)$$

$$\frac{\partial(\bar{\rho}\bar{w})}{\partial t} + \operatorname{div}(\bar{\rho}\bar{w}\vec{u}) = -\frac{\partial \bar{p}}{\partial z} + \mu \operatorname{div}(\operatorname{grad}(\bar{w})) - \left(\operatorname{div}\left((\bar{\rho}\,\overline{w\vec{u}}\right)\right) - \operatorname{div}(\bar{\rho}\bar{w}\vec{u})\right) + S_{Mz} \quad (92)$$

The general scalar form of Navier-Stokes equations is:

$$\frac{\partial(\bar{\rho}\bar{\Phi})}{\partial t} + \operatorname{div}(\bar{\rho}\bar{\Phi}\vec{u}) = \operatorname{div}(\Gamma_{\Phi}\operatorname{grad}(\bar{\Phi})) - \left(\operatorname{div}(\bar{\rho}\overline{\Phi\vec{u}}) - \operatorname{div}(\bar{\rho}\bar{\Phi}\vec{u})\right) + S_{\bar{\Phi}} \quad (93)$$

The second term in the right hand side

$$\operatorname{div}(\bar{\rho}\overline{\Phi\vec{u}}) - \operatorname{div}(\bar{\rho}\bar{\Phi}\vec{u}) = \frac{\partial \tau_{ij}}{\partial x_j} \quad (94)$$

where the sub-grid-scale stress $\tau_{ij} = (\bar{\rho}\overline{\Phi\vec{u}}) - (\rho\bar{\Phi}\vec{u})$ and the sub-grid stress τ_{ij} is related to the strain rate of large scale eddies $S_{ij} = \frac{1}{2}\left(\frac{\partial \bar{u}_i}{\partial x_j} + \frac{\partial \bar{u}_j}{\partial x_i}\right)$ by the "sub-grid turbulence viscosity" Several modelling methods for the sub-grid turbulence viscosity have been proposed such as Smagorinksy-Lilly SGS model, Wale SGS model or dynamic SGS models (Smagorinsky, 1963; Germano et al., 1991; Lilly, 1992; Nicoud & Ducros, 1999).

3.2.3 RANS / LES Comparison

Turbulence structures of all scales are modelled by one single turbulence model within RANS method. While RANS method may be able to provide satisfactory results of mean flow field, modelling anisotropic large eddies and isotropic small eddies using the same turbulence model is very likely to incur errors for highly transient swirling flow simulations. In addition, temporal averaging strategy of RANS method tends to lose transient unsteadiness at each time step and the loss of transient features will accumulate over time. As a result, self-excited flow unsteadiness is expected to be significantly underestimated by RANS method. This kind of incapability of RANS in simulating the evolution of unsteady turbulence has

been proved by a number of researchers (Jones & Whitelaw, 1982; Rodi, 1997; Boudier et al., 2007; Gicquel et al., 2012).

On the other hand, the influential large eddy features are directly resolved in large eddy simulations by solving the spatially filtered Navier-Stokes equations. Only eddies of smaller scale than the cut-off width is discarded, the development of large scale turbulence features over time are able to be retained if they are resolved in sufficiently small time steps. Although small eddies are still to be modelled by sub-grid stress model, their effect on the development of large scale mean flow field is relatively much weaker. Therefore, large eddy simulation is theoretically superior to RANS method in terms of capturing the unsteadiness of transient turbulent flows (Pierce & Moin, 2004; Selle et al., 2004a; Roux et al., 2005; Schmitt et al., 2007).

Large eddy simulation of the reacting flow and combustion instability phenomenon in gas turbine combustors is getting increasing attention to facilitate industrial engine design. Large eddy simulation of swirling reacting flows has been proved to be able to yield satisfactory results on meshes of affordable size and well-imposed boundary conditions (Erlebacher et al., 1992; Roux et al., 2005; Meier et al., 2007; Veynante, 2009; Moureau et al., 2011). On the other hand, large eddy simulation is originally evolved for incompressible flows and extension of its application to compressible flow may lead to extra discretization and sub-grid numerical errors (Garnier et al., 2009). In addition, the chemical reaction in premixed combustion takes place instantaneously at sub-grid scale, accommodating chemical reaction modelling will lead to dramatic variable gradients across neighbouring meshes and time step and this may affect the accuracy of sub-grid stress modelling as well (Pitsch, 2006).

The critical Reynolds number at which a pipe laminar flow turns turbulent falls in between 2000-4000 (Hanks, 1963). The exact value of the critical Reynolds number relies on a number of external factors such as the roughness of the wall and the flow stabilities (Roshko, 1961; Kerswell, 2005). In this work, laminar flow is applied to simulate those cases where only acoustic signal is present and the situations where mean flow is present but the flow Reynolds number is less than 3500. RANS

method along with standard $\kappa - \varepsilon$ turbulence model is applied to simulate flow cases where mean flow Reynolds number is above 3500. Large eddy simulation method is applied in the last chapter to capture the self-excited pressure instability modes in a lab-scale 'PRECCINSTA' combustor.

3.3 Porous Media Model

A porous material is typically made of intertwining solid frames and void spaces. Void fluid spaces are to be resolved in CFD calculations. However, meshing and resolving of all those very small void spaces are nearly impossible due to the huge amount of geometry details and the consequential computational cost. From another perspective, researchers and industry are often more interested in the macroscopic effect of porous region on the transverse flow rather than those flow field details in each individual void space (Mualem, 1976; Champoux & Allard, 1991; Gerke & Genuchten, 1993).

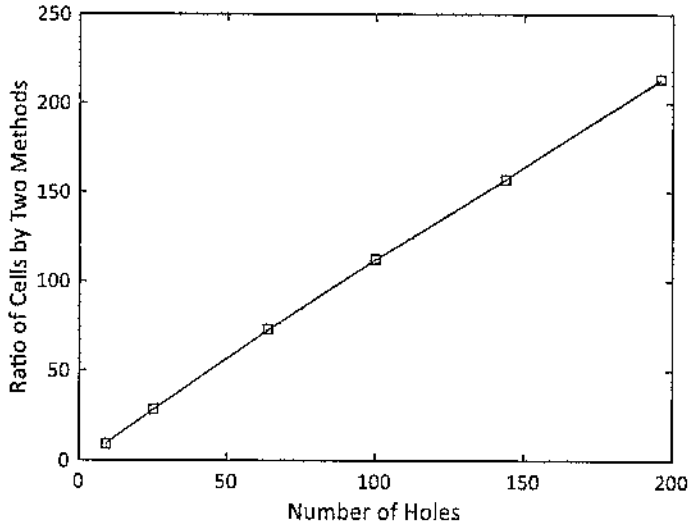

Figure 9 The Ratio of mesh counts required by resolving all perforations and by applying porous zone representation

This work proposes that a perforated liner is able to be treated as a homogenous porous media region. Geometry details are ignored and the flow is assumed to be uniform in the porous media region. This method is able to significantly reduce the computational cost otherwise needed in resolving the large number of effusion cooling holes on a combustor liner. The number of meshes required resolving every

individual hole and that required by treating the perforated plate as a homogenous porous zone is compared in Figure 9. The meshed plate is a 3mm thick 0.1m×0.1m square plate with a number of perpendicular holes (d=2.5mm) as shown in Figure 10(b). When the plate is treated as a homogenous zone, its cross section is built with a 20×20 grid and two layers of meshes are built in the thickness direction which results in a total number of 800 cells in the porous media zone. In cases where real geometry of each hole is resolved, each hole is built with 12 cells across its radial direction and 10 cells in the axial direction at which resolution the internal flow field can be well captured. The mesh counts grow linearly with the number of perforations and as a result, the amount of computational time which is saved by using the porous media model becomes significant where hundreds of small holes are to be resolved. In addition, the mesh counts do not include those small meshes just outside each hole, which, if taken into account, will make the mesh count ratio even more significant.

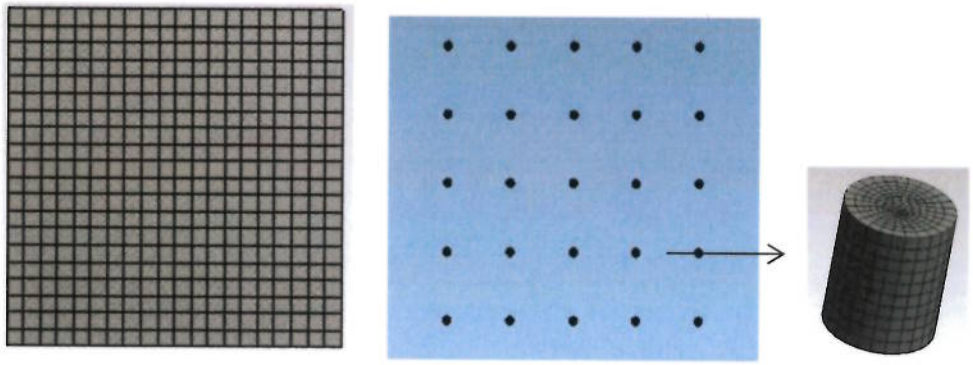

(a) (b) (c)

Figure 10 Two different meshing and calculation strategies for perforated plate region: (a) treating perforated plate as a porous media region; (b) calculation of every individual perforation; (c) a close-up of the meshes in a perforation

Navier-Stokes equations are amended by the porosity and flow resistance so that effects of the porous media on the transverse flow is able to be accounted for. Two porous media models are analyzed: superficial velocity model and physical velocity model. The methodology on how to define the porous media model in order to obtain acoustic properties of perforated liners is provided in this section.

3.3.1 Superficial Velocity Model

The pressure loss a fluid is subjected to when it travels across porous media is accommodated by including an extra momentum sink term S_p in the superficial velocity porous media model(Fluent, 2009).

$$\frac{\partial(\sigma\rho\phi)}{\partial t} + \mathrm{div}(\rho\phi\vec{\mathrm{u}}) = \mathrm{div}(\Gamma \mathrm{grad}\phi) + S_{\phi p} \quad (95)$$

Porosity is not taken into account in the convection and diffusion terms in this porous media Navier-Stokes formulation and therefore same velocity is reported inside and outside the porous media region. The source term in the momentum equation within porous zone is:

$$S_{\phi p} = S_{\phi 0} + S_p \quad (96)$$

where $S_{\phi 0}$ is the original source term and S_p stands for extra source term due to the existence of porous media region:

$$S_p = -(\mathrm{C}_1 U_{\mathrm{sup}} + \mathrm{C}_2 \frac{1}{2} |U_{\mathrm{sup}}| U_{\mathrm{sup}}) \quad (97)$$

where U_{sup} is the superficial velocity which is the flow velocity before flow enters the porous media region. C_1, C_2 are the viscous and inertial resistance coefficient of the porous media based on the superficial velocity.

Superficial velocity model is able to represent the pressure drop a flow is subjected to by defining viscous and inertial resistance. This is often sufficient when the pressure dissipation effect of a porous media is the sole research purpose. However, acoustic impedance as defined by Equation (8) is the ratio of pressure drop to the resulting flow velocity. The superficial velocity model will not able to calculate the acoustic impedance of perforated liners because it can not capture the real flow velocity in the porous media.

3.3.2 Physical Velocity Model

Superficial velocity porous media model can not reflect the flow velocity changes across the porous media model because the effect of porosity is ignored in the velocity related convective terms in the flow governing equations. By contrast, the

physical velocity model accommodates the effect of porosity in all the terms in Navier-Stokes equations. The following amended Navier-Stokes equations are resolved in physical-velocity porous media zones (Fluent, 2009):

$$\frac{\partial(\sigma\rho\phi)}{\partial t} + \mathrm{div}(\sigma\rho\phi\vec{\mathrm{u}}) = \mathrm{div}(\sigma\Gamma\,\mathrm{grad}\phi) + \sigma S_{\phi} \qquad (98)$$

When general scalar ϕ is 1, continuity equations inside the porous region and outside the porous region are respectively:

$$\frac{\partial(\sigma\rho)}{\partial t} + \mathrm{div}(\sigma\rho\vec{\mathrm{u}}) = 0 \qquad (99)$$

$$\frac{\partial\rho}{\partial t} + \mathrm{div}(\rho\vec{\mathrm{u}}) = 0 \qquad (100)$$

The magnitude of velocity vector $\vec{\mathrm{u}}$ within the porous region has to be amplified by a factor $1/\sigma$ for the transverse flow to satisfy the mass continuity. This resultant physical velocity is equivalent to the average real velocity within the porous material region. Therefore, mass flow rate conservation and the correct representation of velocity changes across the porous region are simultaneously achieved by applying the physical velocity porous media model. From another point of view, the inertial force a transverse flow is subjected to across the porous material is determined by the mass flow rate and the velocity change situations. Therefore, it is highly likely that the physical velocity model is able to represent the inertial resistance acting on the transverse flow by the porous media region and the approach of defining *a priori* inertial resistance in superficial velocity model is not necessary any more. Acquisition of the acoustic impedance of the porous region also becomes likely as well with the correct velocity representation in the porous region.

Therefore, physical velocity porous media model is applied in this work to represent the perforated liner region. The methods about how to define relevant properties of the porous media region are described below and the ability of the described methods in acquiring acoustic properties of perforated liners will be validated in future chapters.

3.3.3 Porosity

Porosity is the volume fraction of the space occupied by void fluid passages in the porous media region. Volume porosity is identical with the surface porosity if perforations are made perpendicular with the liner surface. However, In those situations (Eldredge & Dowling, 2003) where the axis of perforations is tilted at an angle (θ) with the liner surface as shown in Figure 11 in order to generate enhanced wall cooling effect, the effective length of the perforation l_{thic} is enlarged by a factor of $1/\sin\theta$ and the volume porosity is larger than surface perforation rate by the same factor of $1/\sin\theta$ as well.

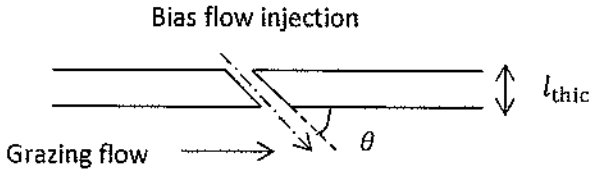

Figure 11 Flow conditions near an inclined perforation

CFD representation of these inclined orifices can be carried out in two ways. The first way is to keep the volume porosity identical with the surface porosity and at the same time to define the thickness of porous media region to be the axial length of perforations. The second way is to apply real volume porosity and real liner thickness and, at the same time, to impose a much higher flow resistance in the radial and tangential directions of inclined perforations so that the flow is forced to only develop in the axial direction of those perforations. The second approach is adopted in this work because it is able to generate more realistic effusion cooling flow effects compared with the first approach.

3.3.4 Viscous Resistance

Energy and pressure loss of a flow across a perforated liner is attributable to two types of flow resistance: viscous resistance and inertial resistance (Crandall, 1954). Viscous resistance is due to the viscous shear stress between those flow layers at different velocities and the presence of wall roughness as well. Viscous loss due to the friction between flow and rough boundaries largely depends on manufacturing quality of the liner surface and is hard to quantify. However, the latter source of

pressure drop due to viscous shear stress between different flow velocity layers coincides with the classical fluid dynamics problem of a laminar flow in small tubes. Hagen-Poiseuille equation (Sutera & Skalak, 1993; Yunus & Cimbala, 2006) has been directly derived from Navier-Stokes equations and the pressure drop of steady laminar flow through a long constant-cross section tube due to viscous shear stresses is expressed as:

$$\Delta P = \frac{32\mu l U}{d^2} \qquad (101)$$

where μ stands for the dynamic viscosity of air; l and d are the length and hydraulic diameter of the tube respectively; U is the flow velocity in the tube. Equation (101) is obtained under the assumption of steady state laminar flow.

Viscous resistance is related to the diameter of the perforations according to Equation (101). However, the porous media model assumes the porous region as a uniform flow region and geometry details of perforations are ignored. As a consequence, the orifice size dependent viscous resistance is beyond calculation ability of the current porous media model. Therefore, viscous resistance of the perforated liners has to be manually imposed to be the viscous resistance of the porous media region. In this work, the steady-state viscous effect is approximated by Equation (101) and is taken into account by imposing the viscous resistance in the source term in Equation (97) for zero mean bias flow cases. For example In ANSYS FLUENT (Fluent, 2009), the pressure drop due to the viscous resistance is expressed as:

$$\Delta P = \frac{\mu}{\alpha} l U_{\text{sup}} \qquad (102)$$

where α is permeability of porous region, U_{sup} is superficial velocity $U_{\text{sup}} = U\sigma$. Combine Equation (101) and Equation (102) , the viscous resistance of a porous media region in ANSYS Fluent in the perforation axial direction can be defined according to:

$$\frac{\mu}{\alpha} = \frac{32\mu}{\sigma d^2} \qquad (103)$$

Directions other than the flow direction such as the radial and tangential directions of perforations are defined to be with viscous resistances that are 100-200 times larger than the viscous resistance in the axial direction so that the flow only develops in the perforation axial direction within perforated liners.

It is also noteworthy at this point that, "viscous resistance" and "flow resistance" of a porous material shares the same mathematical definition to be the pressure drop divided by the resultant neck velocity. However, the term "viscous resistance" is to describe the pressure loss purely due to viscous effect while "flow resistance" is a more general term which can be a result of both viscous effect and inertial effect.

3.3.5 Inertial Resistance

Physical velocity porous media model as described by Equation (99) is able to capture flow velocity changes across the perforated plate. In addition, the mass flow rate of the flow experiencing these velocity changes is a conserved quantity in CFD calculations. A transverse flow is subjected to inertial resistance due to the abrupt changes of velocities across perforated liners and inertial resistance is determined by magnitude of the velocity change and the mass flow rate taking part in the velocity change. Therefore, physical velocity model itself is able to account for inertial resistance a flow is subjected to across perforated liners. As a result, inertial resistance which has to be defined as *a priori* in superficial velocity model does not need to be defined *a priori* in the physical velocity porous media model and is kept to be zero.

When large scale of bias flow exists, pressure drop due to inertial resistance is dominant over that due to viscous resistance. This can be explained by Darcy-Forchheimer Law (Huang & Ayoub, 2008):

$$\Delta P = -(C_v U + C_i U^2) \qquad (104)$$

where C_v and C_i are the viscous loss coefficient and the inertial loss coefficient respectively. Equation (104) indicates that pressure loss due to viscous resistance increases linearly while that due to inertial effect shows a quadratic rise with the neck velocity. As a result, the pressure drop due to inertial resistance dramatically climbs at high bias flow velocities and brings down the proportion of pressure loss

due to viscous effect. On the other hand, when the neck flow velocity is very low, e.g. neck flow velocity is less than 1m/s, viscous effect plays an important role in determining overall resistance and this effect is more significant if the orifice size is small. Two example calculations of viscous resistance and inertial resistance at $U = 0.5\mathrm{m/s}$ and $U = 5\mathrm{m/s}$ are provided below for the plate shown in Figure 10(b).

Pressure drop due to viscous resistance in the perforation is approximated by Equation (101):

$$\Delta P_v \cong \frac{32\mu l U}{d^2} = \frac{32 \times 1.78 \times 10^{-5}\mathrm{kg/(ms)} \times 0.003\mathrm{m} \times 0.5\mathrm{m/s}}{(0.0025\mathrm{m})^2} = 0.137\mathrm{Pa}$$

$$\Delta P_v \cong \frac{32\mu l U}{d^2} = \frac{32 \times 1.78 \times 10^{-5}\mathrm{kg/ms} \times 0.003\mathrm{m} \times 5\mathrm{m/s}}{(0.0025\mathrm{m})^2} = 1.37\mathrm{Pa}$$

Discharge coefficient C_d for a typical perforated plate falls in between 0.6-0.85 in the presence of mean through flows (Kolodzie & Van Winkle, 1957; Smith & Van Winkle, 1958). Discharge coefficient is taken to be 0.75 in current calculations:

$$\Delta P_i = \frac{\rho U^2}{2C_d^2} \cong \frac{1.177\mathrm{kg/m\text{^}3} \times (0.5\mathrm{m/s})^2}{2 \times 0.75^2} = 0.262\mathrm{Pa}$$

$$\Delta P_i = \frac{\rho U^2}{2C_d^2} \cong \frac{1.177\mathrm{kg/m\text{^}3} \times (5\mathrm{m/s})^2}{2 \times 0.75^2} = 26.2\mathrm{Pa}$$

As can be seen from above calculations, the contribution of viscous resistance is much smaller than the inertial resistance when significant mean bias flow is present. What is more, approximation of the viscous resistance by Hagen-Poiseuille equation tends to overestimate the viscous resistance when flow detachment occurs due to strong neck flow. Therefore, in this work, viscous resistance is calculated and defined according to Equation (101) when mean flow is not present. It is, on the other hand, simply neglected in the presence of bias flows where $M_b > 0.01$. Inertial resistance is left as 0 in the model and we propose that the physical velocity model itself is able to capture the inertial resistance the flow is subjected to thanks to its capacity to capture the flow velocity changes.

3.3.6 Grazing Flow Induced Flow Resistance

Grazing flow is the flow which travels parallel with the perforated liner surface. The net flow rate through the perforated liner is zero if the liner is backed by a closed cavity, regardless of the presence of the grazing flow in the duct. However, grazing flow impacts on the perforation wall and thus causes local flow in the perforations as shown in Figure 12 (Sullivan, 1979; Tonon et al., 2013). The non-uniform local neck flow increases the flow resistance of the liner due to inertial effect. However, the extra inertial resistance due to non-uniform neck flows is beyond the capability of the porous media model because it ignores geometry details of perforations and treats the perforated liner as a homogenous flow region. Therefore, grazing flow induced flow resistance has to be taken into account by imposing *a priori* grazing flow resistance for the porous media region in CFD calculations.

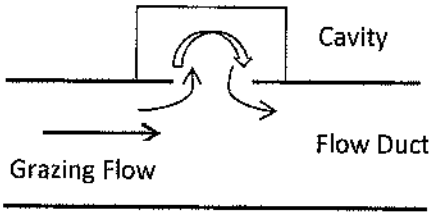

Figure 12 Illustration of grazing flow induced neck flow in a single perforation

According to experiments by Rice and Syed et al. (Rice, 1971; Dean & Tester, 1975; Jing et al., 2001; Syed et al., 2002), grazing flow induced specific flow resistance is proportional to grazing flow Mach number:

$$r_g = \frac{C_g M_g}{\sigma} \qquad (105)$$

The proportional constant C_g is different across different experiments. C_g is claimed to be 0.3 in some experiments (Rice, 1976; Bauer, 1977; Jing et al., 2001), and it is argued to be 0.5 in some other experiments (Rice, 1976; Rao & Munjal, 1986). Heidelberg et al. (1980) confirmed that the coefficient C_g varies with the dimension of perforations and according to him:

$$r_g = \frac{M_g}{\sigma} / (2 + 1.256\frac{\delta}{d}) \qquad (106)$$

where δ is "boundary layer thickness displacement". Syed et al. (2002) found that δ is approximately 1.45mm and hardly changes above certain grazing flow speeds. Therefore, grazing flow induced normalized specific flow resistance of the porous media region in CFD simulations is approximated in this work as:

$$r_g = \frac{M_g}{\sigma} / (2 + \frac{0.0018}{d}) \quad (107)$$

Proportional constant varies from 0.5 for large perforations to 0.25 for small perforations. The dependency of grazing flow effect on orifice sizes is intuitively understandable: stronger local neck flow will be induced in a larger perforation due to the larger flow gap open to grazing flow impact.

Grazing flow and bias flow coexists in gas turbine combustion chambers. Several experiments have found that grazing flow is important only when mean bias flow through the neck is relatively weak (Rice, 1971; Dean & Tester, 1975; Lahiri, 2014). Lahiri (2014) found that grazing flow provides similar sound attenuation effect with the bias flow if $M_b/M_g = 1/3$ and the effect of grazing flow alone could be ignored if $M_b/M_g > 1/3$. Similarly, Rice (1971) proposed the ratio M_b/M_g to be 0.3 above which grazing flow effect is negligible. Otherwise, grazing flow induced resistance is dominant over bias flow induced resistance. Both authors (Rice, 1971; Lahiri, 2014) indicated that the overall flow resistance of a perforated liner is dominant either by bias flow or grazing flow and it was reasonable to take the larger resistance as the overall resistance of the liner. Bias flow induced flow resistance is directly solvable by the physical velocity porous media model as has been discussed. However, the grazing flow effect is totally ignored by the homogenous model. As a consequence, flow resistance of the porous media region should be supplemented by the difference between grazing flow induced resistance and the resolved bias flow resistance in a CFD simulation for grazing flow dominant flow conditions.

$$r_{g-b} = \begin{cases} 0 & \text{if } r_b > r_g \text{ or } r_g = 0 \\ \frac{C_g M_g}{\sigma} - r_b & \text{if } r_b < r_g \\ \frac{C_g M_g}{\sigma} & \text{if } r_b = 0 \end{cases} \quad (108)$$

where $C_g = 1/(2 + 0.0018/d)$ according to Equation (107). r_b is the bias flow induced flow resistance which is to be determined by a separate CFD calculation using physical porous media model in the presence of bias flow only. The empirical inclusion of *a priori* grazing flow induced resistance appears to reduce the numerical robustness of the proposed porous media model. However, flow resistance of a perforated liner is, in most cases dominant by bias flows in the real gas turbine combustors thanks to the relatively low grazing flow Mach number near the liner region.

Boden et al. (Rademaker et al., 2011; R.Kabral, 2014; Bodén & Kabral, 2015) recently found that the linear relationship between grazing flow Mach number and the resulting flow resistance remains valid in high temperature flows and the effect of flow temperatures on the flow resistance is negligible. Therefore, the approach of defining flow resistance as described in Equation (108) remains valid in high temperature flow conditions.

3.3.7 Plate Thickness and End Corrections

Acoustic effective thickness of a perforated liner is larger than its real thickness due to the acoustic radiation effect at the rim of orifices. However, porous media model ignores geometry details of perforations and, as a result; the additional thickness due to end radiation effect can not be represented. Therefore, the thickness of the porous media region in CFD simulations has to be equal to the effective thickness of the liner rather than the real liner thickness.

Effective thickness of an orifice through an infinite large plate without the presence of mean flow was analytically derived by Rayleigh et al. (Rayleigh, 1940; Bolt et al., 1949; Ingard, 1953):

$$l_{\text{eff}} = l_{\text{thic}} + 8r/3\pi \approx l_{\text{thic}} + 0.85d \qquad (109)$$

Other researchers (Ingard, 1953; Melling, 1973) found that the end correction length would be reduced by the acoustic interaction effect between neighboring holes. Melling (1973) analyzed the hole-hole interaction effect by referring to Fok's function Ψ (Fok & Brocklesby, 1941).

$$\Psi = 1 - 1.4092\sqrt{\sigma} + 0.33818\sigma^{1.5} + 0.06793\sigma^{2.5} \quad (110)$$

Mellling (1973) plotted the Fok's function against $(2r_0)/D$ where r_0 is perforation size and D represents the perforation separation distance. He found that hole-hole interaction effect is very small when $(2r_0)/D < 0.2$ because the holes are too far away from each other. Fok's function is simplified to $\Psi = 1 - 1.4\sqrt{\sigma}$ and will be used in this work only if $2r_0/D > 0.2$.

$$l_{\text{eff}} = l_{\text{thic}} + 0.85d(1 - 1.4\sqrt{\sigma}) \quad (111)$$

High particle velocity or mean bias flow in the orifice was found to be able to reduce end correction effect as well (McAuliffe, 1950; Ingard, 1959). Maa (1996) proposed an extra correction term due to high orifice velocities:

$$l_{\text{eff}} = l_{\text{thic}} + 0.85d(1 - 1.4\sqrt{\sigma})\left(1 + \frac{\mathrm{M}}{\sigma}\right)^{-1} \quad (112)$$

where M is the neck particle Mach number. It is common to suppose that the high particle velocity and the bias flow reduce end correction length due to the same physical mechanism (Dean & Tester, 1975; Elnady, 2004; Lahiri, 2014) and the neck particle Mach number in Equation (112) could be replaced by the flow Mach number in the neck to take bias flow effect into account.

$$\mathrm{M} = \frac{\left[U_b + \sqrt{2}\mathrm{rms}(U_{\mathrm{ac}})\right]}{c} \quad (113)$$

Inspired by Bellucci et al.(2004), the minimum bias flow correction factor is limited to 0.33 in this work.

A number of experiments found that acoustic end correction length would decrease due to the presence of grazing flow. Rice (1971) proposed a correction factor of $1/(1 + 305\mathrm{M}_{\mathrm{g}}^3)$ for the end correction length correction. However, this correction term would significantly underestimate the effect of grazing flow according to some other researchers (Jing et al., 2001; Elnady & Boden, 2003). Elnady and Boden (2003) simply introduced an grazing flow acoustic reactance term $-0.3\mathrm{M}_{\mathrm{g}}/\sigma$. However those experiments by Kooi, Kirby and Kaji et al. (Kooi & Sarin, 1981; Kaji et al., 1984; Kirby & Cummings, 1998; Jing et al., 2001) clearly showed that the acoustic reactance did not decrease linearly with the grazing flow Mach number as

suggested so by Elnady and Boden (2003). According to Kirby and Cummings (1998), the end correction length was not affected by slow grazing flows until it started to decline rapidly above certain the grazing flow Strouhal number and the decrease of end correction length slows down with increasing grazing flow speed. Kaji et al. (1984) found the same trend that decrease of reactance slowed down with increasing grazing flow velocity and the decrease nearly stopped if $M_g > 0.15$.

Grazing flow reduces end correction length in two ways. First, grazing flow induced local neck flow reduces end correction length in the same way with the bias flow and this is described in Equation (112). Second, grazing flow blows away' part of the end correction length at the flow side. Correction factor for end correction length due to 'blow away' effect is slightly lower than 0.5 at high grazing flow Mach numbers ($M_g > 0.15$). Correction factor can be slightly below 0.5 when the high speed grazing flow blows away all the end correction length at the flow side and also "blows away" some air mass from the internal rim of orifices. The effective thickness of perforated liners is thus proposed to be:

$$l_{\text{eff}} = l_{\text{thic}} + 0.85\text{d}\left(1 - 1.4\sqrt{\sigma}\right) \Big/ \begin{cases} 1 + \dfrac{M_b}{\sigma} & \text{if } M_g = 0 \\ (1 + 10M_g)\left(1 + \dfrac{M_b}{\sigma}\right), & \text{if } M_b/M_g > C_g \\ \left(1 + 10M_g\right)\left(1 + \dfrac{C_g M_g}{\sigma}\right), & \text{if } M_b/M_g < C_g \end{cases} \quad (114)$$

The term $(1 + 10M_g)$ considers the end correction 'blow away' effect by the grazing flow. This term is no greater than 2.5 because the 'blow away' effect takes place only at the grazing flow side of the liner and does not affect the end radiation effect at the cavity side of the liner. The second term $(1 + C_g M_g/\sigma)$ is to reflect the local neck flow effect and this term will be replaced by $1 + M_b/\sigma$ if the mean bias flow effect is stronger than the local flow effect.

3.3.8 Turbulence Modelling in the Porous Media Region

As stated in Section 3.3.4, most bias flows in gas turbine perforated liners fall into laminar flow regime. However, turbulence models will be adopted to simulate flows in the other regions if the flow Reynolds number exceeds 3500. In addition, micro-

scale turbulence could develop at lower Reynolds number in the small holes due to strong upstream and downstream disturbance (Macdonald et al., 1979; Antohe & Lage, 1997). This section looks into how turbulence should be treated in the porous media model.

The turbulence structures emerging in the perforations are obviously smaller than the perforation geometry itself. On the other hand, there are often only 2-3 layers of meshes in the direction of perforation thickness in the CFD simulations. As a result, the micro-scale turbulence features in the perforations can not be well represented due to the low resolution of meshes. From the other perspective, increase of the number of cells in the liner region does not improve the turbulence solution because micro-scale flow details are totally absent within the homogenous porous media model.

A next issue is that whether the turbulence modelling should be totally turned off in the porous media model. In the $\kappa - \varepsilon$ model approach, turbulence kinetic energy in i direction is defined as:

$$\kappa = \frac{1}{2}\overline{u_i'^2} \qquad (115)$$

where u_i' is the turbulent velocity fluctuation. The porous media model as described by Equation (98) is able to obtain physical velocity within the porous media region by placing the porosity into all terms in Navier-Stokes equations. However, at the same time, all turbulent velocity terms in the porous media region are obtained by simply multiplying a factor of $1/\sigma$ to its original values. Turbulence kinetic energy in the porous material model becomes:

$$\kappa = \frac{1}{2\sigma^2}\overline{u_i'^2} \qquad (116)$$

While it is correct that mean flow velocity is accelerated by $1/\sigma$ inside the porous region compared with that outside the porous region. However, it is a serious exaggeration to assume that turbulent fluctuation is increased by the same factor $1/\sigma$ and turbulence kinetic energy is increased by $1/\sigma^2$. As a consequence, application of $\kappa - \varepsilon$ turbulence model in the porous media region tends to seriously

overestimate energy and pressure loss due to the seriously exaggerated turbulence strength. To summarize, turbulence details in the perforated liner region can not be reasonably represented by traditional turbulence solution strategies in the porous media model. Modelling of turbulence has to be turned off in the porous media region regardless of the turbulence model applied in other flow regions.

3.4 Acoustic Boundary Conditions

3.4.1 Non-Reflecting Flow Boundaries

Correct definition of acoustic properties of boundaries is vital for a CFD simulation to accurately resolve the internal acoustic field and it can be achieved in two ways. The first approach is to expand the calculation domain until acoustic reflections from the calculation domain boundaries can hardly exert impact on the acoustic field in the regions of interest (Roux et al., 2005; Singh, 2012). The second approach is to accurately define acoustic impedance of near-field boundaries. However, the acoustic impedance of boundaries is often not *a priori* parameter. In this work, the first approach is adopted if the acoustic impedance of near-field boundaries is unknown such as in the simulations of experiments by Eldredge and Roux et al.(Eldredge & Dowling, 2003; Roux et al., 2005) On the other hand, a general non-reflecting boundary condition (NRBCs) is applied in CFD calculations to represent those anechoic boundaries in experiments such as those by Jing and Houston et al.(Jing & Sun, 2002; Houston et al., 2015b)

The non-reflecting boundary proposed by Poinsot et al. (Poinsot et al., 1992; Selle et al., 2004b) allows outgoing waves to leave the boundary but artificially cancels the incoming waves entering the domain by imposing a "spring force" at the boundary. By this method, the incoming waves are diminished and will not couple with internal acoustic field. The amplitude of the incoming pressure wave at a pressure outlet is computed by a linear relaxation method (LRM) (Selle et al., 2004b). The Linear relaxation method sets the incoming wave amplitude to be proportional to the difference between the calculated variable on the boundary and the imposed boundary value. The amplitude of the incoming pressure wave on a pressure outlet boundary is expressed as:

$$L_1 = K(P - P_{exit}) \quad (117)$$

where P_{exit} is the imposed pressure at the exit boundary, K is a relaxation factor, and P is the local calculated pressure value at the boundary.

3.4.2 Representation of Acoustic Source

An acoustic source such as loudspeakers are typically either placed at one end of impedance tube or installed opposite each other at the side walls of flow duct. The latter loudspeaker position is difficult to achieve in a CFD simulation. Opening extra boundaries on the mean flow duct walls for acoustic signal introduction will lead to unrealistic flow field disturbance due to the interaction between the opening and incident mean flow. It is neither acceptable to simply use a neighbouring mean flow boundary as the acoustic signal inlet because the intrinsically reflecting loudspeaker will modify the original acoustic properties of the flow boundary.

In this work, the loudspeakers which are placed in the side wall of flow ducts in the experiments as shown in Figure 14 are relocated to its neighbouring mean flow boundary in CFD simulations. The flow inlet or outlet near loudspeakers is divided into two parts as shown in Figure 13. A small area in the middle of the boundary is treated to be the acoustic signal inlet. The area of acoustic signal inlet covers less than 1/10 of the overall area of the flow boundary so that the original acoustic property of this boundary is not altered. The acoustic signal is introduced through the small area by imposing predetermined transient acoustic pressure, mass flow rate or velocity information at each time step. The type and strength of the acoustic signals applied in validation simulations are duplicated signals applied in those validation experiments.

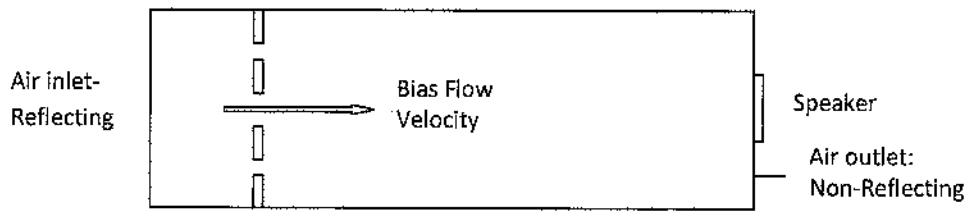

Figure 13 An illustration of loudspeaker representation in the CFD simulation for experiment of Bellucci et al. (2004)

3.5 Mesh Building, Time Step and Discretization Schemes

Thickness of perforated liners has significant impact on overall acoustic properties of liner absorbers. Therefore, the quality of grid representation in liner thickness direction is crucial for a CFD calculation to predict acoustic properties with least errors. In this work, 2-4 layers of orthogonal structured hexahedral meshes are built within the porous media region in the liner thickness direction. Unstructured tetrahedral mesh is not used within the porous media region to avoid any possible numerical errors due to mesh skewness (Versteeg & Malalasekera, 2007).

Meshes in other regions satisfy several other basic requirements. First, all the test rig geometries has to be numerically accurately represented. At least 20 layers of meshes are guaranteed in the radial direction of a flow duct. Second, flow Courant number is ensured to be not much greater than unity in the calculation domain, though implicit temporal scheme is employed, in order to achieve high numerical accuracies. Third, a time period of the highest frequency signal is coved with no less than 20 time steps. Extra mesh and time step requirements are to be met for large eddy simulations and will be introduced in the last chapter of the thesis.

Acoustic velocity and pressure are very small compared with mean flow velocity and pressure. Therefore, the spatial terms are discretized with second order accuracy by the second order upwind scheme. Bounded second order implicit temporal scheme is applied to capture the subtle but rapid acoustical pressure change in this work. Bounded second order implicit scheme provided both the numerical accuracy of second order upwind scheme and the convergence robustness of the first order scheme (Fluent, 2009). All CFD simulations are carried out by solving three dimensional compressible Navier-Stokes equations in ANSYS FLUENT 17.2. The compressibility of air is represented by ideal gas state equations. Navier-Stokes governing equations are resolved in the double-precision FLUENT solver so that more precise acoustic information can be retrieved from higher precision calculations. Acoustic information is taken to be the static pressures at positions where microphones are placed and the acoustic information is not

collected until both the mean flow and acoustic field reach statistically and numerically stable states.

3.6 Summary

Nine points should be followed in order for CFD simulations to obtain the accurate prediction about acoustic properties of perforated liners:

1. The porosity of porous media region is defined to be the volume porosity rather than the surface porosity in cases of inclined orifices.
2. The porous media region is built with effective thickness of a liner rather than real thickness of the liner.
3. Physical velocity model rather than superficial velocity model is applied in order to obtain correct flow velocity in the porous media region.
4. Turbulence modelling in the porous media zone has to be suppressed. Flow through the perforated liners is treated as laminar flow.
5. Viscous resistance in the axial direction of perforation should be included according to Hagen-Poiseuille equation and this is especially important for liners with small perforation size in the absence of mean flow. Grazing flow induced flow resistance has to be accommodated into the porous media model as well. Viscous resistance in radial and tangential directions of perforations should be defined to be 100-200 times larger than the axial direction resistance to guarantee correct flow direction in the liner.
6. Acoustical reflection properties of boundaries should either be directly resolved or accurately imposed with their acoustic impedance. Anechoic boundary is treated as non-reflecting boundary in CFD simulations.
7. The type and strength of acoustic signal in CFD simulations should be identical with the signal applied in the validation experiments. Acoustic signal should be introduced through a small area on a flow boundary.
8. Mesh has to be structured in the perforated liner region and tetrahedral meshes are not preferred to avoid any possible numerical error.

9. The compressible Navier-Stokes equations are discretized by numerical schemes with at least second order accuracy. Air should be treated as ideal gas or real gas rather than a medium with constant density.

4. Validation of the Porous Media Model in Predicting Acoustic Properties of Perforated Panel Absorbers

4.1 Review and Objectives

The final aim of this research is to validate that the proposed methodology in Chapter 3 is able to predict acoustic attenuation properties of perorated liners in real gas turbine combustors. However, simulations of the swirling and reacting flows in a real gas turbine combustor are open to a number of numerical and modelling sources of errors, and it is difficult to validate the porous media model in the presence of so many other sources of errors. Therefore, the proposed methodology in Chapter 3 is firstly applied and validated in this chapter in zero mean flow conditions prior to being applied to simulate more complex flows. Acoustic properties of perforated panel absorbers without the presence of mean flow are resolved in a compressible laminar flow CFD solver and simulation results are compared to a number of well-cited experiments.

Acoustic attenuation effects of perforated panel absorbers depend on both those geometry features of perforations and cavities and also the incident signals. Past experimental research has intensively investigated the effects of geometry features such as perforation rate, plate thickness, number of plate layers (Jones et al., 2002; Lee & Kwon, 2004; Jung et al., 2007), the size and shape of perforations (Miasa et al., 2007; Li & Mechefske, 2010; Vigran, 2012) and geometry of the perforated panel and air cavity (Liu & Herrin, 2010; Lahiri, 2014). Incident signal intensity (Ingard & Ising, 1967; Cummings, 1984; Maa, 1996; Jing & Sun, 2002; Heuwinkel et al., 2009; Tayong et al., 2010) and signal incidence angle (Jones et al., 2002; Liu, 2011; Yang et al., 2013) have been experimentally studied as well.

In addition to experimental works, a few acoustic impedance models have been acquired by analytical derivations and experimental regressions. Well-known models include Maa's model (Maa, 1998) which is proposed for micro-perforated panel absorbers, Atalla and Sgard's model (Atalla & Sgard, 2007) which is proposed for perforated screens. Maa's model is only applicable to absorbers with small sized

perforations while Atalla's Model is applicable to medium sized perforated panel absorbers. Maa, Ingard and Melling et al. (Ingard & Ising, 1967; Melling, 1973; Maa, 1996) also proposed correction terms to account for the effect of high neck particle velocity on acoustic impedance of perforated liners. Details about these acoustic impedance models are given in Chapter 2.

In the chapter, the CFD method described in Chapter 3 will be applied to revisit three well-acknowledged experimental works and two specifically designed experiments by University of Hull (Melling, 1973; Jing & Sun, 2002; Lee & Kwon, 2004; Houston et al., 2015a; Houston et al., 2015b). CFD and experimental results will be compared in terms of effects of porosity, signal incidence angle, incident sound pressure level, and the number and the array of panel layers on acoustic absorption properties of perforated panel absorbers.

4.2. Validation Experiments

4.2.1 Experiment by Houston and Wang

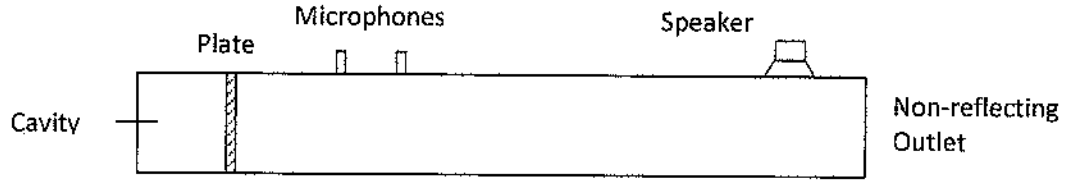

Figure 14 Schematic view of impedance tube setup for panel absorbers HA, HB, HC (Houston et al., 2015a)

Table 1 Geometric specifications of perforated panel HA, HB, HC

Plate	Hole diameter	Thickness	Porosity
HA	1mm	2mm	0.38%
HB	1mm	2mm	1.23%
HC	3mm	2mm	3.41%

As a part of this work, the acoustic absorption properties of six perforated panel absorbers were experimentally investigated by University of Hull, Acoustic Research Centre. In the first experiment (Houston et al., 2015a), three perforated panels (HA,

HB and HC) were placed at one end of a Ø78mm circular impedance tube and were backed by a 55mm deep air cavity as shown in Figure 14. The geometric features of Plate HA, HB and HC are listed in Table 1. A random sound signal with a flat acoustic energy spectrum within 100Hz-1200Hz was introduced by the loudspeakers at the other end of the impedance tube. The overall incident sound pressure level was 105dB for plate HA and HC and 110dB for plate HC. Transient pressure data were collected and processed by the two-microphone transfer function method as described in Section 2.4.1.

In the second experiment (Houston et al., 2015b), the other three 50mm×59.4mm rectangle plates H1, H2 and H3 were mounted in flush with the side wall of a Ø165mm flow duct and were backed by a 51mm deep fan-shaped cavity as shown in Figure 15. The other end of the cavity was either a closed wall or installed with a second layer of perforated plate. The outer plate as shown in Figure 16 is H1-out, H2-out, H3-out for inner plate H1, H2 and H3 respectively. Detailed geometric features of all perforated panels are listed in Table 2. Incident signal was a 115dB 200Hz-1000Hz random signal which was introduced by loudspeakers on the upstream flow duct wall. Pressure data were collected at four different locations as shown in Figure 15 and processed by the two-microphone transfer function method as described in Section 2.4.2.

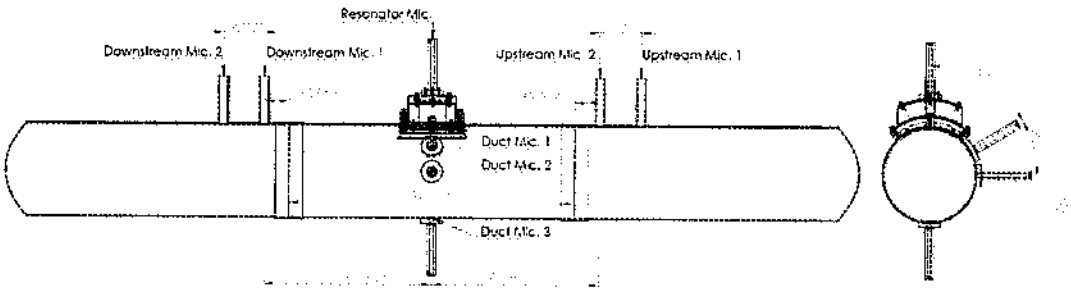

Figure 15 CAD Drawing of flow rig measurement section (Houston et al., 2015b)

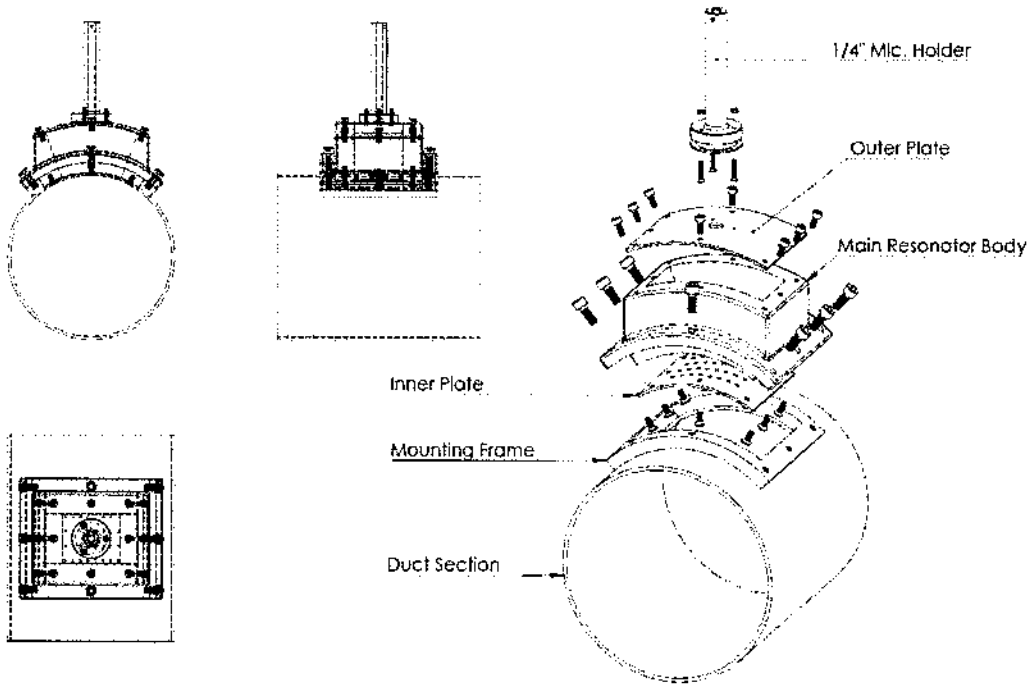

Figure 16 Assembly CAD drawing of the Resonator design (Houston et al., 2015b)

Table 2 Geometry features of perforated panel H1, H2, H2 and corresponding outer plates H1-out, H2-out, H3-out (Houston et al., 2015b)

Plate	Hole size	Holes Number	Plate Dimension	Porosity
		Inner Liner		
H1	2mm	32	50×59.4mm	3.38%
H2	3mm	32	50×59.4mm	7.62%
H3	4mm	32	50×59.4mm	13.5%
		Outer Liner		
H1-out	1mm	20	50×97mm	0.324%
H2-out	2mm	12	50×97mm	0.775%
H3-out	2mm	20	50×97mm	1.30%

4.2.2 Experiment of Lee and Kwon's

Experiment of Lee and Kwon's (2004) are re-visited by the proposed CFD methodology in order to investigate effects of porosities, multi-layer perforated panels and effect of array of perforated plates. Test rig setup of this experiment is very similar to the impedance tube setup as shown in Figure 14. Four plates (L1, L2,

L3 and L4) have been experimentally tested and they were of the same thickness of 1mm and the same orifice diameter of 2mm. Perforation rates of L1, L2, L3, L4 were respectively 1.40%, 3.14%, 5.59% and 7.07% by changing hole to hole separation distances. The perforated panels were placed in a one metre long 60mm×60mm square impedance tube. Each layer of perforated panel was backed by a 70mm deep air cavity. Signal used was a random noise signal and the incident sound pressure level was kept below 102dB to avoid any non-linear absorption effect. Transient pressure data were collected and processed by the two-microphone transfer function method as described in Section 2.4.1.

4.2.3 Experiment of Melling's and Jing's

Linear absorption regime is the regime where acoustic attenuation effect of a sound absorber barely changes with the incident sound pressure levels. Inertial resistance of the absorber is small compared with viscous resistance in linear absorption regime. On the contrary, inertial resistance becomes significant in non-linear regimes due to high neck particle velocities. As a result, variations in incident sound pressure levels could alter the overall noise attenuation effect of an absorber in the non-linear absorption regime.

Past research has indicated that plates with smaller porosities and smaller perforation sizes tend to reach non-linear absorption regime at lower sound pressure levels compared with those with a larger porosity (Melling, 1973; Tayong et al., 2010; Lahiri, 2014). Therefore, a perforated plate with a larger porosity is taken from the experiment by Melling (1973) and a second orifice plate with a smaller porosity is taken from the experiment by Jing and Sun (2002) and their response to high incident sound pressure levels are revisited by the proposed CFD method. Details about the two cases are provided in Table 3.

Table 3 Some details about Melling's and Jing's Experiment

Plate	Porosity	Hole Diameter	Incident SPL	Plate Thickness
Melling's RT335/00	7.6%	2.8mm	116-160dB	0.56mm
Jing's	0.5%	8mm	96-144dB	0.1mm

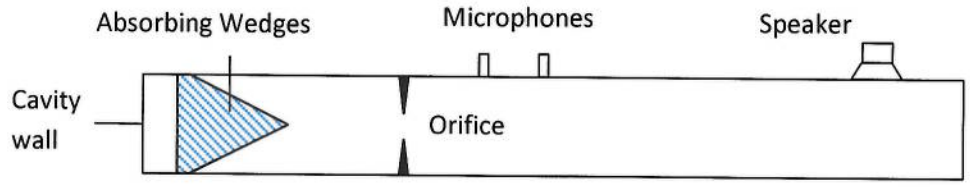

Figure 17 Experimental test rig setup of the experiment by Jing and Sun (2002)

The experimental test rig in Melling's experiment was similar with the impedance tube as shown in Figure 14. CFD calculations are carried out for the case where plate RT335/00 backed with a 25.4mm deep cavity was incident by a 1130Hz sine-wave signal. Jing and Sun's experiment featured a single Ø8mm circular orifice in the middle of a 100mm×100mm square plate as shown in Figure 17. Downstream cavity was filled with sound attenuation material so that acoustic wave reflection from the cavity was negligible. The sound signal used in his experiment was a 200Hz sine wave. Transient pressure data were collected and processed by the one-microphone transfer function method proposed by Chu (1986) as mentioned in Section 2.4.1.

4.3. Results and Discussion

The acoustic signal normal incidence on a perforated liner can be compared to a serial connection of electrical resistances as shown in Figure 18 (Liu, 2011). Pressure loss is additive $p = \Delta p + p_A$ and particle flow rate is continuous across the plate. The overall specific acoustic resistance is calculated as:

$$\frac{p}{us_1} = \frac{\Delta p}{us_B} + \frac{p_A}{us_A} \quad (118)$$

$$Z/s_1 = Z_A/s_A + Z_B/s_B \quad (119)$$

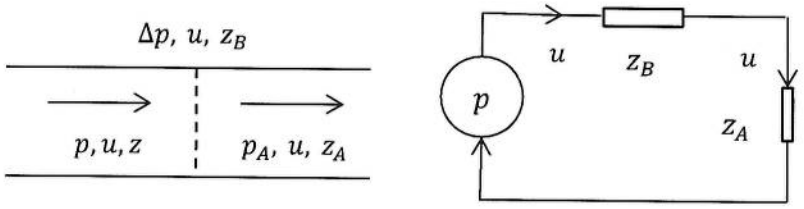

Figure 18 Electro-acoustic analogy for normal signal incidence cases (Liu, 2011)

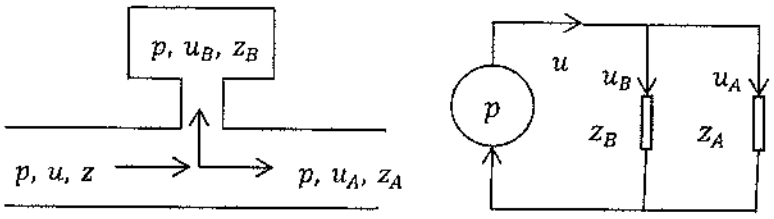

Figure 19 Electro-acoustic analogy for parallel signal incidence cases (Liu, 2011)

The acoustic signal grazing incidence on a perforated liner can be compared to a parallel connection of electrical resistances as shown in Figure 19 (Liu, 2011). Pressure difference across the cross dimension of the liner is small if the liner is much smaller than wavelength of signal. According to flow continuity, volume flow rate $\dot{V} = \dot{V}_A + \dot{V}_b$ and $\dot{V} = u \cdot s$. Therefore, $us_1 = u_A s_A + u_B s_B$ and:

$$\frac{us_1}{p} = \frac{u_A s_A}{p} + \frac{u_B s_B}{p} \quad (120)$$

$$\frac{s_1}{Z} = \frac{s_A}{Z_A} + \frac{s_B}{Z_B} \quad (121)$$

As can been seen, installation of a same perforated liner could result in very different overall acoustic impedance depending on signal incidence angles, the acoustic impedance of surroundings and also the relative size of liner.

4.3.1 Normal Signal Incidence

Figure 20 shows typical mesh distribution for CFD calculations of normal incidence tests in an impedance tube. 2-3 layers of meshes are built in the thickness direction of the perforated plate. At least 20 meshes are built in the radial direction of the impedance tube and at least 20 meshes are guaranteed within one wavelength of the tested signals in the sound propagation direction.

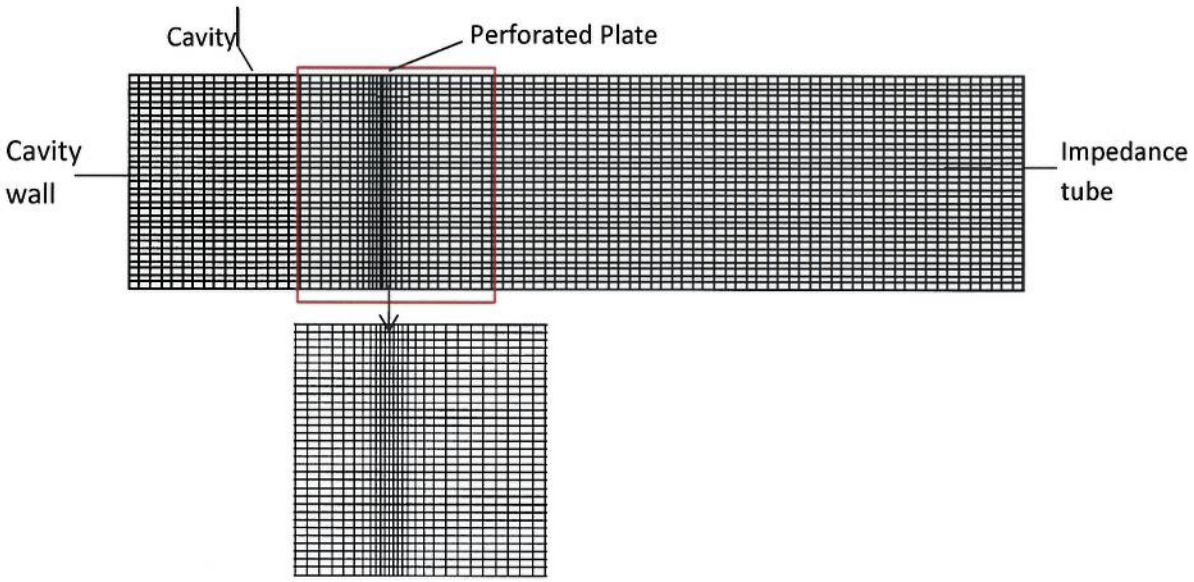

Figure 20 Meshes distribution in an impedance tube

Figure 21, Figure 22 and Figure 23 compare the absorption coefficient curves acquired by experiment, CFD, Maa's model and Atalla's model for three different panel absorbers made of perforated plates HA, HB, HC respectively. First, results given by all four methods indicate that peak absorption frequency increases from approximately 260Hz to 475Hz and 600Hz when the porosity of liners rises from 0.38% to 1.23% and 3.41%. Optimum absorption coefficient declines and absorption bandwidth widens with the increasing liner porosities. Plate HC absorber exhibits much weaker overall attenuation effect than HA and HB absorbers do. This is because the porosity of plate HC and the size of perforations are much larger so that the viscous resistance of plate HC are much lower. Maa's theory fails to yield reasonable result for plate HC because the 3mm perforation size pushes HC absorber beyond the application scope of Maa's model in terms of Shear number as described in section 2.3.2.

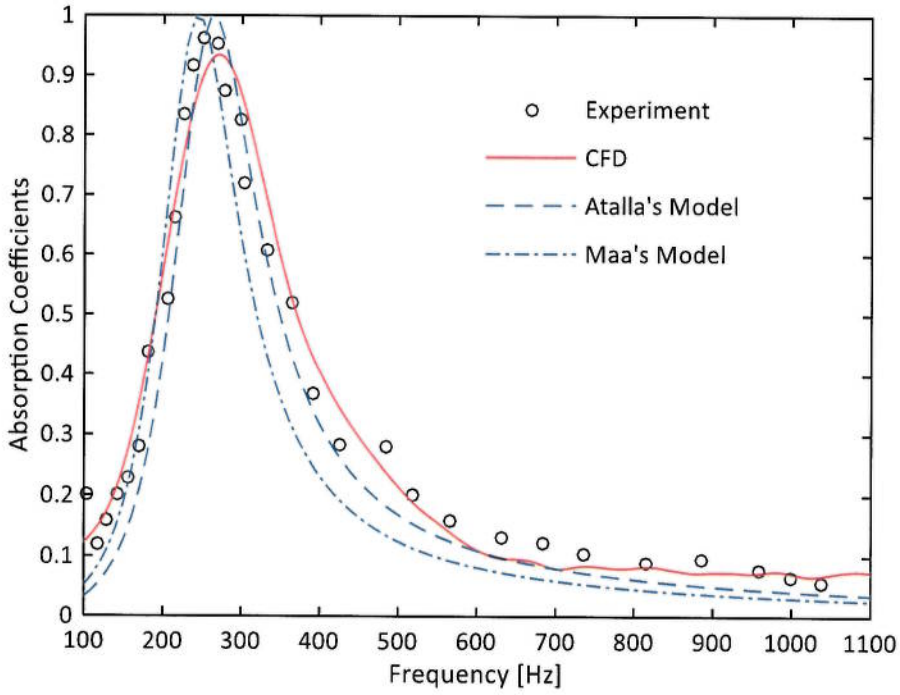

Figure 21 Absorption coefficient curves for plate HA absorber acquired by experiment, CFD and analytical models

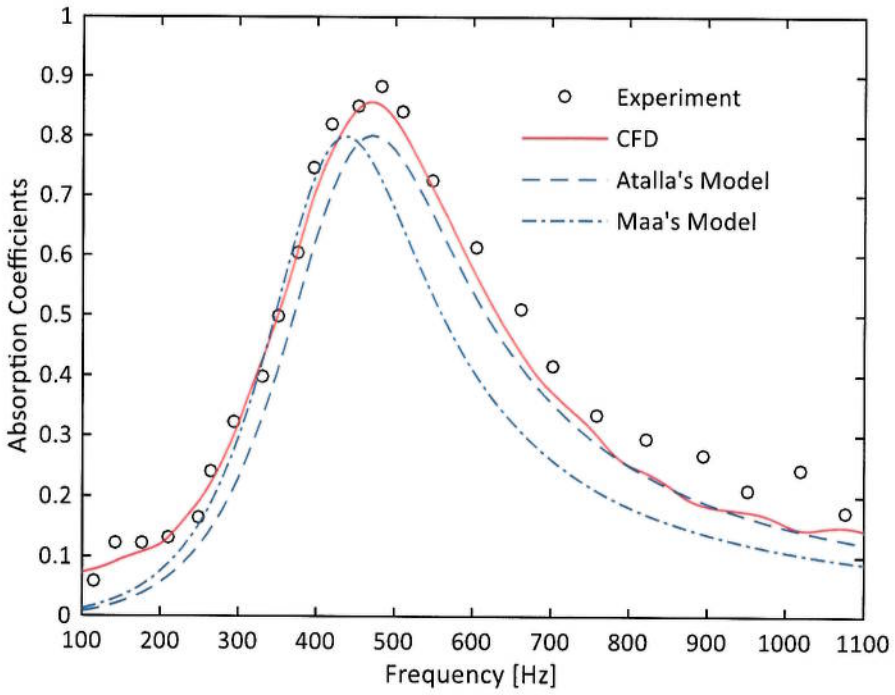

Figure 22 Absorption coefficient curves for plate HB absorber acquired by experiment, CFD and analytical models

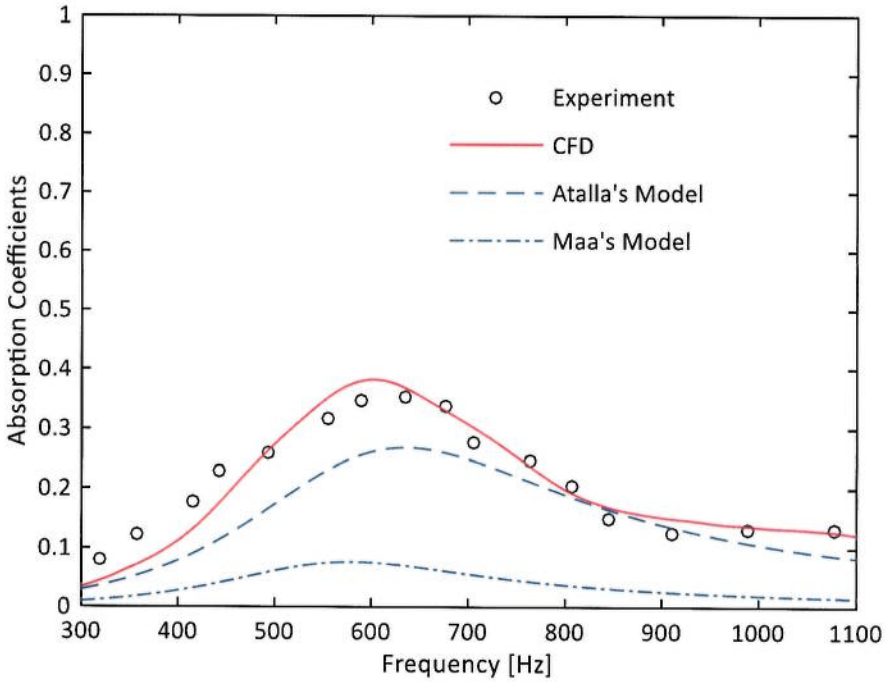

Figure 23 Absorption coefficient curves for plate HC absorber acquired by experiment, CFD and analytical models

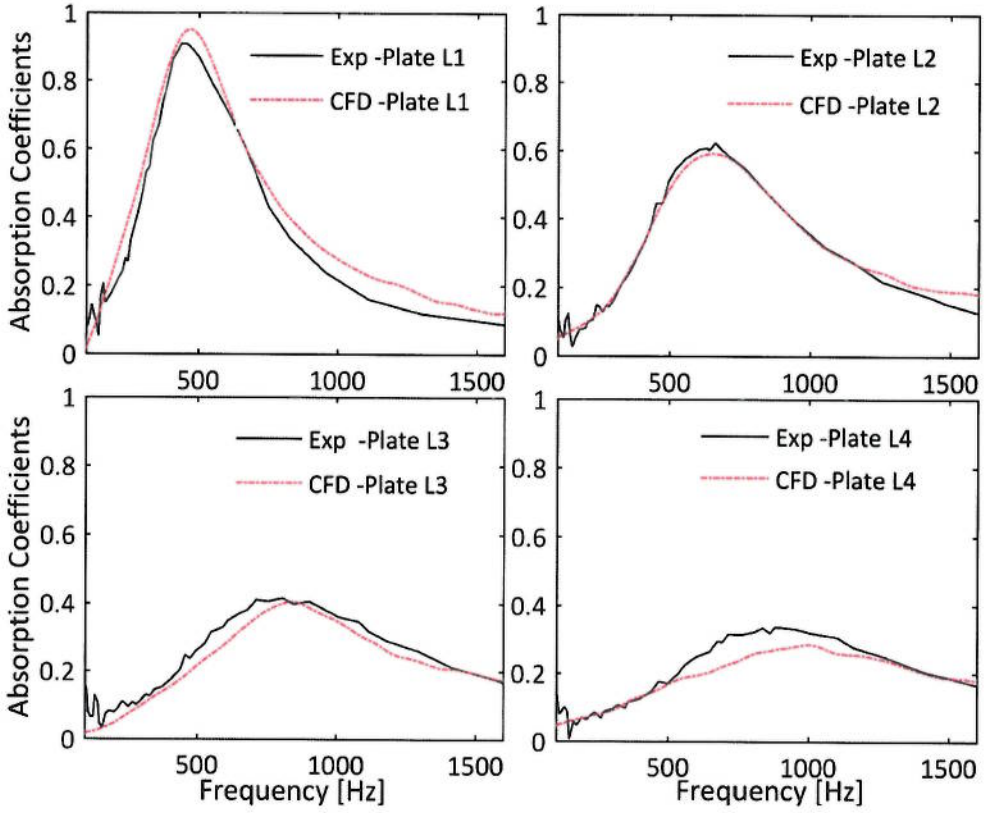

Figure 24 CFD and experimental comparison of absorption coefficients for single layer plate absorbers from Lee's experiment(Lee & Kwon, 2004)

Acoustic attenuation properties of those four perforated panel absorbers from Lee's experiment are reproduced by the proposed CFD method and comparison are displayed in Figure 24. CFD generated absorption coefficient curves for those four panel absorbers all agree closely with experimental curves. Resonance frequencies and absorption bandwidth are reproduced with very high accuracy. As a conclusion of CFD validations against these two experiments, the proposed porous media model is able to very accurately predict the acoustic attenuation effect of perforated pane absorbers in signal normal incidence situations.

4.3.2 Grazing Signal Incidence

Figure 25 shows typical mesh distribution for CFD calculations of signal grazing incidence tests in a flow duct. 2-3 layers of meshes are built in the thickness direction of the perforated plate. At least 20 meshes are built in the radial direction of the impedance tube and at least 20 meshes are guaranteed within one wavelength of the tested signals in the sound propagation direction.

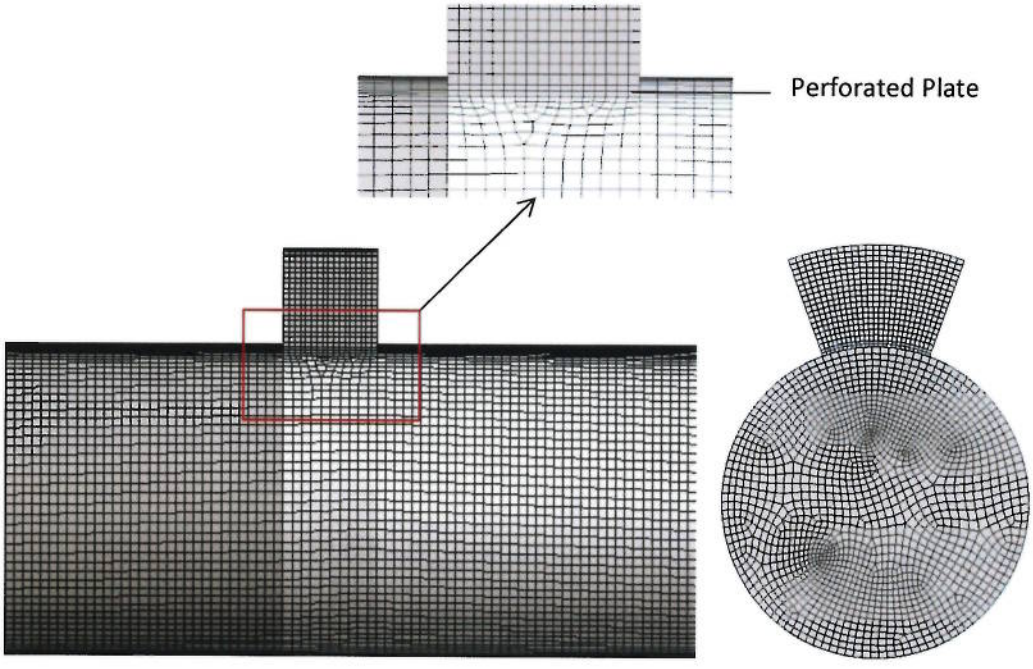

Figure 25 Mesh distribution for CFD calculations of experiment by Houston et al (2015b). (a) Front view (b) Cross sectional view (Houston et al., 2015b)

Figure 26 compares CFD and experimental results of acoustic energy absorption coefficients for H1, H2, H3 panel absorbers in grazing signal incidence conditions in the case of closed resonators. Figure 27 gives the similar comparison between CFD and experiment, however for those "open cavity" cases where a second layer of perforate panel is present. Resonance frequencies and absorption bandwidth for all three panel absorbers in closed cavity and open cavity cases are in close agreement with experimental result. CFD and experimental results also agree that plate H1 with 7.6% porosity displays the highest peak attenuation effect in closed cavity situations. However, it is the plate H3 with a porosity of 13.5% that displays the strongest noise attenuation effect in "open" cavities.

Resonance frequencies are approximately 100Hz higher in "open" cavity situations where the outer liners are present. This may be because that the volume of the cavity is shared by two liners in "open" cavity situations and according to Equation (46), a smaller effective volume of the cavity causes a larger resonance frequency. This shift of resonance frequency to higher frequencies can be found in Lee's experiment as well (Lee & Kwon, 2004) where the addition of extra layers of perforated liner pushes the resonance frequencies to higher value and generates another attenuation peak at lower frequencies. However this lower frequency peak is not found in Figure 27 because the lower resonance frequency is too low to be shown in the graph.

Errors are present such as that CFD tends to overestimate the attenuation effect near resonance frequencies for plate H1. CFD is also more likely to generate slightly narrower attenuation curves for closed cavity absorbers. Despite these errors, CFD provides highly accurate prediction of resonance frequencies and also major shift trends such as frequency shift with rising porosities.

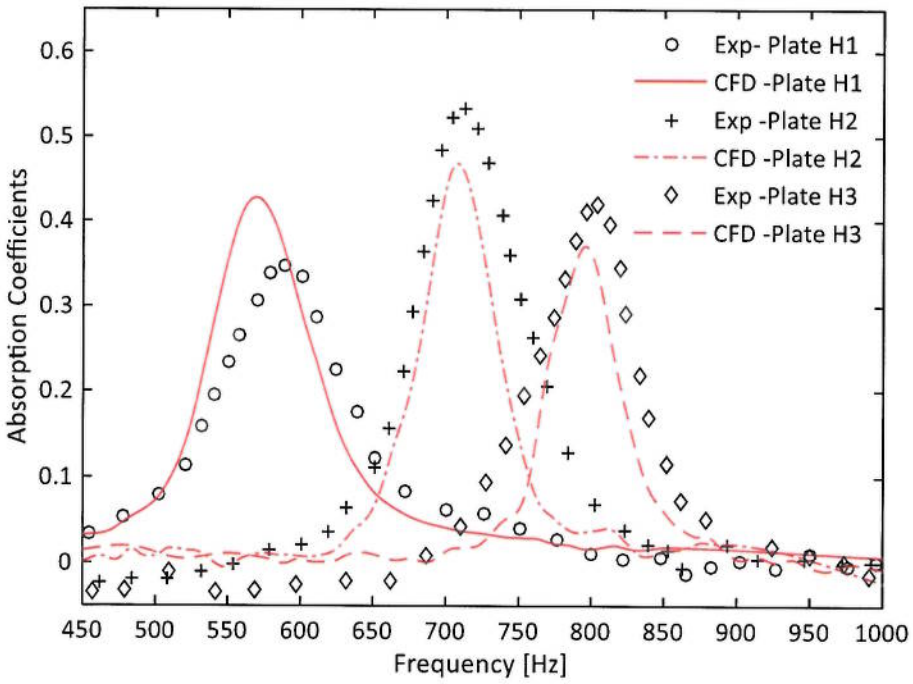

Figure 26 CFD and experimental comparison of absorption coefficients in sound grazing incidence conditions with closed cavity

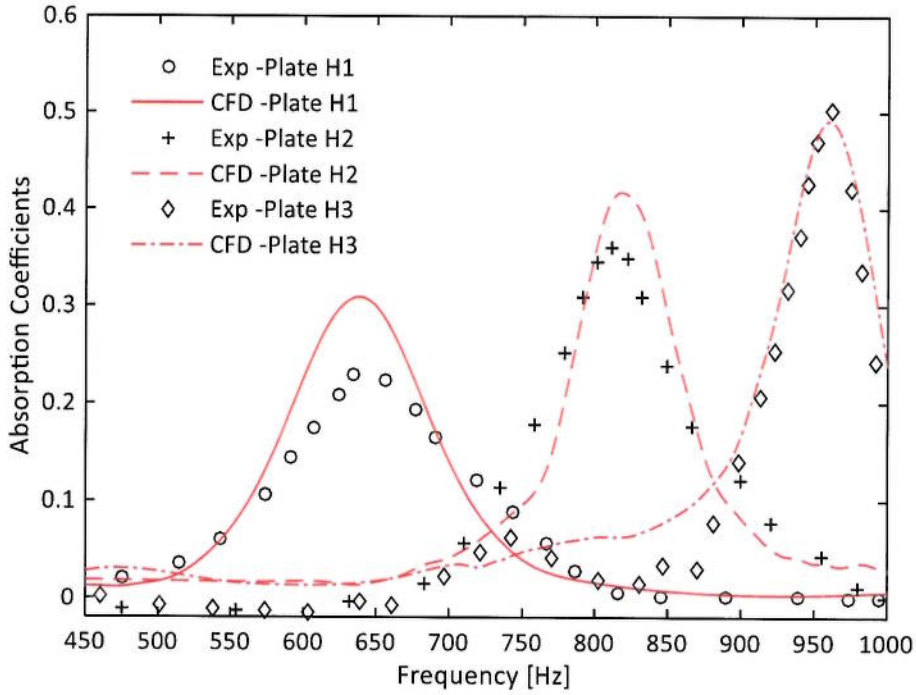

Figure 27 CFD and experimental comparison of absorption coefficients in sound grazing incidence conditions with a second layer of perforated panel

4.3.3 Multi-layer Plates and Array of Plates

Double-layered perforated liners are commonly adopted in gas turbine engines for the purpose of bias flow rate modulation under certain overall pressure drop. CFD calculations are thus carried out for two-layer and three-layer panel absorbers. CFD and experimental results are compared in Figure 28(a) and Figure 28(b) and the agreement between results by these two methods are again very good. It is also shown that the multi-layer setup pushes the first resonance frequency to lower values and the number of absorption effect peaks is the identical with the number of liner layers.

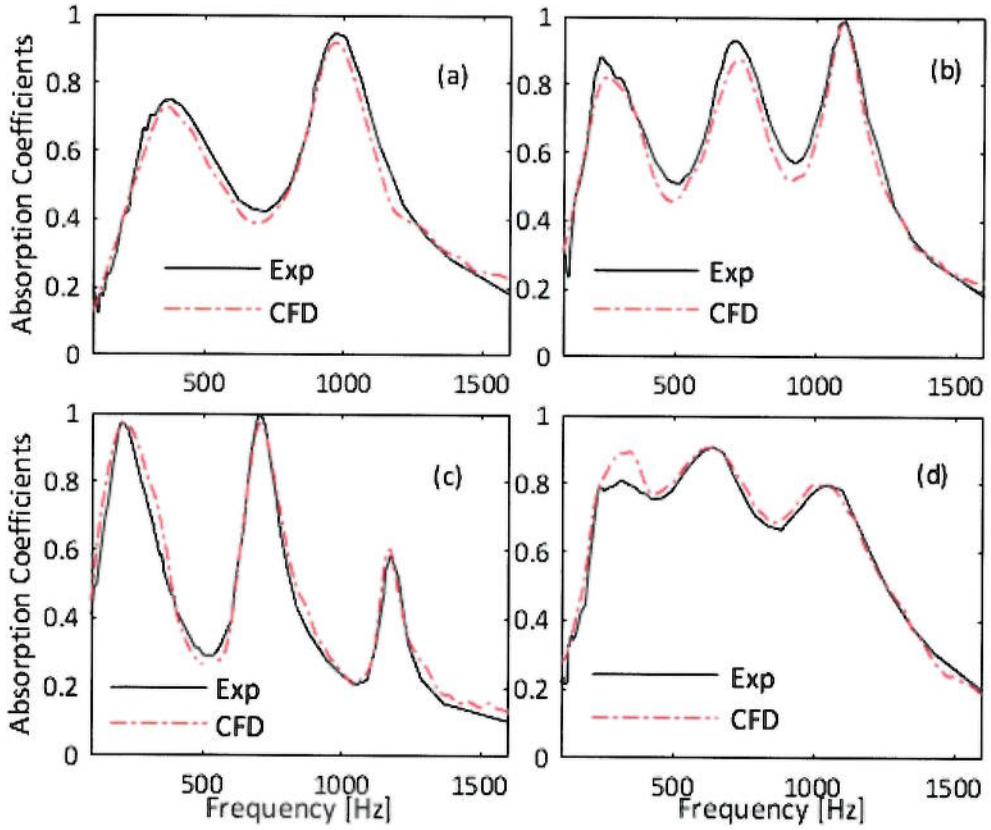

Figure 28 CFD and experimental comparison of absorption coefficients for multi-layer perforated panel absorbers: (a) 2-layer plate L2-L2 (b) 3-layer plate L2-L2-L2 (c) 3-layer absorber of L1-L2-L3 (d) 3-layer absorber of L3-L2-L1 (Lee & Kwon, 2004)

Figure 28(c) displays the absorption coefficient curves of an absorber made of three different plates in the sequence of L1-L2-L3 from upstream to downstream. By contrast, Figure 28(d) displays absorption coefficient curves of the absorber made

of the same three-layer plates but in the reverse order L3-L2-L1. Very different attenuation effects are produced due to the difference in the array of these three plates. Large fluctuation exists in absorption coefficient curves of the former configuration while the latter configuration gives much smoother absorption curves. In addition, the L3-L2-L1 absorber setup yields much better absorption effect than the single layer L3 configuration as shown in Figure 4. CFD generated results are in high level of agreement with experimental results and all these features in experimental results are highlighted in the CFD results.

4.3.4 High Sound Pressure Level

Figure 29 compares the normalized specific acoustic resistance of plate RT335/00 (Melling, 1973) obtained by CFD and experiment. CFD and experimental results agree closely and both methods show that the normalized specific acoustic resistance rise from a very low value (0.03) to approximately 1.5 as incident sound pressure level rises from 118dB to 160dB. The CFD generated absorption coefficient (α) curve indicates that the rising resistance enhances noise attenuation effect but this enhancement effect slows down as incident sound pressure level reaches very high values. Unfortunately, experimental data about absorption coefficients is not available for comparison.

Ingard and Ising (1967) found in their experiment that acoustic specific resistance of an orifice due to high sound pressure level is proportional to particle velocity amplitude in the orifice. This finding was later confirmed by Jing's experiment (Jing & Sun, 2002). Therefore, normalized resistance of an orifice in the presence of high particle velocities is expressed as:

$$r_{\text{orifice}} = \frac{\mathrm{C}U}{c} = \mathrm{CM} \qquad (122)$$

Where M denotes Mach number of the particle velocity amplitude in the neck and normalized specific acoustic resistance of the liner is:

$$r_{\text{liner}} = \frac{\mathrm{C}U}{c\sigma} = \frac{\mathrm{CM}}{\sigma} = \frac{\mathrm{C}\sqrt{2}\mathrm{RMS}(U_{\mathrm{ac}})}{\sigma} \qquad (123)$$

where U_{ac} is orifice acoustical particle velocity and C is a function of

discharge coefficient. According to Melling (1973), C is expressed to be:

$$C = \frac{0.424\rho}{C_d^2}$$

Coefficient C is negatively related to the discharge coefficient of perforated liner. Therefore, non-linear acoustic resistance of plates with larger porosities tends to rise slower with incident sound pressure levels because plates with larger porosities tend to have larger discharge coefficients (Dannenberg et al., 1956; Kolodzie & Van Winkle, 1957).

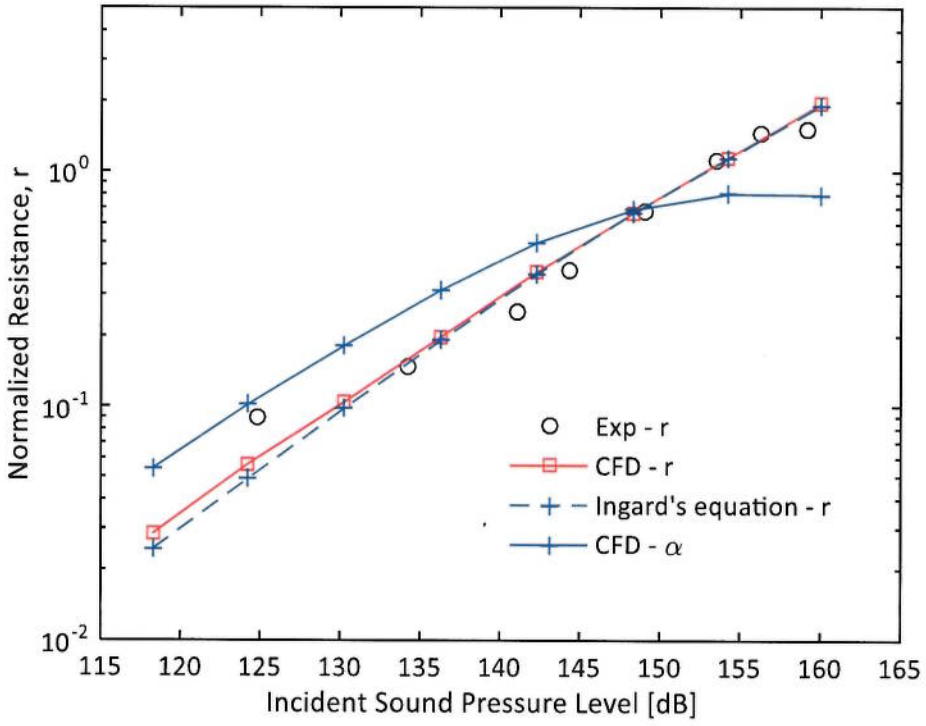

Figure 29 CFD and experimental comparison of normalized specific resistance of Plate RT335/00 in different incident sound pressure levels (Melling, 1973)

The normalized specific acoustic resistance for Melling's plate RT335/00 is calculated by imposing C=1 in Equation (123) using CFD acquired particle velocity and the result is plotted in Figure 29. Agreement between the result from Equation (123) and that from the experiment is very close above SPL 130dB. Equation (123) assessed resistance is however somewhat lower than two-microphone method acquired resistance at low sound pressure levels. This is because Ingard's linear

equation is acquired in high sound pressure levels and it tends to underestimate the contribution of viscous effect in low sound pressure levels.

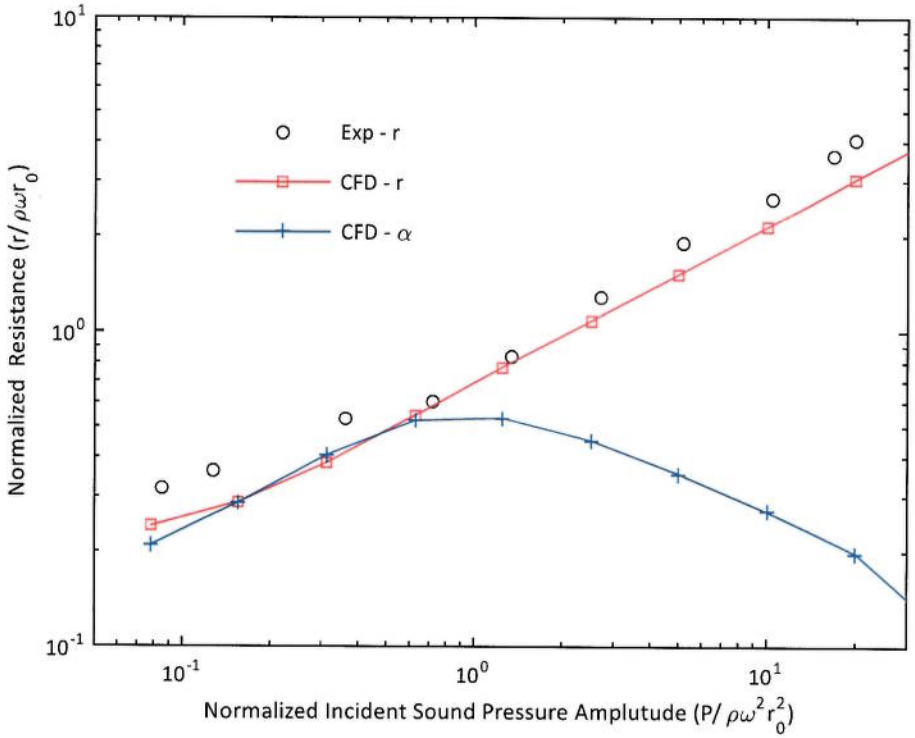

Figure 30 CFD and experiment results for Jing's orifice plate: change of normalized resistance with normalized incident sound pressure amplitude (Jing & Sun, 2002)

Figure 30 compares normalized acoustic resistance acquired by experiment (Jing & Sun, 2002) and corresponding CFD simulations. Incidence sound pressure levels, specific acoustic impedance and orifice velocity are normalized by $\rho\omega^2 r_0^2$, $\rho\omega r_0$, ωr_0 respectively, where ω is the incidence signal angular frequency, r_0 is the radius of the orifice. CFD generated results again agree with the experimental results with quite satisfactory accuracy. CFD method predicts that absorption coefficient rises with increasing sound pressure levels until normalized sound pressure amplitude reaches 1.7 which corresponds to an incident sound pressure level 115dB. After that, the orifice is almost choked and yields very weak attenuation effect at higher sound pressure levels above 140dB ($P/(\rho\omega^2 r_0^2) > 10$). This finding is different from the simulation result of Melling's experiment where absorption coefficient rises up to sound pressure levels of 150dB. This indicates that plates with smaller

porosities and orifices are more easily saturated by high sound pressure levels compared with those plates with larger porosities and orifices.

Figure 31 plots normalized specific resistance acquired by Equation (123) based on CFD acquired particle velocity data against the resistance acquired by CFD based on transfer function method. As can be seen, imposing a higher coefficient C=1.15 in Equation (123) matches CFD generated results more closely than C=1 which is the correct value for Melling's plate. This is because Jing's single orifice plate has a smaller discharge coefficient than Melling's plate RT335/00 according to Equation (124). Proportional coefficient C is larger for liners with smaller porosities and the CFD method successfully yields different proportional coefficients for plates with different porosities.

Figure 32 plots how particle velocity in the perforated plate region changes with incident sound pressure amplitude. First, particle velocities obtained by CFD method agree very closely with those experimental results in a wide range of incident sound pressure amplitudes. Second, both methods indicate that particle velocity in the perforation is proportional to incident sound pressure amplitude within low incident sound pressure amplitudes. However, increase of particle velocity with incidence sound pressure amplitude slows down at high sound pressure levels and the pressure amplitude gradually changes to be in a quadratic relationship with particle velocity. This proves that the proposed CFD method is able to predict the resultant particle velocity due to a wide range of incident pressure amplitude and therefore is able to generate correct acoustic impedance within a wide range of incident sound pressure levels.

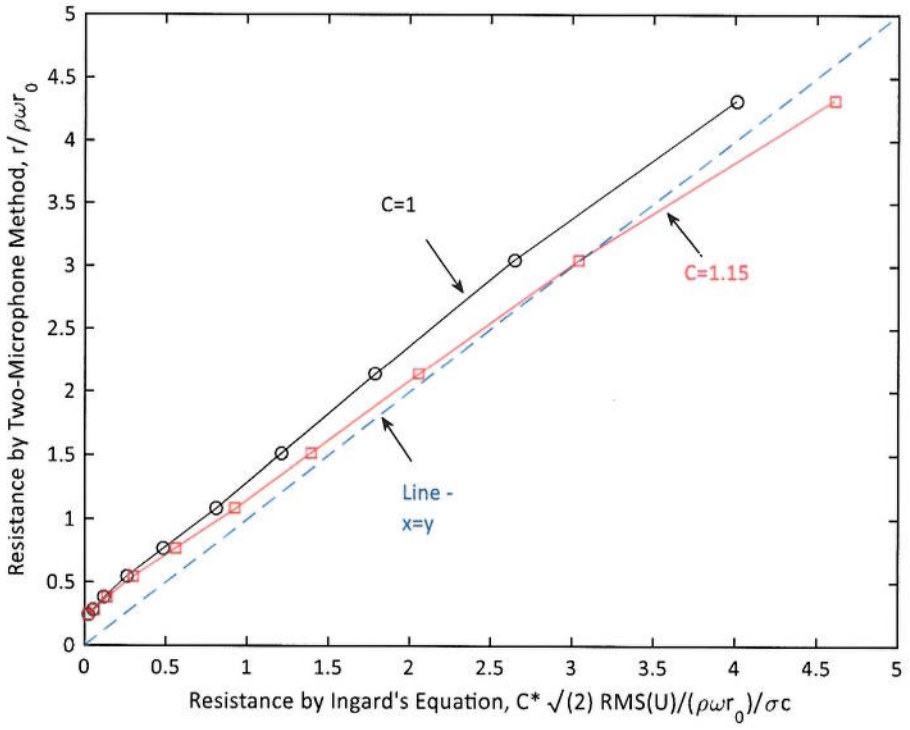

Figure 31 Determination of the proportional coefficient C in Ingard's equation

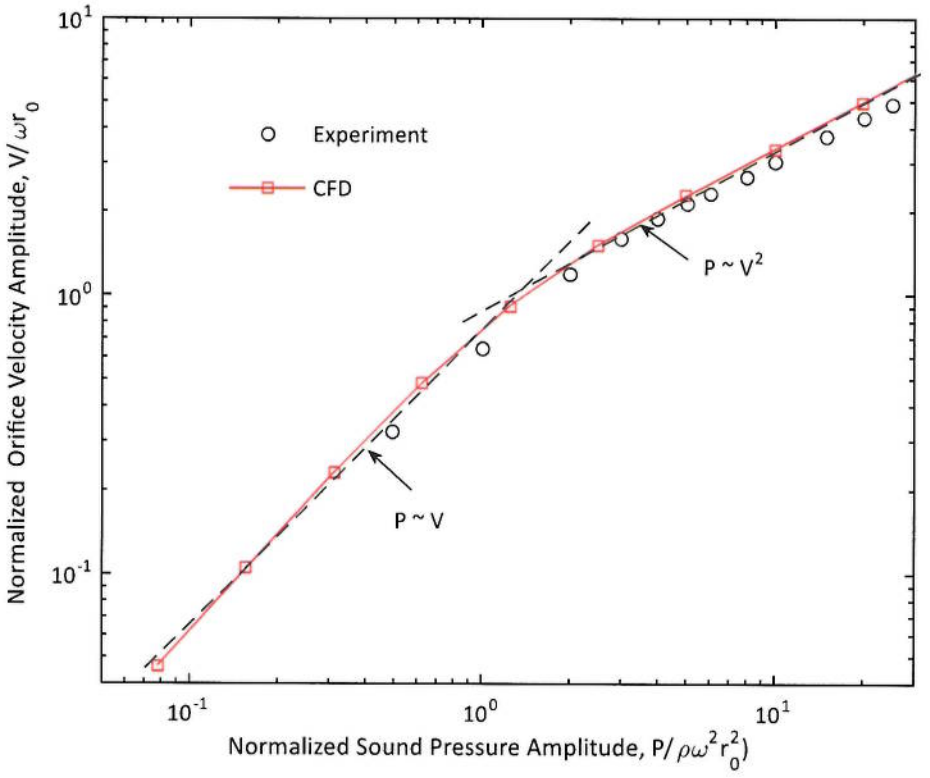

Figure 32 CFD and experimental comparison: change of orifice particle velocity with normalized incident sound pressure amplitude (Jing & Sun, 2002)

4.4 Summary

Five experimental works studying acoustic properties of perforated panel absorbers without the presence of mean flow have been revisited by the proposed CFD method in this chapter. The experimental effects of geometry factors such as the porosity of plate, the number of plate layers and the array of plate layers are successfully reproduced by the proposed CFD method. The experimental effects of the angle and strength of incident sound signals are also reproduced with high accuracy by the proposed CFD method. It is demonstrated that the proposed CFD methodology is able to reproduce acoustic properties of perforated panel absorbers with very high accuracy in zero mean flow conditions.

5. Validation of the Porous Media Model in Predicting the Bias Flow Effect on Acoustic Properties of Perforated Liners

5.1. Review and Objectives

Cool bias flow is injected through perforated gas turbine combustor walls to provide effusion cooling effect (Proscia & Jones, 2007). However, bias flow combustor liners were later found to be able to mitigate large amplitude pressure fluctuations in the combustor. A large number of geometry and flow parameters exert influence on acoustic attenuation effect of bias flow liners. However, research by several authors indicates that the impact of orifice geometry details is negligible in the presence of strong bias flow (Chanaud, 1994; Grace et al., 1998; Ahuji & Gaeta Jr, 2000; Lahiri, 2014; Gaeta & Ahuja, 2016). Acoustic attenuation property of perforated liners is largely determined by only a few geometry and flow factors, namely, bias flow velocity, porosity, zero-flow Helmholtz resonance frequency (Lahiri, 2014). The validity of the proposed CFD method in producing the effect of porosity and the zero-flow Helmholtz resonance frequency has been demonstrated in Chapter 4. This chapter will focus on validating the proposed CFD method in representing the effect of bias flows.

There exist a large number of experimental works studying the effect of bias flow on the acoustic properties of perforated liners. Bellucci and Jing et al. (Hughes & Dowling, 1990; Jing & Sun, 1999; 2000; Bellucci et al., 2004; Lee et al., 2007; Scarpato et al., 2012) tested the effect of bias flow by applying two-microphone method in their modified impedance tubes. Eldredge and Lahiri et al. (Eldredge & Dowling, 2003; Heuwinkel et al., 2007; Zhong & Zhao, 2012; Lahiri, 2014) installed annular perforated liners on the side wall and parallel with grazing flow ducts and the effects of bias flow in grazing signal incidence conditions were investigated. These experiments indicated that acoustic resistance of perforated liners rose with bias flow speed and the injection of appropriate bias flow could enhance acoustic attenuation effects of perforated liner absorbers.

Many Rayleigh conductivity and acoustic impedance models of perforated liners in the presence of bias flow were analytically derived and experimentally regressed. These models are described in details in Chapter 2 (Howe, 1979; Eldredge & Dowling, 2003; Bellucci et al., 2004; Luong et al., 2005). In this chapter, the capability of the proposed CFD method in acquiring the bias flow effect on acoustic properties of perforated liners will be validated against three well-acknowledged experimental works by Jing and Sun (1999), Bellucci et al. (2004) and Eldredge and Dowling (2003). Experiments carried out by University of Hull, Acoustic Research Centre (Houston et al., 2015b) will be re-visited by the proposed CFD method as well.

5.2. Validation Experiments

5.2.1 Jing's and Bellucci's Experiment

Jing and Bellucci et al. (Jing & Sun, 1999; Bellucci et al., 2004) investigated how the presence of bias flow affected acoustic properties of perforated plates. The experimental test rig in Bellucci's work as shown in Figure 33 was a 1.55m long impedance circular tube with a diameter of Ø316mm. Four loudspeakers were installed opposite each other at the end of the impedance tube to generate the acoustic signal. Further upstream of the impedance tube was equipped with an extension space and was filled with sound absorbing porous material so that incoming acoustic waves would not be bounced back to the impedance tube. Four holes were drilled opposite each other on the cavity wall so that the injected bias flow was stagnated in the cavity and flow in orifices was uniform. The impedance tube Jing used was similar with that of Bellucci's and was a 100mm×100mm square tube in which a wide frequency range (100Hz-1700Hz) could be tested. Transient pressure data were collected and processed by the two-microphone transfer function method as described in Section 2.4.1.

Four perforated plates were tested in Bellucci's experiment. Geometric specifications of these plates are listed in Table 4. Plate K was used as reference plate for which reflections coefficients were obtained under 3 different bias flow velocities. Plates Q, T and F were respectively designed to investigate the effects of

orifice size, thickness and porosity. However, orifice size of plate Q and thickness of plate T were well beyond reasonable dimensions and experimental results were absent for plate F. Therefore, only reference plate K is chosen for current CFD validations. Plate K has also been cited by other authors for large eddy simulation validations (Dassé et al., 2008; Mendez & Eldredge, 2009)

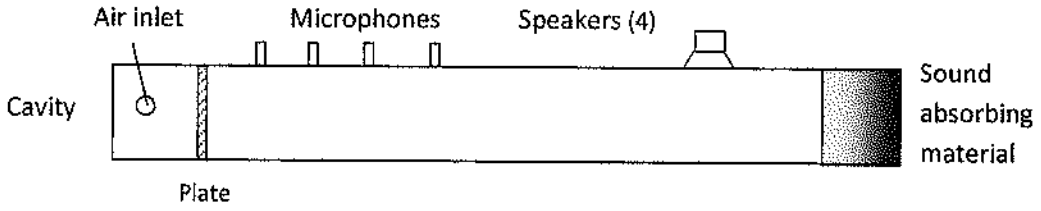

Figure 33 Impedance tube test rig setup in Bellucci's and Jing's experiments

Table 4 Geometric specifications of plates in the experiment by Bellucci et al. (2004)

	Hole-Hole distance	Orifice radius	Porosity	Liner Thickness	Cavity depth
K	35mm	3mm	0.0231	1.5mm	95mm
Q	85mm	6.9mm	0.0207	1.5mm	95mm
T	35mm	3mm	0.0231	43mm	95mm
F	35mm	2mm	0.0103	1.5mm	50mm

Table 5 Geometric specifications of plates in the experiment by Jing and Sun (1999)

	Orifice radius	Hole-Hole distance	Porosity	Thickness
No.1	1.5mm	17mm	0.0254	0.2mm
No.2	1.0mm	13mm	0.0201	0.2mm
No.3	1.5mm	17mm	0.0254	2.0mm

Magnitudes of the reflection coefficients were plotted against signal excitation frequencies by Bellucci et al. (2004). Acoustic energy absorption coefficients were plotted against a resonance parameter Q by Jing and Sun (1999) and the resonance parameter was a geometry dependent feature (Hughes & Dowling, 1990):

$$Q = \frac{\pi}{2}(\mu k l_c)^2 \left(\frac{r_0}{\mu k l_c}\right) \quad (125)$$

where μ is dynamic viscosity of the air, k is the signal wavenumber, l_c is the cavity depth and r_0 is radius of orifices. Geometric specifications of those perforated liners investigated by Jing and Sun (1999) are listed in Table 5.

5.2.2 Experiment by Eldredge and Dowling

Eldredge and Dowling (2003) proposed a one-dimensional homogenous compliance model for perforated liners and experiments were designed and carried out to validate their proposed model. Figure 34 shows the test rig setup in their experiment. Two 800mm long ducts were separated by a 178mm long double layered perforated liners. Both layers of liners were 3mm thick. The outer liner was a Ø152mm annular duct shell with 2% of its area perpendicularly perforated by Ø2.7mm circular holes. The Ø127mm inner liner was perforated by Ø0.75mm circular holes and the overall surface porosity was 4%. Those perforations on the inner liner were titled 45° toward downstream duct.

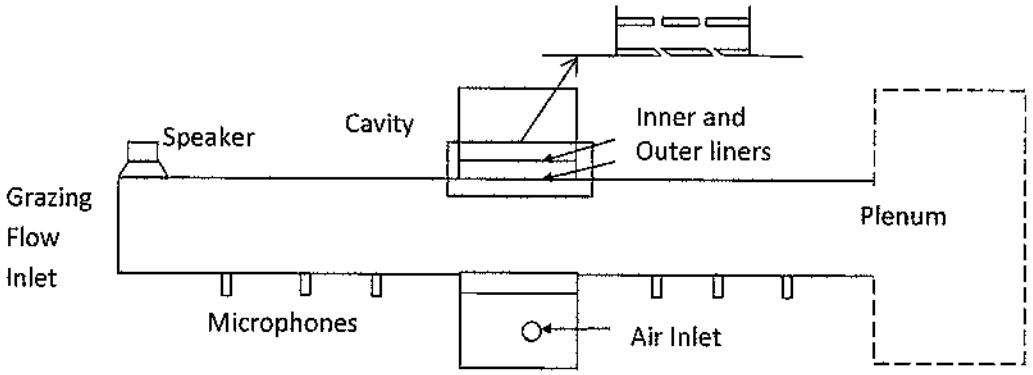

Figure 34 Test rig setup in the experiment by Eldredge and Dowling (2003)

Four loudspeakers were mounted at the end of the upstream flow duct and the sine wave signals between 100Hz and 700Hz were excited. The radial gap in between the two liners formed an inner air cavity. Bias flow was compressed into the cavity and the mean flow was finally emptied to a large plenum at the exit of downstream duct as shown in Figure 34. This plenum will be included in the calculation domain of CFD simulations. Transient pressure data were collected and processed by the two-microphone transfer function method as described in Section 2.4.2. The double layered liners parallel with mean flow ducts and the inclined peroration angle are to

a large degree comparable to those situations in real gas turbines. It is therefore very meaningful to validate the proposed CFD method against this experiment before the CFD method is applied to simulate perforated liners in real gas turbine engines.

5.2.3 Experiment by Houston and Wang

University of Hull, Acoustic Research Centre tested the acoustic attenuation properties of three double layered perforated liners in various bias flow conditions (Houston et al., 2015b). Geometric details about the two layers of liners and the experimental test rig can be found in Section 4.2.1. Similar with the experiment by Eldredge and Dowling (2003), perforated plates in this experiment were installed parallel with the flow duct. However, while the liner in Eldredge's experiments were an full annular duct shell, liners in this experiment were much smaller and those inner liners were only able to occupy a circumferential angle of $41.5°$ on a $\emptyset 165\text{mm}$ flow duct as shown in Figure 15 and Figure 16. Bias flow was compressed through a $\emptyset 52\text{mm}$ pipe an entered a 435mL box. The flow was then further driven into a steel cavity (201mL) before it finally arrived at the grazing flow duct. Most of the overall pressure drop was consumed across outer liners due to their low perforation rates. Volumetric air flow rate was collected so that bias flow speed was able to be calculated. Both ends of the flow ducts were anechoic by filling in sound absorbing structures. Acoustic signal applied was a 118dB random signal within 300Hz-1000Hz. Transient pressure data were collected and processed by the two-microphone transfer function method as described in Section 2.4.2.

5.3. Results and Discussion

5.3.1 Bellucci's Experiment

The mesh resolution applied in the CFD simulations for experiments by Bellucci and Jing et al.(Jing & Sun, 1999; Bellucci et al., 2004) follows same criteria with the mesh resolution shown in **Figure 20**. Reference plate K in Bellucci's experiment is re-tested by the proposed CFD method. Figure 35 compares CFD, Bellucci's model and experiment acquired magnitudes of reflection coefficients for plate K absorber in three bias flow conditions. Both CFD and experimental data predict that the

magnitudes of reflection coefficients decline with increasing bias flow speed from 0m/s to 2m/s and 5m/s. The frequency of the lowest reflection coefficient shifts to higher values as bias flow velocity increases. Optimum absorption effect is achieved in the 5m/s bias flow condition according to Equation (45).

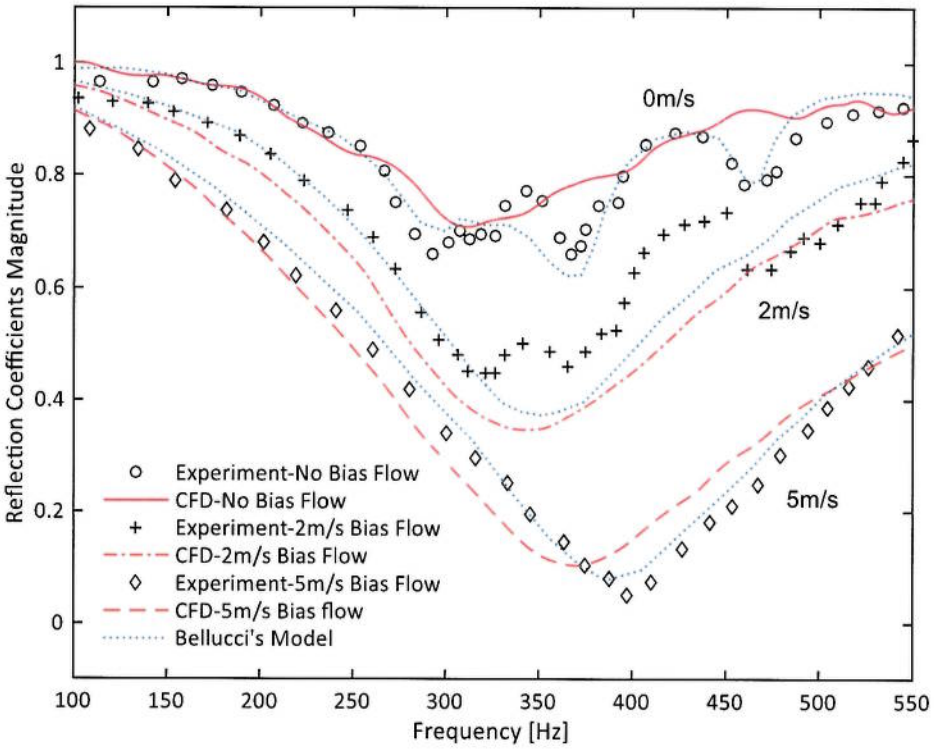

Figure 35 CFD and experimental comparison of reflection coefficients magnitude for reference plate K in Bellucci's work (Bellucci et al., 2004)

Table 6 Resonance Frequency and Absorption Bandwidth of Plate K[1]

Bias Flow	f_{reson}			$f_{1/2}$			Q factors		
	Expe	Model	CFD	Exp	Model	CFD	Exp	Model	CFD
0m/s	295Hz	362Hz	304Hz	160Hz	160Hz	178Hz	1.84	2.25	1.70
2m/s	326Hz	350Hz	343Hz	245Hz	235Hz	270Hz	1.33	1.49	1.27
5m/s	396Hz	382Hz	373Hz	280Hz	270Hz	295Hz	1.41	1.42	1.26

Absorption coefficients calculated by Equation (45) and Q factors defined in Equation (47) are listed in Table 6. It shows that CFD method generates slightly

[1]Absorption bandwidth for the 5m/s bias flow case is taken across frequencies those are with 75% of the maximum absorption effect because experimental data at frequencies with 50% of the maximum absorption effect is not available.

higher resonance frequencies in zero flow and 2m/s bias flow conditions than experiments do, yet it generates slightly lower resonance frequency and higher reflection curve in 5m/s bias flow case than experiments do. This may be due to that the iregular data points in the experimental curves for zero flow and 2m/s bias flow conditions makes it difficult to pinpoint the lowest reflection coefficient. CFD generated absorption coefficient curves are slightly lower and with somewhat smaller Q factors compared with those curves acquired by experiment and Belluci's model, and this is especially true for the 2m/s bias flow condition. This suggestes that CFD method may tend to overestimate attenuation effect in the medium bias flow velocities, which is 2m/s bias flow in this experiment.

Besides limited errors, CFD yields more consistent shift trend of resonance frequencies with bias flow speed than experiments do. In general, CFD shows excellent ability in reproducing the attenuation effect enhancement by the introduction of bias flows despite limited errors in the absorption bandwidth.

5.3.2 Experiment of Jing and Sun's

Jing and Sun (1999) experimentally tested acoustic properties of three perforated liners under more bias flow conditions. CFD and experimental absorption coefficient curves are compared in Figure 36 for an absorber made of plate No.1 and a 60mm deep cavity under zero bias flow and 5m/s bias flow conditions. High degree of agreement between CFD, experiment and Howe's model (Howe, 1979) is achieved in these two bias flow conditions. All three methods suggest that the presence of 5m/s bias flow is able to yield much higher absorption magnitude and broader absorption bandwidth.

CFD and experimental results of the normalized specific acoustic impedance for this panel absorber is compared in Figure 37. The reactance curve is flatter and zero reactance occurs at higher frequencies when 5m/s bias flow is present. According to Equation (45), frequency with a zero reactance corresponds to the optimum absorption effect and a lower reactance leads to a larger absorption coefficient. Therefore, the flatter reactance curve and the higher frequency with zero reactance in 5m/s bias flow condition correspond well to Figure 36 where the absorption

curve is broader and resonance frequency is higher in the presence of 5m/s bias flow. In addition, normalized resistance increases from 0.2-0.3 in zero flow condition to 1-1.2 and this rise in resistance in the 5m/s bias flow condition explains why noticeably stronger absorption effect is achieved in 5m/s bias flow. On the other hand, there is very little change in the normalized resistance across a wide frequency range when bias flow is present.

Figure 38 displays the absorption effect of liner No. 2 under several bias flow conditions. CFD results indicate that the noise attenuation effect is enhanced quickly with the introduction of bias flows. The absorption coefficient rises from approximately 50% in zero flow condition to 95% when bias flow Mach number is approximately 0.01. Nearly 100% absorption is achieved at Mach number 0.012. After this point, the absorption coefficient gradually declines but remains above 60% up to $M_b = 0.04$. The experimental curve follows the same trend with CFD curves: attenuation effect increases from 60% in zero flow condition to 100% at Mach number 0.012, and absorption effect declines at even higher bias flow Mach numbers.

However, a difference between CFD and experiment is present: CFD method indicates somewhat better attenuation effects than the experiment does in low bias flow conditions. Similar error is found in 2m/s bias flow validation case for Bellucci's experiment as shown in Figure 35. On the other hand, Howe's theory also yields somewhat higher attenuation effect at low bias flow situations than that of experiment. Therefore, admitting the overestimation of attenuation effect within low bias flow conditions by CFD, this error could potentially be exaggerated due to errors in the experimental curve which shows an abrupt change near Mach number 0.005.

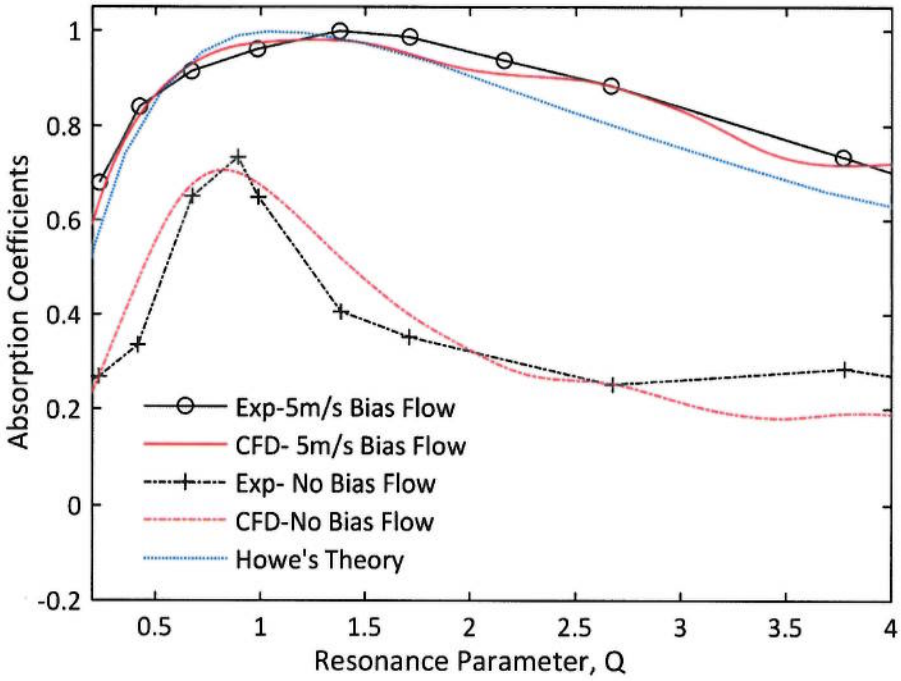

Figure 36 CFD and experimental comparison of absorption coefficients for perforated liner No.1 in 5m/s bias flow and zero bias flow conditions ($l_c = 60\text{mm}$) (Jing & Sun, 1999)

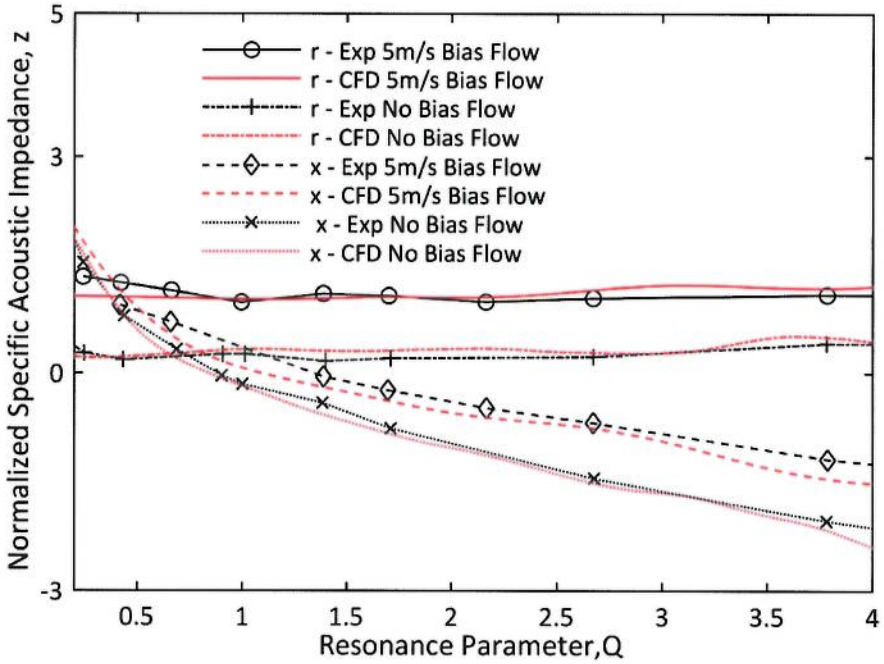

Figure 37 CFD and experimental comparison of normalized specific acoustic impedance for perforated liner No.1 in 5m/s bias flow and zero bias flow conditions ($l_c = 60\text{mm}$) (Jing & Sun, 1999)

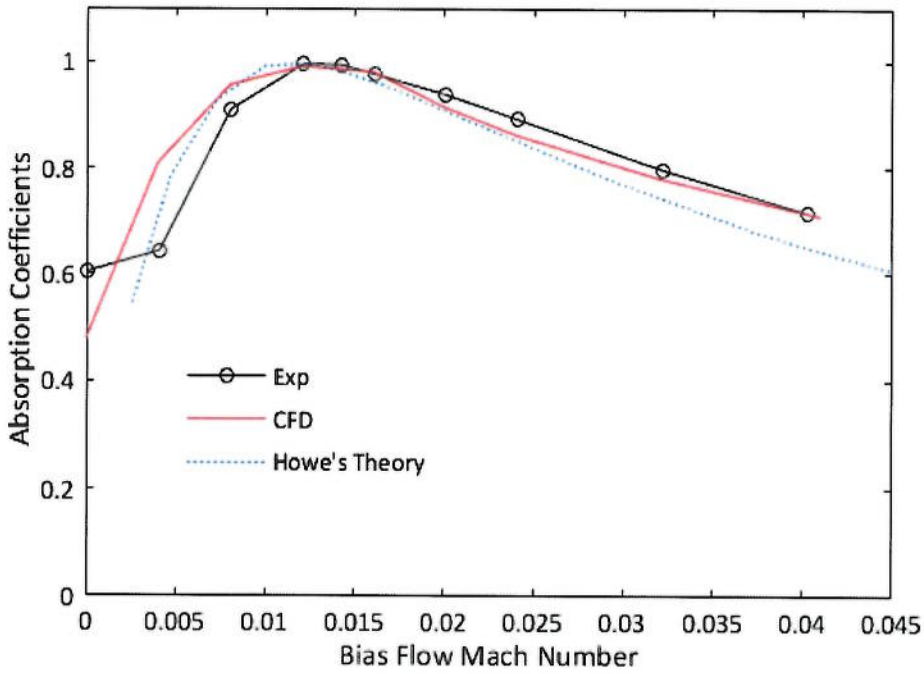

Figure 38 CFD and experimental comparison of absorption coefficients for perforated liner No.2 in different bias flow situations (Q = 1, $l_c = 60\text{mm}$) (Jing & Sun, 1999)

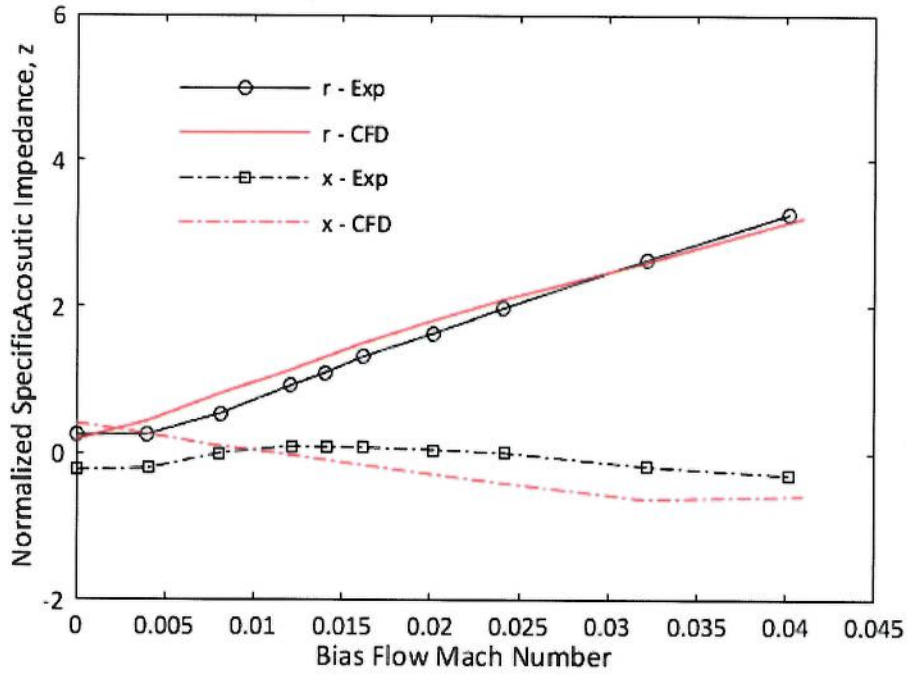

Figure 39 CFD and experimental comparison of normalized specific acoustic impedance for perforated liner No.2 in different bias flow situations (Q = 1,$l_c = 60\text{mm}$) (Jing & Sun, 1999)

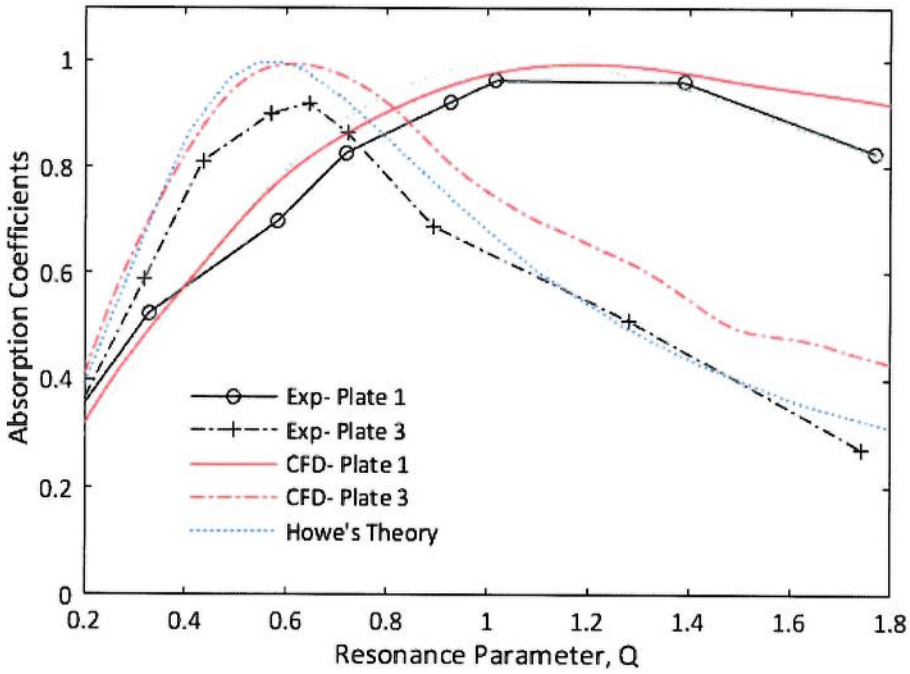

Figure 40 CFD and experimental comparison of absorption coefficients for perforated liners No.1 and No.3 with different thickness under 5.4m/s bias flow ($l_c = 60\text{mm}$) (Jing & Sun, 1999)

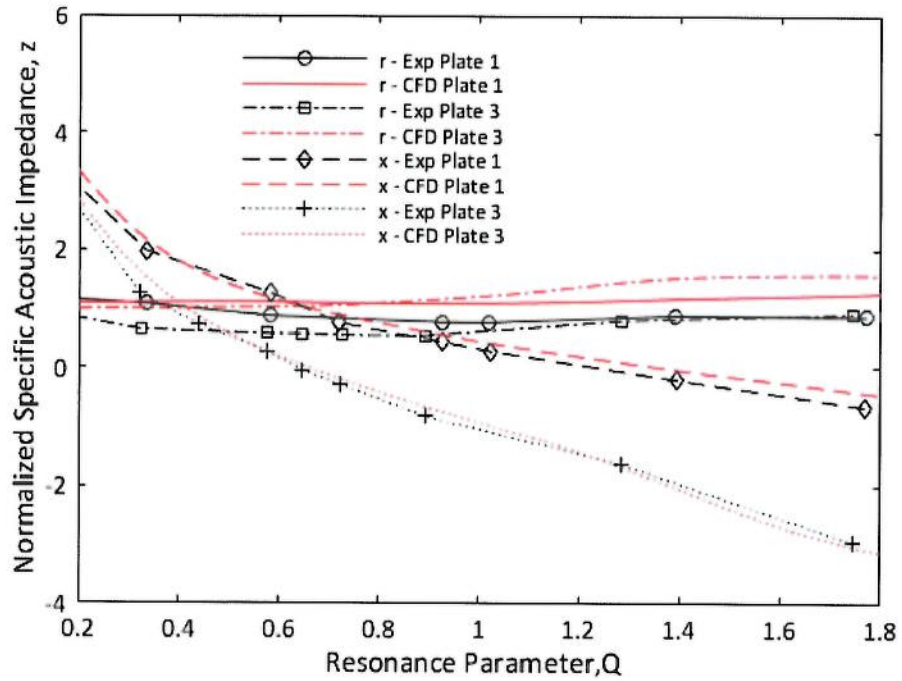

Figure 41 CFD and experimental comparison of normalized specific acoustic impedance for perforated liners No.1 and No.3 with different thickness under 5.4m/s bias flow condition($l_c = 60\text{mm}$) (Jing & Sun, 1999)

Figure 39 shows that both experiment and CFD indicate a linear acoustic resistance with bias flow velocities. The linear relationship between acoustic resistance and bias flow velocity is found by other researchers as well (Sivian, 1935; Bauer, 1977; Cummings & Eversman, 1983).

$$r = \frac{C_b U}{\sigma c} = \frac{C_b M}{\sigma} \qquad (126)$$

The proportional constanct C_b is a constant between 1 and 1.5, whose value depends on the contraction coefficients of the bias flow jet (Cummings & Eversman, 1983). The constant is approximately 1.5 for the current liner setup according to the CFD and experimental results shown in Figure 39. It is interesting to see the high similarity between Equation (126) for mean bias flow situations and Equation (123) for high sound incidence levels situations. The sole difference is that the proportional constant is higher in the presence of mean bias flow. According to (124), this implies that the discharge coefficeint of perforate liner No.2 is reduced by the presence of bias flow which is in turn a result of the rapid growing inertial flow resistance according to Equation (104).

To summarize for No.2 liner validation case: CFD is capable of giving accurate prediction about the optimum absorption coefficients of a perforated liner and the corresponding optimum bias flow velocity. It is also able to reproduce the experimental trend about how attenuation effect varies with varying bias flow velocities. At the same time, CFD tends to exaggerate attenuation enhancement effect by bias flow in the low bias flow region.

Figure 40 illustrates absorption coefficient curves acquired by CFD and experiment for perforated liners No.1 and No.3. The two liners No.1 and No.3 are with identical orifice geometries but different liner thickness. Both CFD and experimental curves indicate that the thicker liner No.3 tends to peak absorption frequency to lower values. In addition, the absorption coefficient curve for the thinner liner No.1 remains at high values at high frequencies whereas the absorption curve for the thicker liner No.3 shows more rapid decline at high frequencies. This difference is explainable by looking at the acoustic reactance curves displayed in Figure 41. Acoustic reactance curve of liner No.3 is steeper and zero reactance occurs at a

lower frequency than that of liner No.1. According to Equation (45), a steeper reactance curve and larger magnitudes of reactance will give rise to a narrower absorption coefficient curve.

The absorption curves for liner No.3 agree very well between CFD, experiment and Howe's theory in terms of the general trend. However, errors exist as well. For example, magnitude of CFD generated absorption coefficients are about 0.05 higher than those acquired by experiment within high frequencies. Howe's theory generated absorption coefficients are about 0.05 larger than experimental results as well in low frequency ranges.

To summarize validation results for Jing's experiment, both CFD and experiments confirm that the introduction of bias flow enhances the noise attenuation effect of perforated liners. CFD is able to accurately predict the bias flow conditions with optimum absorption effects. The effect of plate thickness on liner absorption property is represented by CFD with fairly good accuracy as well. Lastly, while CFD is able to predict absorption effect of perforated liners with good accuracy within medium to high bias flow conditions, it tends to give somewhat higher absorption coefficients than experiments do in low bias flow regions.

5.3.3 Eldredge & Dowling's Experiment

Figure 25 shows the mesh distribution for CFD calculations of the double layered liner absorber in the experiment by Eldredge and Dowling (2003). 2-3 layers of meshes are built in the thickness direction of both perforated plates. At least 20 meshes are built in the radial direction of the impedance tube and at least 20 meshes are guaranteed within one wavelength of the tested signals in the sound propagation direction. The mesh resolution is refined in the cavity between two perorated plates so that flow and acoustic field can be better represented in this narrow yet significant location.

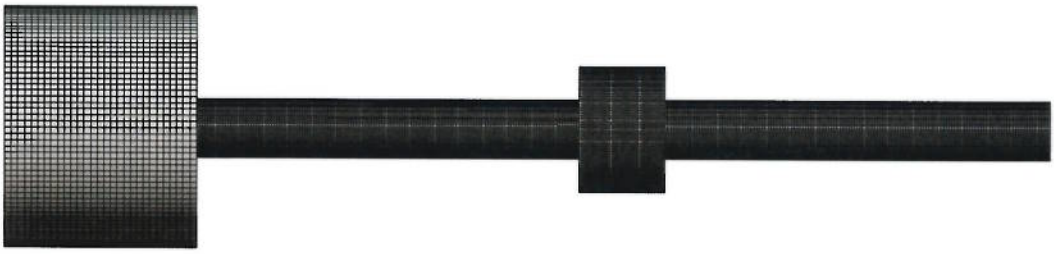

(a)

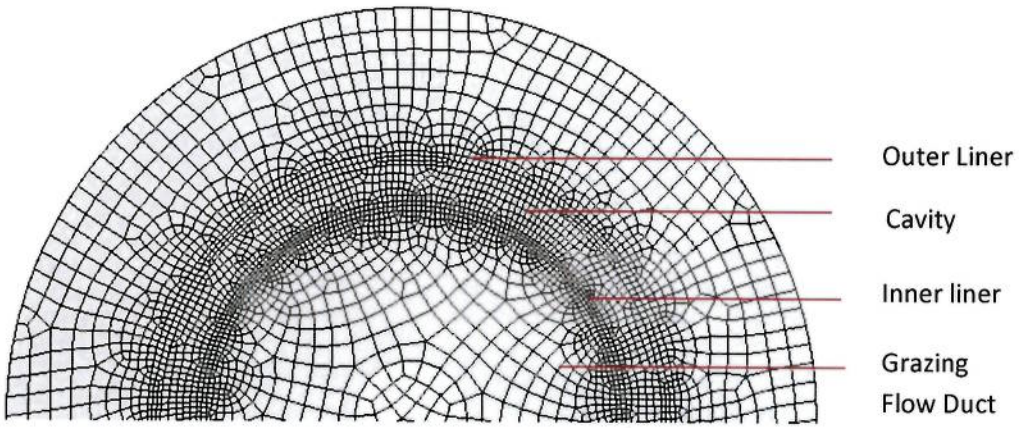

(b)

Figure 42 Mesh distribution for CFD calculations of experiment by Houston et al (2015b). (a) Front view (b) Half of the cross sectional view of the liner test section

Absorption coefficients obtained by CFD, experiment and Eldredge's model are plotted against the wave number in Figure 43 and Figure 44. $\mathrm{M_{in}}$ stand for the bias flow Mach number through the inner liner, k is the signal wave number and L is the length of the liner. Those peak and bottom absorption coefficients and corresponding frequencies generated by CFD method are in very close agreement with experimental and model results. The successful capturing of absorption effect fluctuations with frequencies proves that CFD method is able to represent acoustical reflections from the downstream plenum. Compare Figure 43 and Figure 44, all the three methods indicate that an increase of bias flow Mach number from 0.023 to 0.041 reduces peak absorption coefficients by approximately 10% while the minimum magnitude of absorption coefficients hardly changes.

Besides the overall good agreement, discrepancies exist between absorption coefficient curves acquired by different methods, especially at very high frequencies when $k{\cdot}L>1.7$. Eldredge and Dowling (2003) suggested that this error

may be a result of the high sensitivity of high frequency signals to the interference between left and right travelling waves in the liner section.

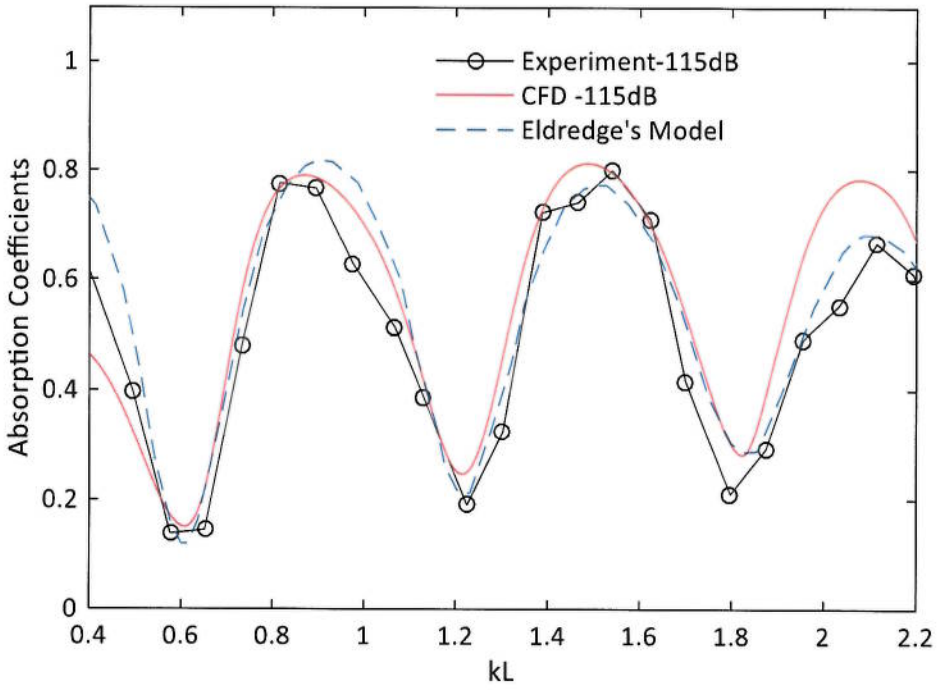

Figure 43 CFD and experimental comparison of absorption coefficients at $M_{in} = 0.023$ and zero grazing flow conditions (Eldredge & Dowling, 2003)

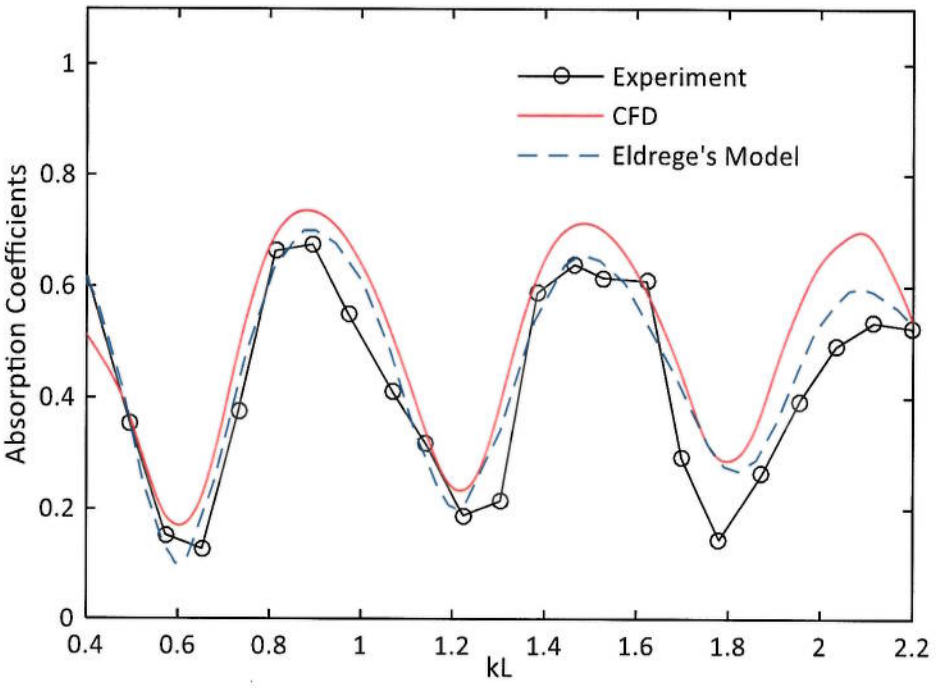

Figure 44 CFD and experimental comparison of absorption coefficients at $M_{in} = 0.041$ and zero grazing flow conditions (Eldredge & Dowling, 2003)

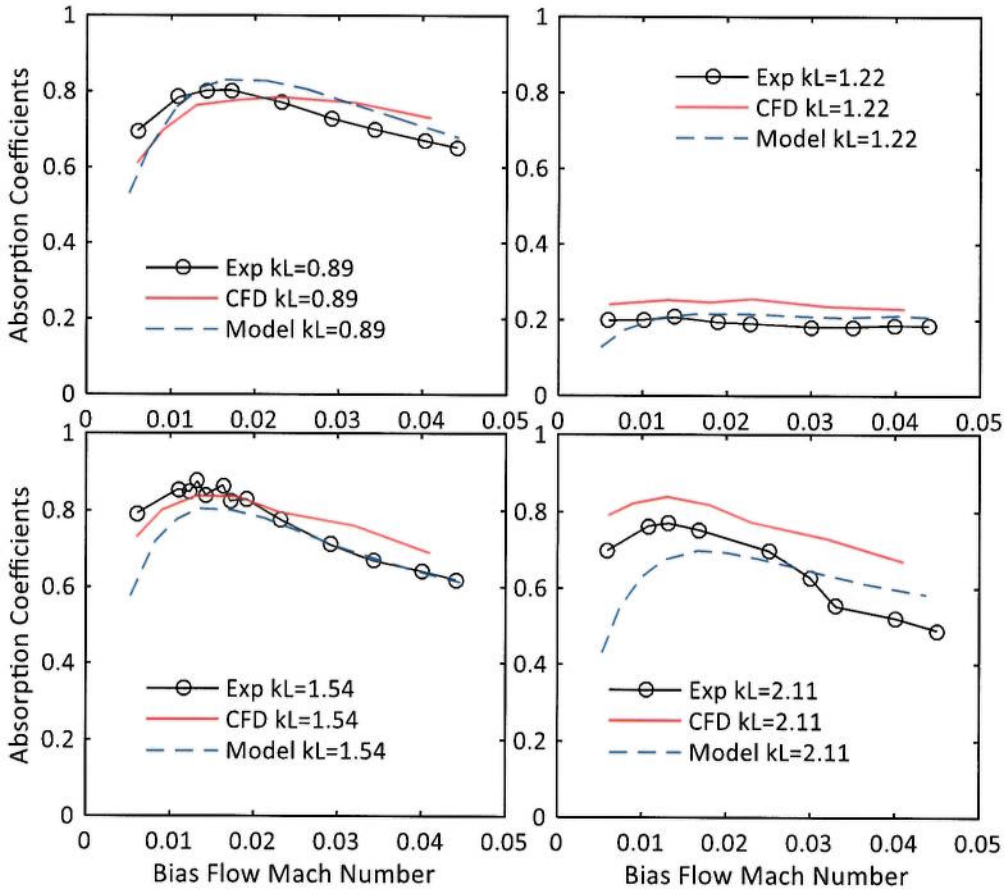

Figure 45 CFD and experimental comparison of absorption coefficients variation with bias flow speed in zero grazing flow conditions (Eldredge & Dowling, 2003)

Figure 45 demonstrates noise absorption effect variation with bias flow Mach numbers. All three methods suggest that the optimum absorption effect takes place between $0.01 < \mathrm{M_{in}} < 0.02$, and all three methods indicate that further increase of bias flow speed above the optimum speed reduces the peak absorption coefficients, yet the minimum absorption effect at frequencies $kL = 1.22$ is hardly changed by the bias flow speed. This finding has been suggested by the Jing and Sun' experiment (1999): Figure 38 has shown that there exist an optimum absorption bias low Mach number for a perforated liner, weaker or stronger bias flows than the optimum speed reduce the optimum absorption effect. According to Eldredge and Dowling (2003), the optimum attenuation effect of a perforated liner is achieved in the following bias flow condition:

$$\left(\frac{M_b}{\sigma}\right)_{opt} = \frac{s_l/s_d}{2\sqrt{2}} \quad (127)$$

where s_l is the area of the liner surface and s_d is the cross section area of the flow duct. It is clearly indicated in this equation that the optimum bias flow speed at which a perforated liner achieves optimum absorption effect depends on the porosity of the liner and its relative size to the flow duct as well.

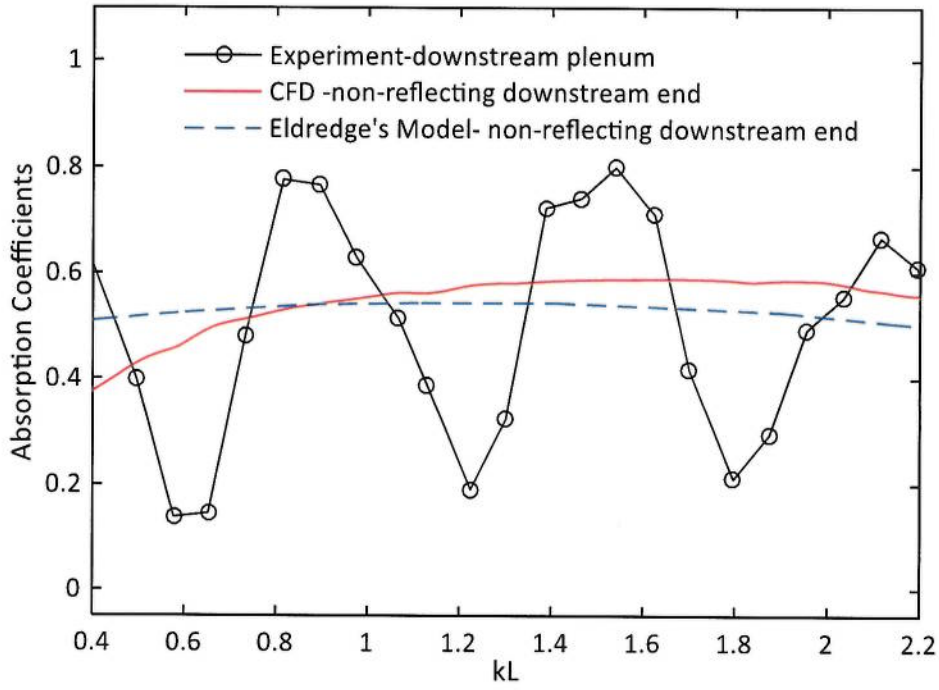

Figure 46 CFD & Experiment Absorption Effect Comparison with Non-Reflecting Downstream End (bias flow Mach number in inner liner=0.023, zero grazing flow, L=0.178) (Eldredge & Dowling, 2003)

Eldredge and Dolwing (2003) also calculated the absorption effect of this two-layered liner assuming the downstream duct is infinitely long. The infinitely long downstream duct is equivalent to an acoustically non-reflecting boundary in CFD simulations. Figure 46 compares the absorption coefficient curves obtained by CFD method in non-reflecting boundary conditions and that by the model (Eldredge & Dowling, 2003). The CFD generated absorption coefficient curve generally matches very closely with that by the model of Eldredge's. In addition, there is a vast difference between the absorption coefficient curves under different downstream acoustic boundary conditions and this proves the significance of acoustic property

of boundaries in determining overall absorption effects of a liner absorber. The success of CFD method in yielding acoustic attenuation effect in both boundary conditions not only validates the capability of the CFD method in resolving acoustic property of perforated liners itself, it also highlights the unique advantage of CFD method in accounting for surrounding acoustical boundary conditions at little extra cost. Limited errors do exist. CFD generated absorption coefficients are slightly larger than the model results at higher frequencies and somewhat lower at very low frequencies. Corresponding errors in the very low and high frequency ranges occurs as well in the results as shown in Figure 43 and Figure 44.

5.3.4 Experiment by Houston and Wang

The three liner absorbers tested by University of Hull, Acoustic Research Centre (Houston et al., 2015b) are three distributed Helmholtz resonators fixed parallel with the main flow duct. Details of these absorbers have been given in Section 4.2.1 and Section 5.3.2. Absorption coefficient curves obtained by experiment and CFD are compared in Figure 47, Figure 48 and Figure 49. As can be seen, CFD and experimental methods generate very similar resonance frequencies for all three liners in zero bias flow conditions.

The injection of 5m/s bias flow is shown to be able to significantly enhance the attenuation effect of perforated liner absorbers in previous experiments as shown in Figure 35 and Figure 38 (Jing & Sun, 1999; Bellucci et al., 2004). However, Figure 47, Figure 48 and Figure 49 show that a similar speed of 5.6m/s bias flow reduces peak attenuation coefficients of all these three perforated liners. Introducing bias flow at even higher speed (10m/s) further suppresses absorption coefficient to a very low level below 0.2. This is because, according to Equation (127), the very small values of s_l/s_d represented by these three liners will result in optimum bias flow Mach numbers at around 0.006-0.01. Therefore, the attenuation effect of these liners is saturated by a bias flow of 5m/s -10m/s (M=0.0165-0.033). This very different bias flow effects across different experiments confirms that similar bias flow speeds can result in different impact on the acoustic absorption properties of different perforated liners.

Lastly, Figure 47, Figure 48 and Figure 49 suggest that the peak absorption effect occurs at lower frequencies in the presence of bias flow than those in zero flow conditions. This can be explained by that: The cavity volume is shared by the acoustic resonance effect of two liners in zero mean flow conditions. However, the presence of bias flow suppresses the resonance effect due to resultant strong inertial resistance in the orifice and the inertial resistance is much stronger for the outer liners due to their much smaller porosities compared with the inner liner. As a result, the part of cavity volume that originally participates in the resonance of the outer liner is utilized by the inner layer in the presence of the bias flow.

Despite the close agreement between CFD and experimental prediction, noticeable errors exist in the magnitude and bandwidth of absorption coefficients curves. In Addition, CFD generates smooth absorption coefficients curves while experimental curves embrace more fluctuations especially near the peak absorption frequencies.

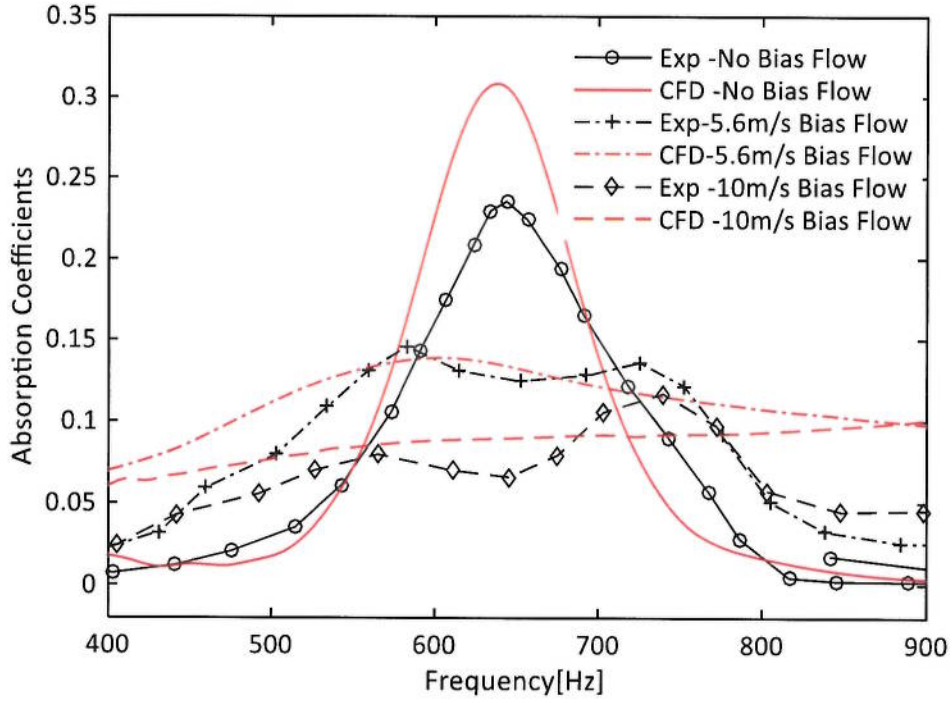

Figure 47 CFD and experimental comparison of absorption coefficients for plate H1 absorber in three bias flow conditions

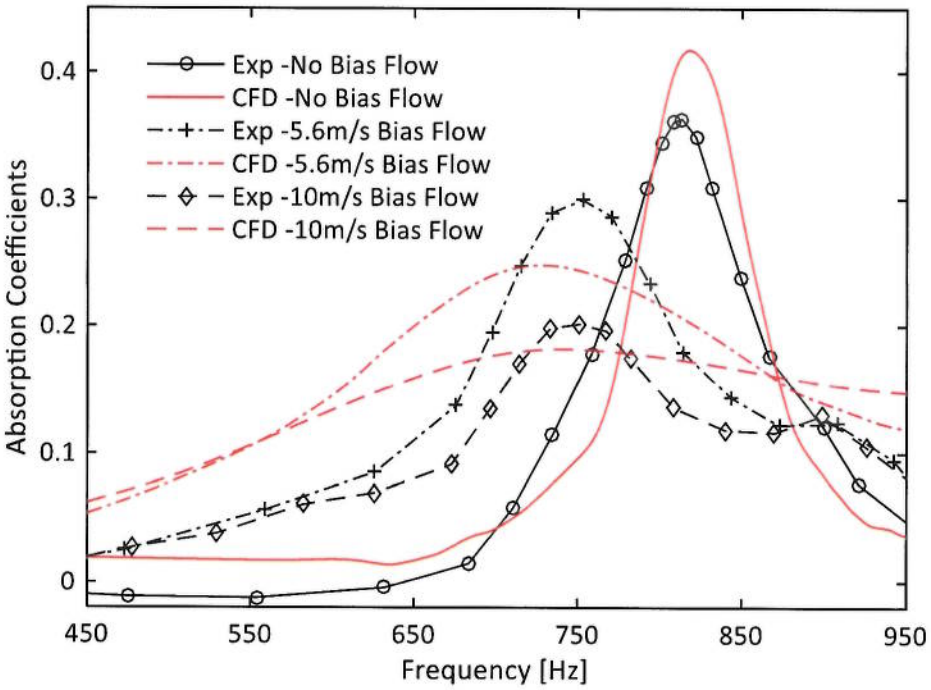

Figure 48 CFD and experimental comparison of absorption coefficients for plate H2 absorber in three bias flow conditions

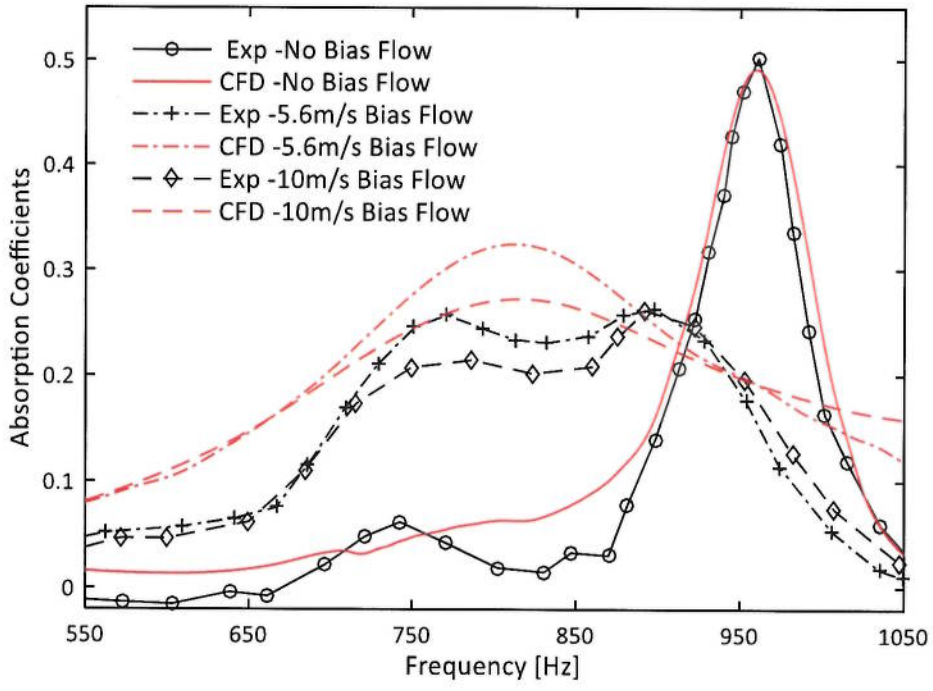

Figure 49 CFD and experimental comparison of absorption coefficients for plate H3 absorber in three bias flow conditions

5.4. Summary

In conclusion, the proposed CFD method is demonstrated to be able to obtain accurate prediction about acoustic properties of perforated liner absorbers in the presence of mean bias flows. Specifically, CFD method gives accurate prediction about the resonance frequencies in the presence of bias flow. It is also able to calculate the maximum absorption effect that can be achieved at the optimum bias flow speed. In addition, change of the absorption effect with bias flow speed is also predicted with high accuracy for two perforated liner absorbers. Experimental results of absorption coefficients for Eldredge's double layered liner absorbers with inclined perforations have also been successfully reproduced. Lastly, the impact of the liner thickness on the resonance frequency and absorption bandwidth of a perforated liner absorber has also been well represented by the CFD method. However, the CFD method tends to overestimate noise attenuation effect of perforated liner absorbers under low speed bias flow conditions.

6. Validation of the Porous Media Model in Predicting the Grazing Flow Effect on Acoustic Properties of Perforated liners

6.1 Review and Objectives

High temperature flue gas flows over the combustor liner surface and mixes with cold bias flow injections. A cooling flow film is thereby formed to prevent the direct contact of combustor wall with the high temperature grazing flow. Injected bias flow works as secondary air supply for the combustion process as well. Therefore, situations where only grazing flow is present are very rare in real gas turbine combustors. However, thorough understanding about how the proposed CFD method represents grazing flow effect is necessary before this CFD method is applied to investigate simultaneous bias/grazing flow effects. In this chapter, the flow and acoustic effect of pure grazing flow is firstly investigated. Study of the impact of simultaneous bias/grazing flow on acoustic properties of perforated liners is followed.

A number of experiments investigated grazing flow effects (Rao & Munjal, 1986; Dickey et al., 2001; Jing et al., 2001) and several empirical acoustic impedance models were established as well to accommodate grazing flow effect (Rice, 1971; Bauer, 1977; Kooi & Sarin, 1981; Kirby & Cummings, 1998; Lee & Ih, 2003). According to these works, flow resistance of a perforated liner rose linearly with the grazing flow speed:

$$r = \frac{C_g M_g}{\sigma} \qquad (128)$$

The rise of liner flow resistance with grazing flow speed was accredited to the local neck flow caused by grazing flow/orifice interactions (Sullivan, 1979). However, the current porous media model treats the liner region as a homogenous region by ignoring perforation geometry details. As a consequence, this porous media model is not able to numerically resolve the grazing flow induced resistance.

The number of research studying simultaneous grazing/bias flow effects is very small. Sun et al. (2002) plotted the discharge coefficients of perforated liners at

different M_b/M_g values and it could found that the discharge coefficient of a liner hardly changes if $M_b/M_g > 0.25$. Lahiri (2014) found similar conclusion in his experiment that grazing flow would not be able to affect the overall attenuation effect of a liner only if $M_b/M_g > 1/3$. Some other experiments (Eldredge & Dowling, 2003; Zhao et al., 2015) found that the effect of grazing flow was considerably weaker than the effect of bias flow in determining the overall attenuation effect of perforated liner absorbers.

Experimental study of acoustic properties of perforated liners in high temperature environments is also rare (Elnady et al., 2004; Rademaker et al., 2011; R.Kabral, 2014; Bodén & Kabral, 2015). Among those limited experimental works, Boden and Kabral (R.Kabral, 2014; Bodén & Kabral, 2015) found that temperature of grazing flow had very minor influence on the acoustic resistance of a liner. Same finding was also found by Rademaker et al. (2011) that the effect of flow temperature on acoustic resistance was very small. Elnany et al. (2004) experimentally tested the acoustic impedance of an orifice absorber in a high temperature impedance tube without the presence of any mean flow. He found that the change of acoustic impedance with temperature was entirely a result of the change of fluid properties such as the speed of sound and the density of air. Experiments by Elnady et al. (2004) and Kabral (2014) will be revisited in this chapter to validate the proposed CFD method in high temperature conditions.

6.2 Validation Experiments

6.2.1 Experiment of Jing's and Sun's

Jing et al. (2001) looked at how pure grazing flow impacted the acoustic impedance of four orifice plates. Figure 50 shows the test rig setup in his experiment. Grazing flow duct was a 120mm×120mm square tube. A closed 150mm long Ø35mm cylindrical cavity was fixed on the side wall of the grazing flow duct. A loudspeaker was installed on the opposite duct wall facing the cavity. Sound signal was a sine signal of 200Hz. Geometric features of the four orifice plates from this experiment are listed in Table 7. Transient pressure data were collected and processed by the method as described in Section 2.4.3.

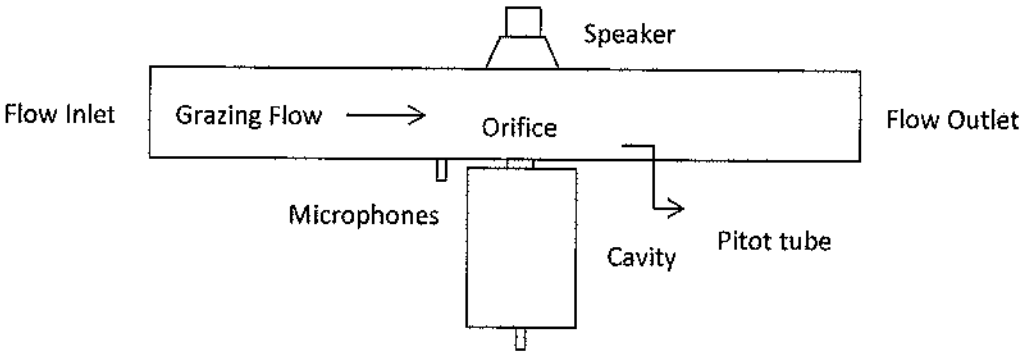

Figure 50 Test rig setup in Jing's experiment for the investigation of pure grazing flow effect (Jing et al., 2001)

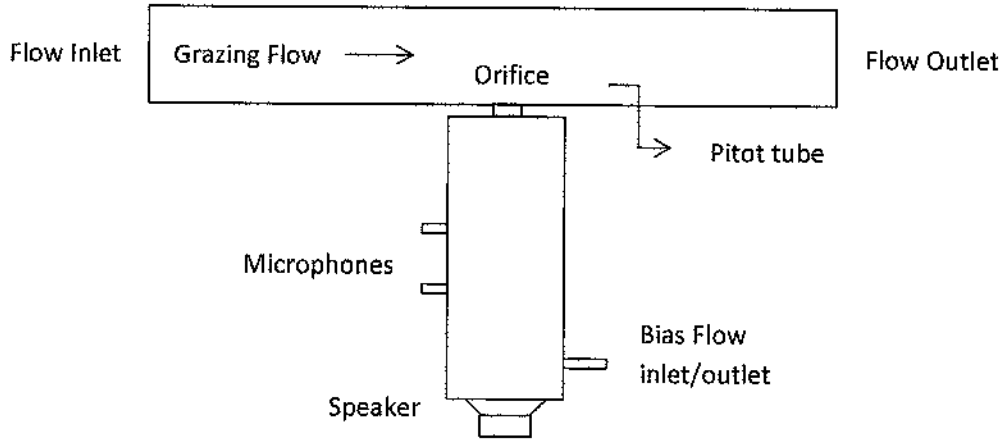

Figure 51 Test rig setup in Sun's experiment for the investigation of simultaneous bias/grazing flow effect (Sun et al., 2002)

Figure 51 shows the test rig setup in Sun's experiment (Sun et al., 2002) for the investigation of simultaneous bias/grazing flow effects. The closed cavity in Figure 50 was replaced by an impedance tube of the same diameter Ø35mm. A small pipe was linked to the impedance tube through which bias flow could be introduced in two ways: inflow and outflow. The inflow bias flow was compressed into the impedance tube and met with grazing flow in the grazing flow duct. The outflow bias flow was drawn into the impedance tube from the grazing flow duct. Only inflow cases are revisited by the proposed CFD method in this work because outflow means a reverse flow entering the cavity which is not realistic in gas turbine combustors. Geometric features of these three investigated orifice plates from this experiment are listed in Table 8. A sine wave signal of 500Hz was used. Transient

pressure data were collected and processed by the two-microphone transfer function method as described in Section 2.4.1.

Table 7 Geometric specifications of the orifice plates from the experiment by Jing et al. (2001)

Plate	Diameter	Thickness	Number of orifices	Porosity
JG1	3mm	2mm	4	2.94%
JG2	4.5mm	2mm	1	1.65%
JG3	7mm	0.5mm	1	4%
JG4	7mm	2mm	1	4%

Table 8 Geometric specifications of the orifice plates from the experiment by Sun et al. (2002)

Plate	Diameter	Thickness	Number of orifices	Porosity
JGB1	7mm	0.5mm	1	4%
JGB2	7mm	2mm	1	4%
JGB3	3mm	2mm	4	2.94%

6.2.2 Experiment of Elnady's and Kabral's

Elnady et al. (2004) experimentally tested the acoustic impedance of a single unit of honey-comb resonator in high temperature environments. The resonator unit was mounted on one end of an impedance tube which was placed in a constant high temperature oven as shown in Figure 52. Temperatures in the cavity were monitored. Microphones and loudspeaker were placed outside the high temperature oven and were provided with water circulation cooling system. Transient pressure data were collected and processed by the two-microphone transfer function method as described in Section 2.4.1. Those tested honey-comb resonator units were made of an orifice and a 19mm deep Ø10mm cylindrical cavity. Geometric details about the orifices are listed in Table 9. Only sample E2, E3 and E4 are revisited by CFD method as there is no available experimental result for sample E1. A stepped sine wave 400Hz-3500Hz was used and the frequency step was 50Hz near the resonance frequencies and was 100Hz in other frequency range. The

temperature acquired in the cavity in the experiment is taken to be the temperature of the air in CFD simulations.

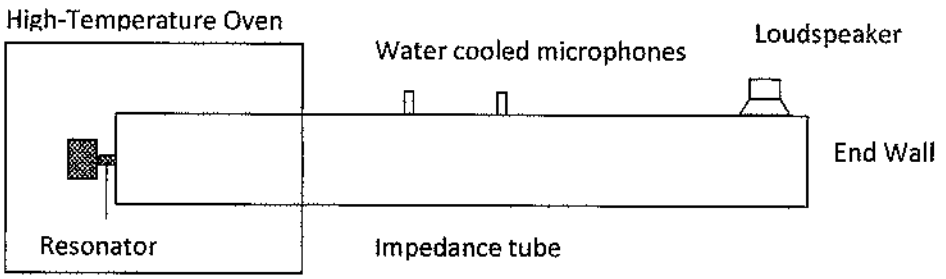

Figure 52 Schematic view of test rig setup in the experiment by Elnady et al. (2004)

Table 9 Geometric specifications of orifices and the temperatures in the cavity in the experiment by Elnany et al. (2004)

Sample	Diameter	Thickness	Porosity	Cavity temperatures
E1	1mm	2.3mm	1%	293K-589K
E2	1mm	1mm	1%	293K-563K
E3	1.5mm	1mm	2.25%	293K-551K
E4	1.5mm	0.5mm	2.25%	293K-545K

Experimental study of the effect of flow temperature only received very limited research efforts until recent years (Rademaker et al., 2011; R.Kabral, 2014; Bodén & Kabral, 2015). Experiment by Kabral's (2014) obtained the acoustic impedance of a perforated liner in low and high temperature grazing flow conditions. A 0.6mm thick plate was perforated by 23 Ø0.75mm circular orifices. The perforated liner was with a porosity of 16.3% and backed by a 19mm deep air cavity. The cavity was made of 4×8 small square cavities and each cavity has a cross section of 6.9mm×6.9mm. The perforated liner absorber was installed on one side wall of a 36mm×36mm square flow duct as shown in Figure 53. A stepped sine wave was used and the frequency step was 50Hz.

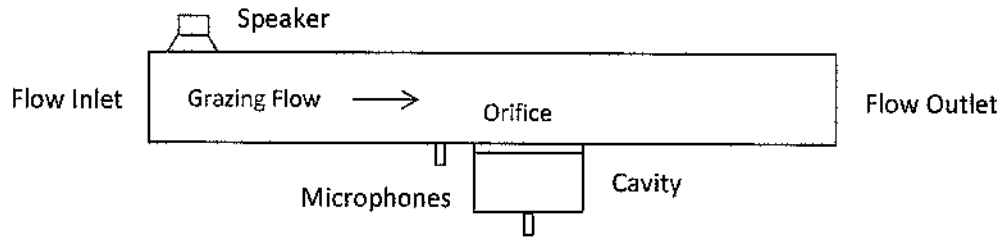

Figure 53 Schematic view of the test rig setup in the experiment by R. Kabral (2014)

6.3 Results and Discussion

6.3.1 Grazing Flow and Zero Bias Flow

As have been discussed, the homogenous porous media model is probably not able to resolve the grazing flow effect due to its incapability to account for grazing flow/orifice structure interaction effects. Figure 54 illustrates a test case where a 35mm×35mm plate is placed in 34m/s grazing flow conditions. The plate is perforated by nine Ø3mm orifices and is backed by a closed cavity. Two CFD simulations are carried out and the obtained velocity profiles in the liner are compared in Figure 55. The perforated plate is treated as a homogenous porous media region in the first simulation while the real orifice geometries are directly resolved in the second simulation. The mesh resolution and distribution situations for the two different methods can be found in Figure 10.

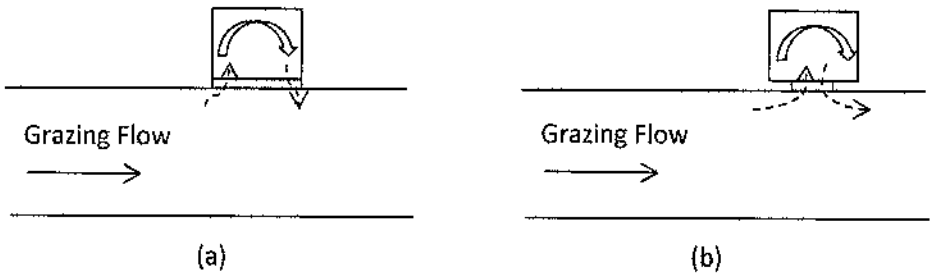

Figure 54 Illustration of the two CFD simulations for a perforated liner (a) treating the liner as a homogenous porous media region (b) resolving real orifices

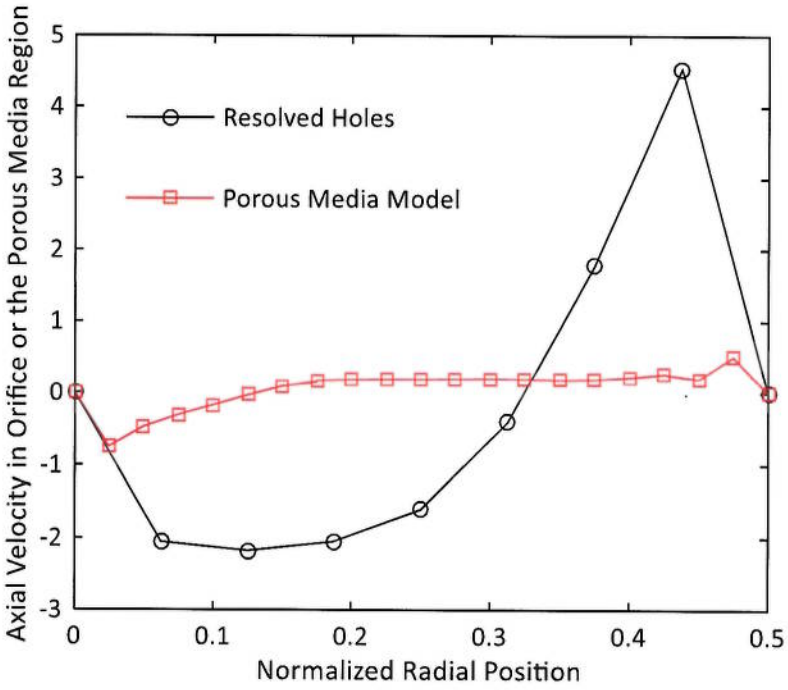

Figure 55 Axial velocity profiles in a resolved orifice and that in the equivalent porous media region.

Figure 55 compares axial velocity profiles in a directly resolved orifice and that in an equivalent porous media region. The radial position is normalized by the diameter of the orifice and the diameter of the perforated liner respectively. A strong local neck flow is observed when the orifices are directly resolved. However, the local flow is hardly observed in the porous media region when the liner is represented by an equivalent porous media zone. This confirms that the porous media model is not able to reflect grazing flow induced local neck flows. To remedy this issue, flow resistance of the porous media region is empirically included following Equation (107) in CFD simulations.

Acoustic impedance of the four orifice plates from Jing's experiment (Jing et al., 2001) are obtained by the CFD method under various grazing flow conditions. CFD generated normalized specific acoustic impedance is compared with experimental results in Figure 56. Both CFD and experimental methods suggest that acoustic resistance rises linearly with grazing flow Mach number. More precisely, experimental results indicate the linear proportional constant to be 0.39, 0.41, 0.5, 0. 48 for plate JG1, JG2, JG3, JG4 respectively. Correspondingly, the CFD results

indicate 0.385, 0.417, 0.45, 0.45 for these four plates which are close to experimental values. This demonstrates that CFD method is able to represent the grazing flow induced resistance by empirically including the resistance term according to Equation (107). In addition, CFD and experimental results agree that the magnitude of acoustic reactance decreases with increasing grazing flow speeds and the decrease tends to slow down in high grazing flow speeds. However, the magnitude of the acoustic reactance is much smaller than the magnitude of acoustic resistance in the presence of large scale mean flows. According to Equation (45), acoustic reactance becomes insignificant in determining the overall sound attenuation effect of these perforated liner absorbers.

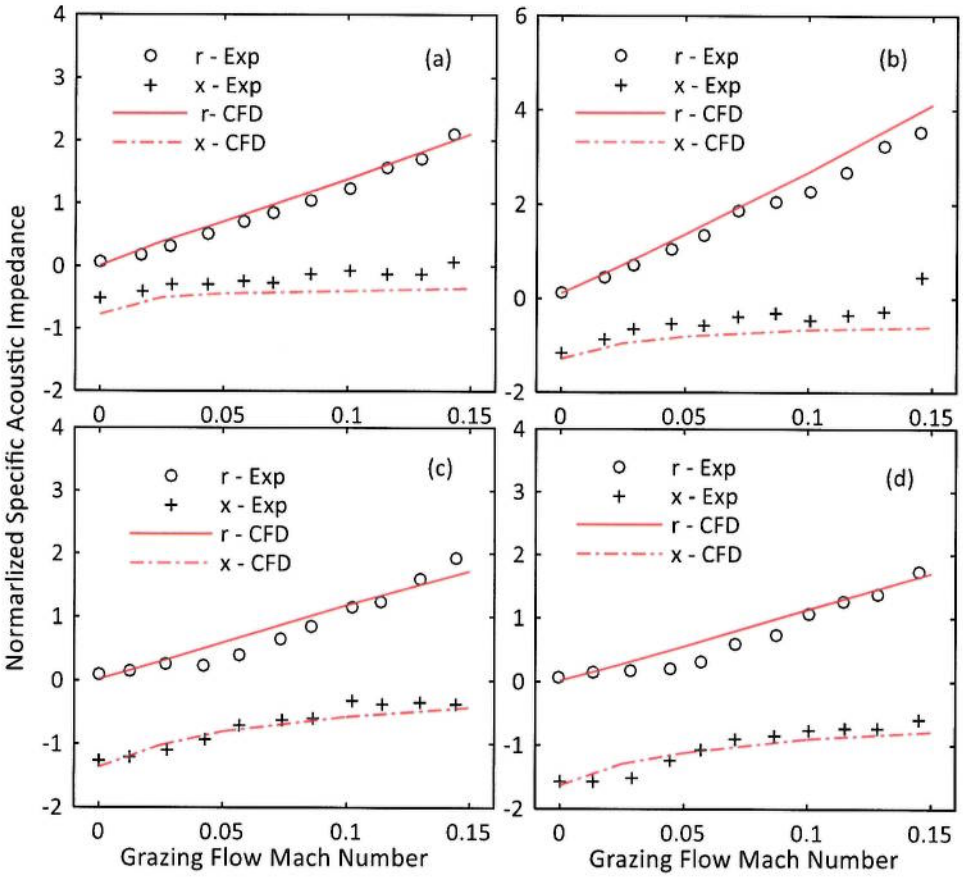

Figure 56 CFD and experimental comparison of normalized specific acoustic impedance as a function of grazing flow Mach number for (a) plate JG1 (b) plate JG2 (c) plate JG3 (d) plate JG4 (Jing et al., 2001)

6.3.2 Simultaneous Grazing and Bias Flow

CFD and experimental comparison of normalized specific acoustic impedance of plates JGB1, JGB2 and JGB3 from Sun's experiment (Sun et al., 2002) under various simultaneous bias/grazing flow conditions is provided in Figure 57, Figure 58 and Figure 59. First of all, all three figures show that the presence of bias flow tends to reduce the impact of grazing flow and the change of acoustic resistance with grazing flow speed is more obvious when bias flow is weak. For instance, when $M_b = 0.01$, acoustic resistance of plate JGB1 is amplified by three times from approximately 0.6 at $M_g = 0$ to 1.9 at $M_g = 0.174$. However, when $M_b = 0.1$, the resistance only changes from 5.6 at $M_g = 0$ to 4.5 at $M_g = 0.174$. The change of acoustic resistance with grazing flow speed is much less significant in the presence of strong bias flow.

Second, CFD method successfully captures the effect of grazing flow on the acoustic resistance of all three liners when bias flow is very weak. This is achieved by empirically including the grazing flow induced flow resistance according to Equation (108). CFD results are also in satisfactory agreement with experimental results under high speed bias flow conditions and this is achieved by ignoring grazing flow effect in CFD simulations. However, experimental results indicate that the existence of grazing flow tends to bring down acoustic resistance in simultaneous bias/grazing flow conditions which is termed as "negative grazing flow effect" (Sun et al., 2002). The 'negative grazing flow effect' is beyond the capability of current CFD methodologies.

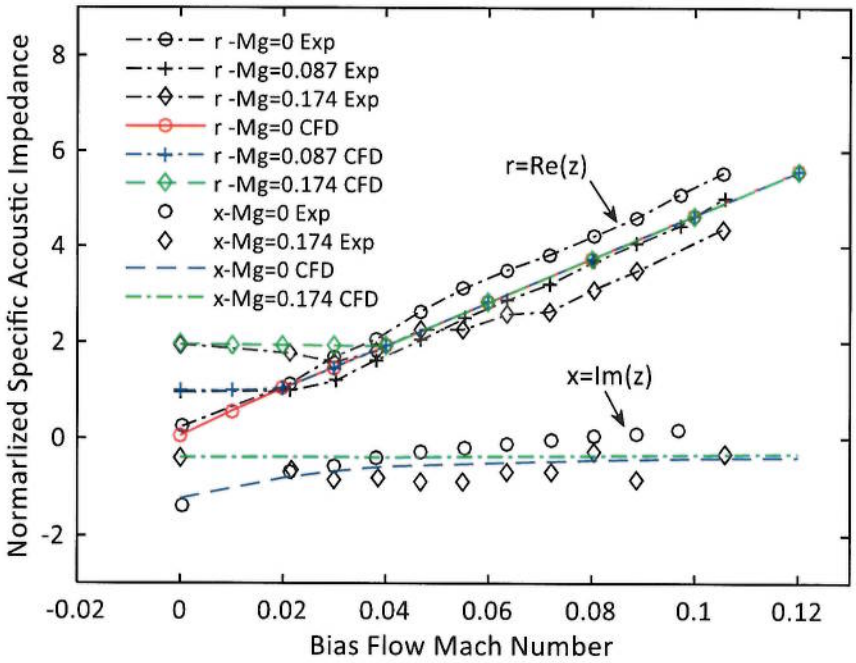

Figure 57 CFD and experimental comparison of normalized specific acoustic impedance for plate JGB1 under various bias/grazing flow conditions (Sun et al., 2002)

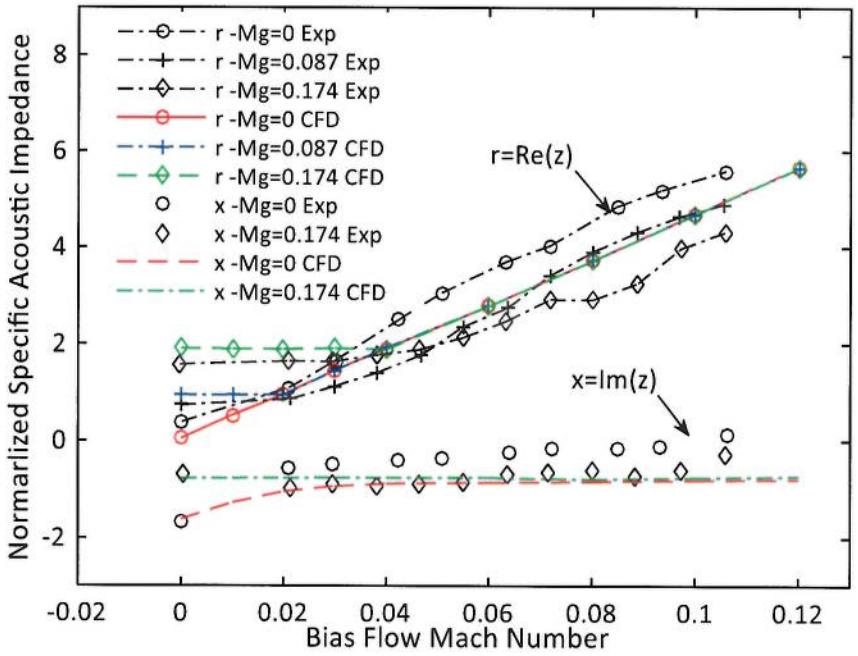

Figure 58 CFD and experimental comparison of normalized specific acoustic impedance for plate JGB2 under various bias/grazing flow conditions (Sun et al., 2002)

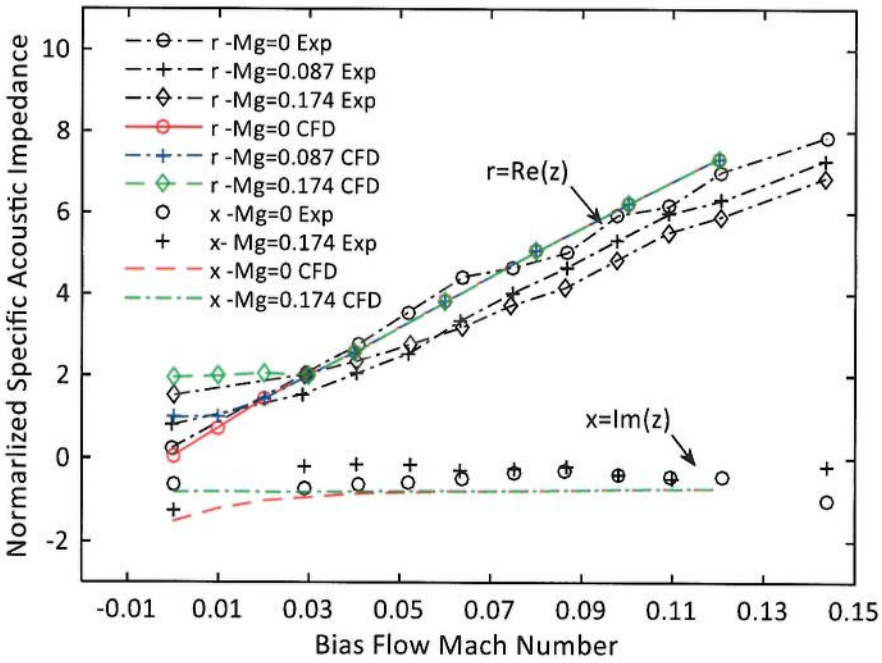

Figure 59 CFD and experimental comparison of normalized specific acoustic impedance for plate JGB3 under various bias/grazing flow conditions (Sun et al., 2002)

The empirical inclusion of *a priori* grazing flow induced resistance appears to reduce. However, on the other hand, many researchers (Rice, 1971; Dean & Tester, 1975; Lahiri, 2014) found that the effect of the grazing flow on noise attenuation effect of perforated liners was inappreciable if $M_b/M_g > 0.25 - 0.33$. This criterion is often satisfied in most gas turbine engines in order to provide sufficient effusion cooling effects (Tonon et al., 2013). It is bias flow rather than grazing flow that is the determining factor in most gas turbine flow conditions and bias flow resistance is numerically resolved by the physical velocity porous media model as explained in Section 3.3.5. Therefore, the empirical input of grazing flow induced resistance only affects the numerical robustness of the proposed porous media model in those rare situations where grazing flow is dominant.

Acoustic reactance curves are obtained by CFD method with reasonably accuracy as well as shown in Figure 57, Figure 58 and Figure 59. However, acoustic reactance is insignificant in determining the overall attenuation effect of perforated liners. This can be explained by Equation (45) that the much larger magnitudes of acoustic

resistance overwhelms the impact of acoustic reactance. In general, experimental effects of simultaneous bias/grazing flow on the acoustic impedance of perforated liners are reproduced by the proposed CFD methodology with fairly good accuracy.

6.3.3 Temperature of the Flow

Figure 60 shows the mesh distribution for CFD calculations of the experiment of Elnady et al. (2004). 2 layers of meshes are built in the thickness direction of the perforated plate. 20 meshes are built in the radial direction of the impedance tube and at least 20 meshes are guaranteed within one wavelength of the tested signals in the sound propagation direction.

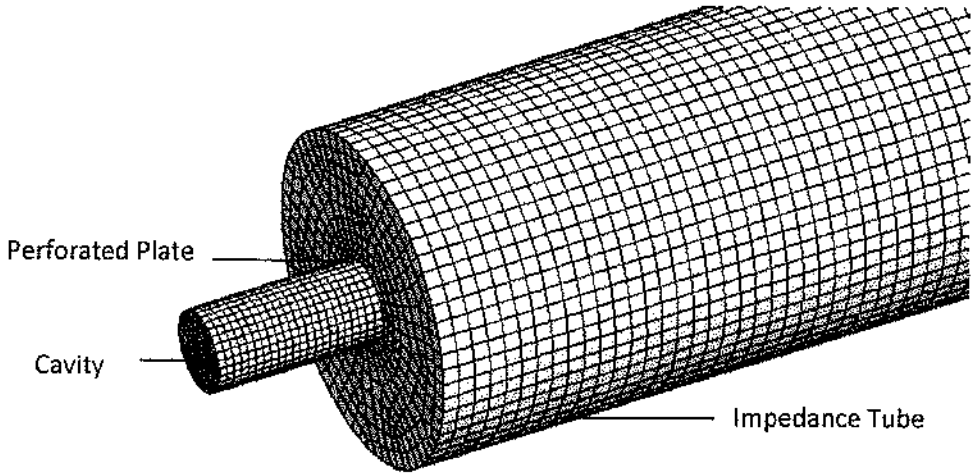

Figure 60 Mesh distribution for the CFD simulation for the experiment of Elnady et al. (2004)

CFD and experimental comparison of acoustic impedance for those resonators from Elnady's experiment (Elnady et al., 2004) is displayed in Figure 61, Figure 62 and Figure 63. All three figures indicate that the impact of air temperature on acoustic resistance of these resonators is very minor across a wide frequency range. By contrast, the acoustic reactance curves are obviously translated to higher frequencies in high temperature conditions. The magnitude of acoustic reactance is much larger than that of acoustic resistance at most frequencies.

Elnady et al. (2004) argued that the influence of temperature on acoustic impedance of liner absorbers was entirely due to its influence on relevant fluid properties such as density and viscosity of the air and the speed of sound.

According to Equation (45), acoustic resonance of an absorber occurs at the frequency where acoustic reactance is zero. According to Equation (46), the resonance frequency of an absorber increases linearly with the speed of sound which is in turn proportional with the square root value of the temperature.

Acoustic reactance curves generated by CFD and experiment agree closely across a wide frequency range. Both methods indicate that the resonance frequency of the absorbers is amplified by 1.4-1.45 times due to an air temperature increase from 293K to about 560K. This finding coincides with the theoretical prediction that resonance frequency of an absorber rises linearly with the square root value of the temperature. The success of CFD method is credited to its capability in representing the variation of air properties with temperature and this is achieved by using ideal gas state equations and temperature-dependent viscosity laws in CFD simulations.

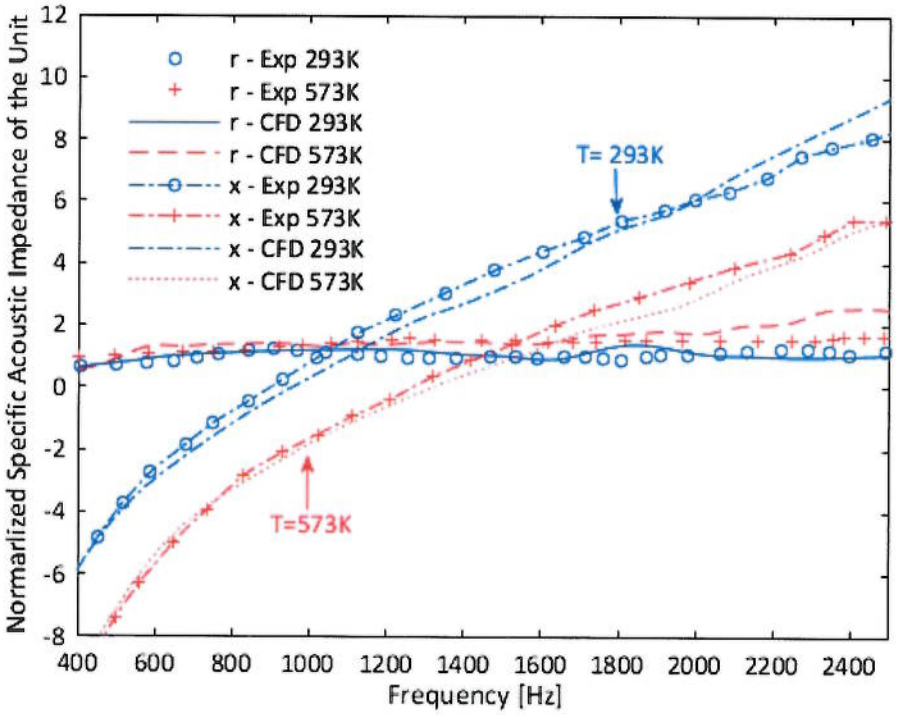

Figure 61 CFD and experimental comparison of normalized specific acoustic impedance of sample E2 at 120dB (Elnady et al., 2004)

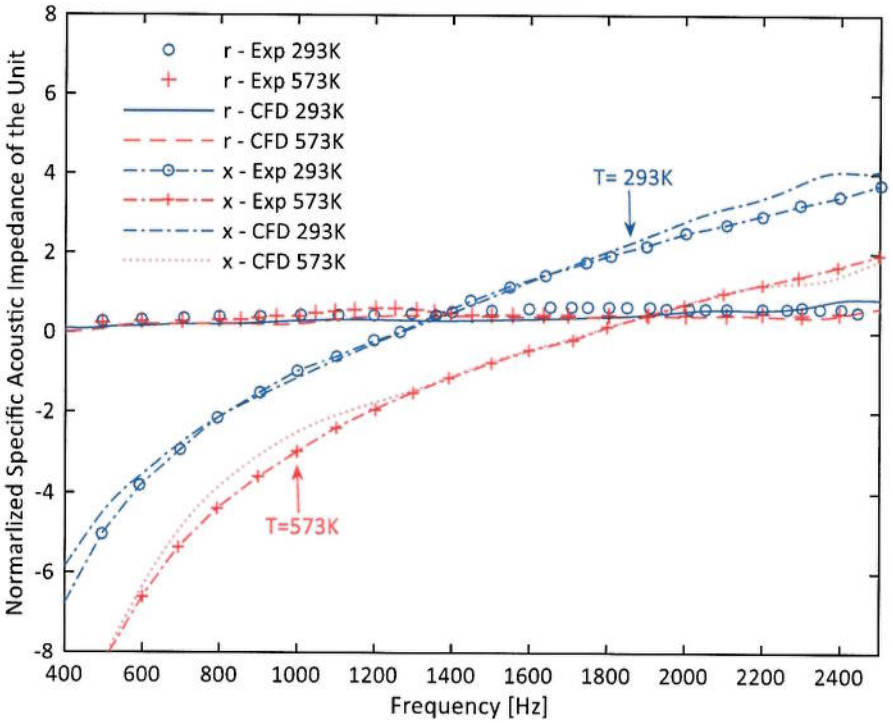

Figure 62 CFD and experimental comparison of normalized specific acoustic impedance of sample E3 at 120dB (Elnady et al., 2004)

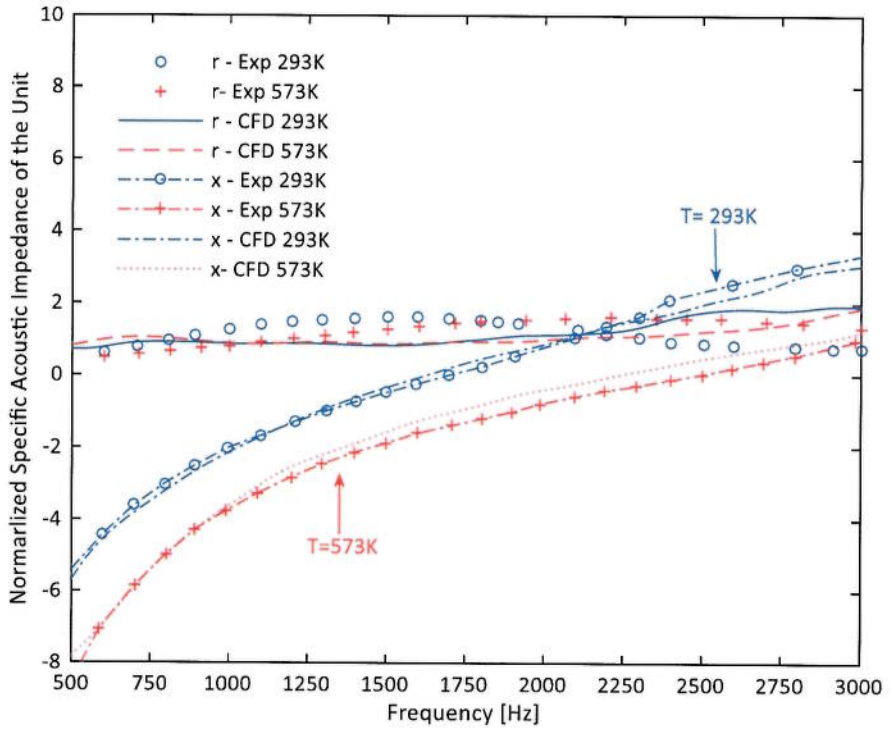

Figure 63 CFD and experimental comparison of normalized specific acoustic impedance of sample E4 at 140dB (Elnady et al., 2004)

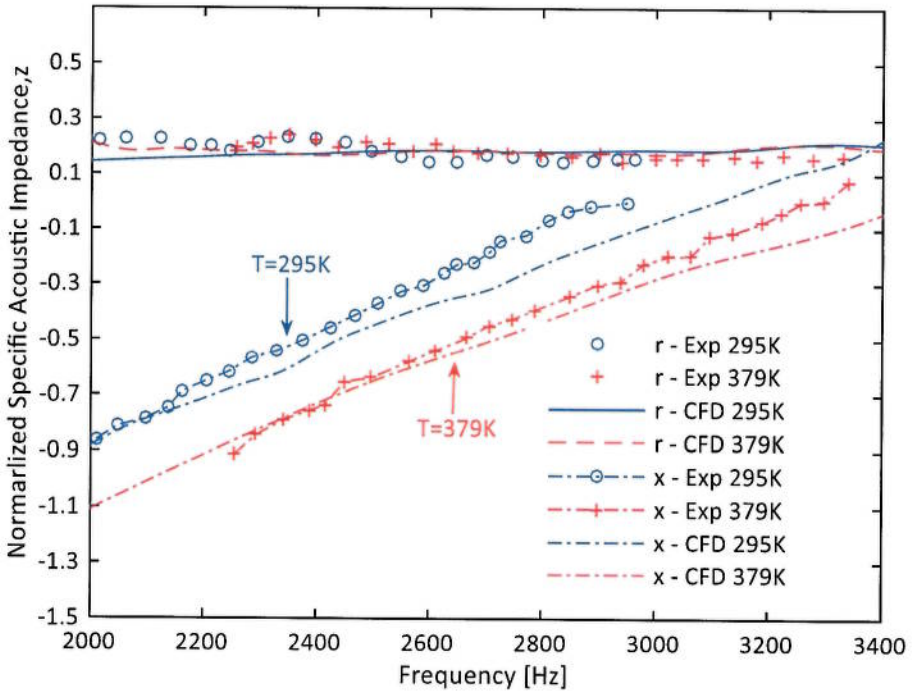

Figure 64 CFD and experimental comparison of normalized specific acoustic impedance ($M_g = 0.12$) (R.Kabral, 2014)

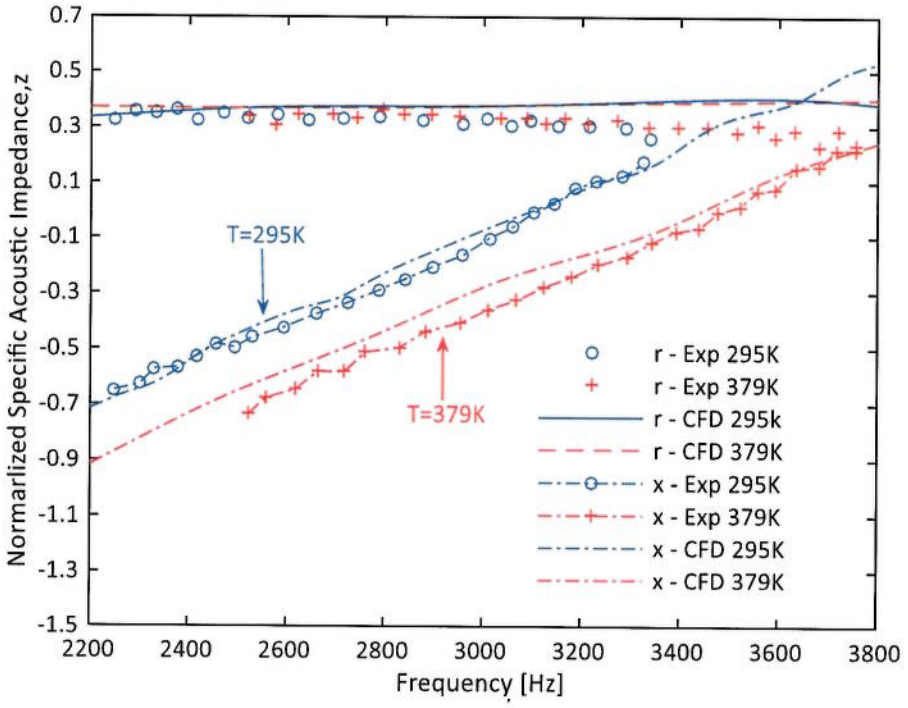

Figure 65 CFD and experimental comparison of normalized specific acoustic impedance ($M_g = 0.25$) (R.Kabral, 2014)

Figure 64 and Figure 65 display similar comparison of acoustic impedance acquired by CFD and experimental method for the panel absorber from Kabrail's experiment (R.Kabral, 2014). Effect of grazing flow temperature has been investigated in this experiment. Both CFD and experimental results suggest that the effect of temperature on normalized acoustic resistance is very minor in the presence of mean grazing flow. The temperature of grazing flow only changes acoustic reactance by translating acoustic reactance curves to higher frequencies. These findings are identical with those found in Elnady's experiment (Elnady et al., 2004).Summarizing both experiments, we come to conclude that the effect of flow temperature on acoustic resistance of perforated liners is especially weak, high temperature of the air only modifies acoustic reactance by shifting those reactance curves of perforated liner absorbers to higher frequencies. This influence of temperature on acoustic impedance is entirely due to the changes of fluid properties with temperatures such as the speed of sound and density of the air.

6.4 Summary

The proposed CFD method is tested in terms of its capability in capturing grazing flow effect on acoustic properties of perforated liner absorbers. The local neck flow caused by grazing flow/orifice interaction is proved to be beyond the capability of the porous media model. Grazing induced flow resistance has thus to be included empirically in CFD simulations according to Equation (107). Experimental acoustic impedance results from the experiment by Jing et al. (2001) has been reproduced with decent accuracy by this method.

Simultaneous bias/grazing flow conditions investigated in Sun's experiment (Sun et al., 2002) are revisited and the CFD acquired results are in satisfactory agreement with experiments both in grazing flow dominant situations and bias flow dominant situations. Last, the experimental finding (Rademaker et al., 2011; R.Kabral, 2014) that the temperature of flow has negligible impact on the acoustic resistance of perforated liners is successfully confirmed by the CFD method. The effect of temperature only manifests itself by translating reactance curves to higher

frequencies due to its impact on fluid properties such as the viscosity and the density of air and the speed of sound.

With the success of the proposed CFD method in resolving acoustic properties of perforated liners in simultaneous grazing/bias flow and high temperature flow conditions, applying this CFD method to simulate the three-dimensional swirling and reacting flows in the gas turbine combustor becomes a realistic next step.

7. Application of the Proposed CFD Methodology in the Gas Turbine Combustor 'PRECCINSTA'

7.1 Review and Objectives

'PRECCINSTA' is an abbreviation for 'Prediction and Control of Combustion Instabilities in Industrial Gas Turbines' which is an European Commission funded research project. It is Turbomeca which first came into the combustion instability problem within one of their lean premixed combustor engines. The combustor geometry and operating conditions were then scaled down to a lab-scale combustor and was sent to DLR research centre for experimental tests (Tidjani et al., 2001). DLR research centres carried out experimental measurements of some key flow parameters such as velocities and temperatures in this lab-scale combustor. They also successfully obtained the unsteady pressure oscillations and a pulsating flame under specific operation conditions (Kelsall & Troger, 2004; Lartigue et al., 2004). This project has led to a better understanding of the combustion instability mechanism, and at the same time it became a reliable database which could be used to validate the capability of large eddy simulations in the study of combustion instability issues such as those efforts made by Roux et al. (Roux et al., 2005; Bulat et al., 2014; Wang et al., 2014).

A schematic view of the combustor is shown in Figure 66. Air was compressed through a plenum (Ø78mm) in to the swirler section. Methane was injected through 12 radially distributed tubes (Ø1mm). The injected methane was of high speed because of the small diameter of injection tubes and it then mixed with the air flow very efficiently in the swirler vanes. The fuel/methane mixture was strongly swirling and turbulent upon entering the combustion chamber. The combustion chamber had a square cross section of 85mm×85mm and its wall was made of a 1.5mm thick transparent quartz window through which the laser measurements were able to be carried out. Combustion chamber was 114mm high[2] and linked to a 50mm long cylindrical exit. The contraction ratio between combustion chamber and the exit was 6:1. The facility was warmed up for nearly 30 minutes before air/fuel

3. The height of the PRECCINSTA varies from 110mm to 114mm in different publications.

mixture is ignited. As a result, the air/fuel mixture temperature was effectively raised to 320K-380K prior to the occurrence of chemical reactions (Meier et al., 2007; Wang et al., 2014). Velocities and temperatures at several locations as shown in Figure 67 were experimentally measured in the "PRECCINSTA" combustor.

DLR Stuttgart performed the Raman LIF, and chemiluminescence measurements for two type of flames (Meier et al., 2007). The first flame was with a lower fuel/air equivalence ratio (Φ=0.70), a strong pulsating flame and self-excited pressure oscillation in the combustion chamber were observed in this case. The second flame was with a higher fuel/air equivalence ratio (Φ=0.83) and it was a much 'quieter flame' compared with the first flame. Another lower equivalence ratio flame (Φ=0.75) was tested by DLR Centre in Berlin by LDV measurements. Flow conditions of these three experiments are summarized in Table 10 (Meier et al., 2007). Figure 67 shows the measurement height positions for velocities and temperatures in experiments. Velocity and temperatures information will be reproduced from large eddy simulations at the same height locations and will be compared with experimental results.

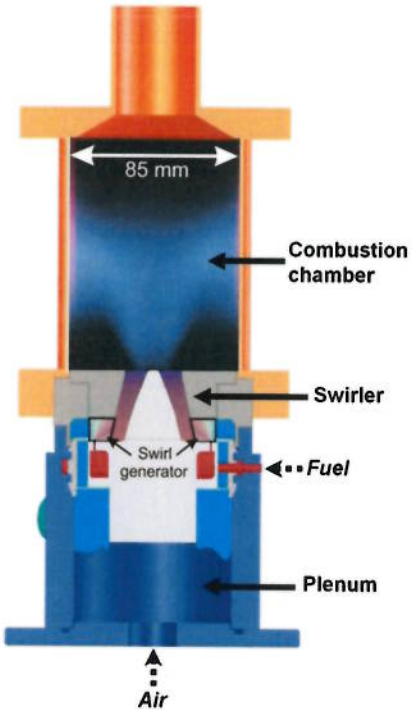

Figure 66 Schematic view of the "PRECCINSTA" combustor (Meier et al., 2007)

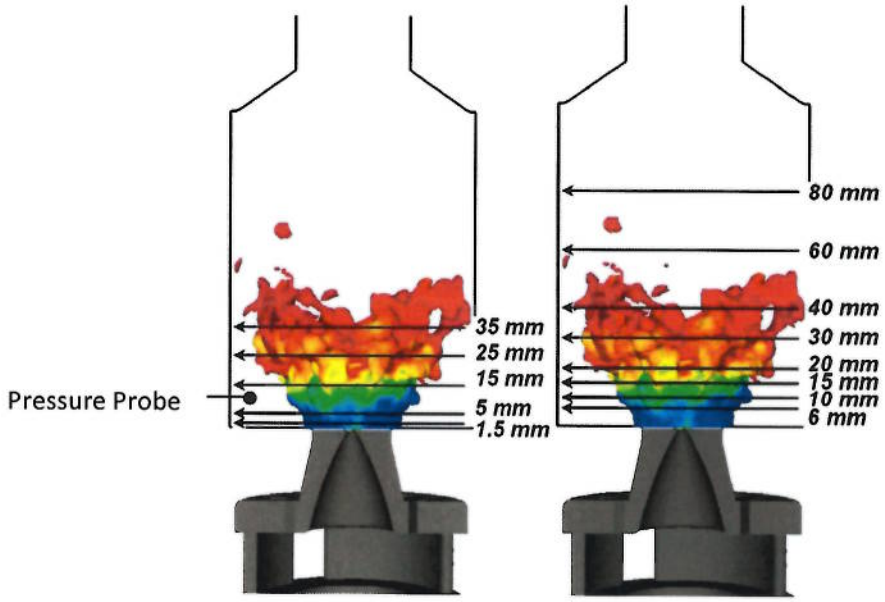

Figure 67 Probe positions for velocity (left) and temperature (right) measurements

Table 10 Three investigated flames at DLR

Flow condition	Air flow rate	CH4 flow rate	Thermal Power	Equivalence Ratio
1	734.2g/min	30g/min	25kW	0.70
2a	734.2g/min	35.9g/min	30kW	0.83
2b	734.2g/min	45g/min	27kW	0.75

A large number of large eddy simulations for swirling flows and reacting flows in various combustors such as TECFLAM combustor, Sydney combustor and PRECCINSTA combustor have been thoroughly reviewed by Gicquel et al. (2012). By reviewing those works, He concluded that large eddy simulation was not only able to predict the mean flow field with high accuracy; it also could be used to capture the fluctuation magnitudes of key flow parameters in unsteady swirling flows. As regard to the "PRECCINSTA" combustor, Several LES efforts (Roux et al., 2005; Albouze, 2009; Fiorina et al., 2010; Moureau et al., 2011; Wang et al., 2014) were made to reproduce the self-excited pulsating flame and these simulations confirmed that large eddy simulation was able to provide highly accurate prediction about the mean flow field in "PRECCINSTA" combustor and was able to generate satisfactory results about the fluctuation magnitude of velocities and pressures as well.

In this work, validation of LES will be firstly repeated for the flow condition 2b as described in Table 10 to confirm its ability in obtaining mean flow fields and fluctuation magnitudes of some key variables such as velocity and reacting flow temperature. Then, LES will be applied to capture the pressure instability modes in the combustion chamber and the results will be compared with experimental results. Lastly, several perforated liners will be designed and installed on the combustor wall and be treated as porous media regions in CFD simulations in order to prove that the proposed CFD methodology is able to capture the noise attenuation effect of the perforated liners in complex flow conditions.

7.2 Meshing and Modelling Strategies

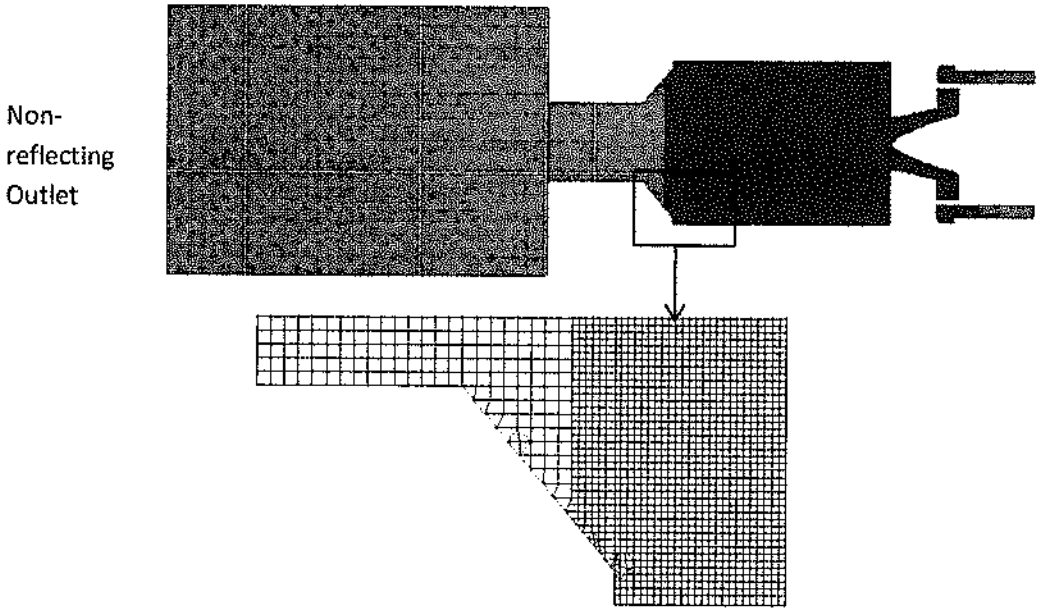

Figure 68 Illustration of the meshes in "PRECCINSTA" combustor

The flue gas in "PRECCINSTA" combustor flows out of the choked exit to a large open space. The consequent acoustic wave reflection from this region due to the flow area discontinuities could significantly affect the acoustic field and flow dynamics inside the combustion chamber. Therefore, a large external zone behind the flue gas exit is included in current CFD calculations so that acoustic wave reflections at the combustor exit are directly resolved. External boundary of this large zone is set to be non-reflecting to emulate the open atmosphere.

Large eddy simulation has to be resolved on sufficiently fine meshes so that influential eddies of the small scale could be directly resolved. Meshes applied in this work are shown in Figure 68. The size of hexahedral meshes (Δ_x) is 1.2mm in the air inlet duct, choked combustor exit and outer zone and it is refined to 0.6mm in the swirler and combustion chamber. 4.2 million structured hexahedral meshes are built in the calculation domain, a few hundred of tetrahedral meshes are present yet only where structured hexahedral meshes are not easily acquirable. Large eddy simulation filters were developed based on regular structured grids and they tend to yield higher accuracy when resolved on structured meshes than on anisotropic irregular unstructured grids (Ghosal & Moin, 1995; Scotti et al., 1997; Selle et al., 2004a). Large eddy simulations on unstructured meshes of 0.5mm-0.6mm has been justified to be able to obtain mesh independent results for the flow filed in "PRECCINSTA" combustor (Moureau et al., 2011; Mercier et al., 2015). Therefore, confidence is given to the 0.6mm structured meshes used in this work.

Transient large eddy simulations start from the mean flow field acquired by RANS method in order to reduce the time needed for the LES simulation to reach a statistically stable mode. Combustion is modelled as partially premixed process, of which the non-premixed combustion process is modelled by the conserved mixture fraction method assuming a chemical equilibrium state and fast chemical reaction process (Jones & Whitelaw, 1982). Premixed reaction is modelled by progress variable method (Pierce & Moin, 2004). Both the mixture fraction method and the progress variable method involve significant approximations and combustion modelling results by these methods may not be as accurate as those acquired by more sophisticated models. However, both methods are very robust in terms of generating reasonable flow field prediction for a variety of reacting flow conditions (Cook & Riley, 1994; Pierce & Moin, 1998; Pitsch, 2006; Sadiki & Janicka, 2006; Veynante, 2009).

Acoustic waves, in essence, are the response of the compressible medium to external pressure fluctuations. Therefore, the modelling of acoustic issues requires the compressibility effect of the flow to be taken into account. Transient terms are resolved in the bounded central second order implicit method. Time step of large

eddies simulation are taken to be as small as 0.01ms for reacting flow cases and 0.02ms for non-reacting flow cases so that the maximum flow Courant number in the calculation domain is not noticeably greater than unity. The effect of sub-grid scale eddies is modelled by WALE sub-grid stress model (Fluent, 2009). The computational time required for a simulation case for cold flow and reacting flow conditions is approximately 36 hours and 72 hours per simulation using 400 Broadwell E5 processing cores. Large eddy simulations are run for at least 3 lapses of combustor flow-through time before the acoustic pressure information is taken to ensure that flow and acoustic fields in the combustor have reached a statistically stable state. One flow-through time for cold flow conditions and reacting flow conditions are respectively 0.05s and 0.02s.

7.3 Results and Discussion

7.3.1 Non-reacting Flow

Figure 69 and Figure 70 show the axial velocity contour in a vertical cross section of the combustor. Unsteady RANS method along with standard $\kappa - \epsilon$ model yields much smoother velocity field without showing many noticeable vortex structures while LES generated contour indicates much more transient turbulence information. The mean value and root mean square value of axial velocities under non-reacting flow conditions obtained by RANS and LES are compared with experimental results in Figure 71 and Figure 72. Figure 71 proves that both methods are able to obtain the mean flow field with very high accuracy. On the other hand, Figure 72 shows that RANS method loses nearly all of the fluctuation strength soon after the fuel/air mixture enters the combustion chamber. By contrast, LES generated results exhibit much closer agreement with experimental data. Therefore, LES method is demonstrated to be the only applicable method for the purpose of capturing self-excited flow instabilities. Other simulation works have also found that RANS method tend to lose unsteadiness magnitude when it is applied to predict the evolution of self-excited unsteady dynamics such as vortex shedding and swirling flow (Rodi, 1997; Benhamadouche & Laurence, 2003; Boudier et al., 2007).

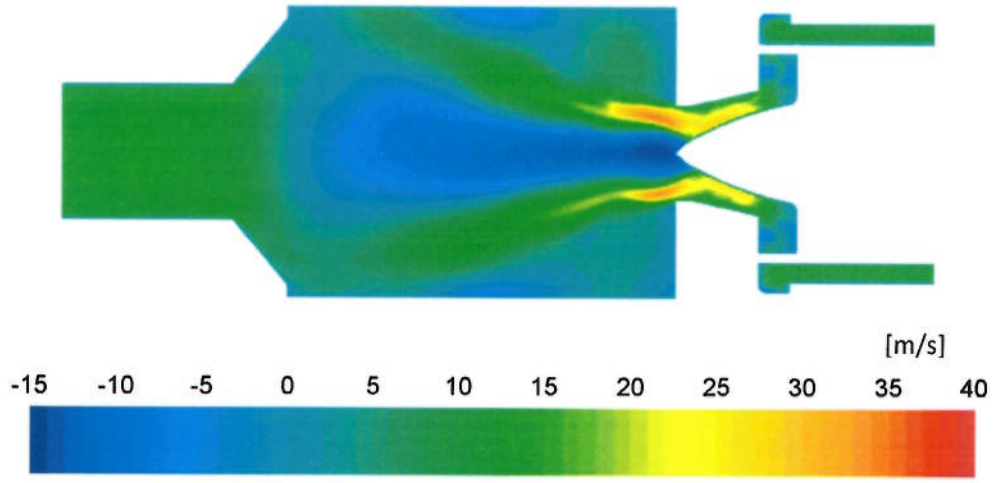

Figure 69 Axial velocity contour obtained by RANS method with standard $\kappa - \epsilon$ model at t=0.2s

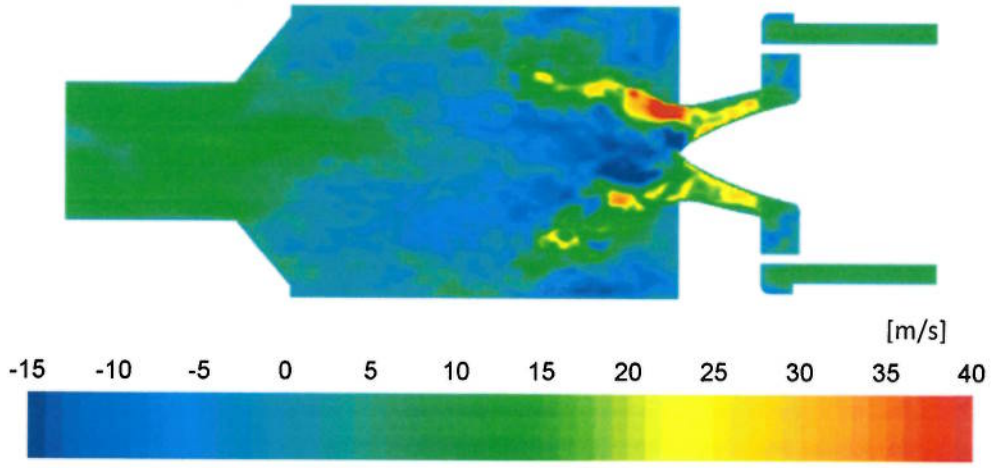

Figure 70 Axial velocity contour obtained by LES method at t=0.2s

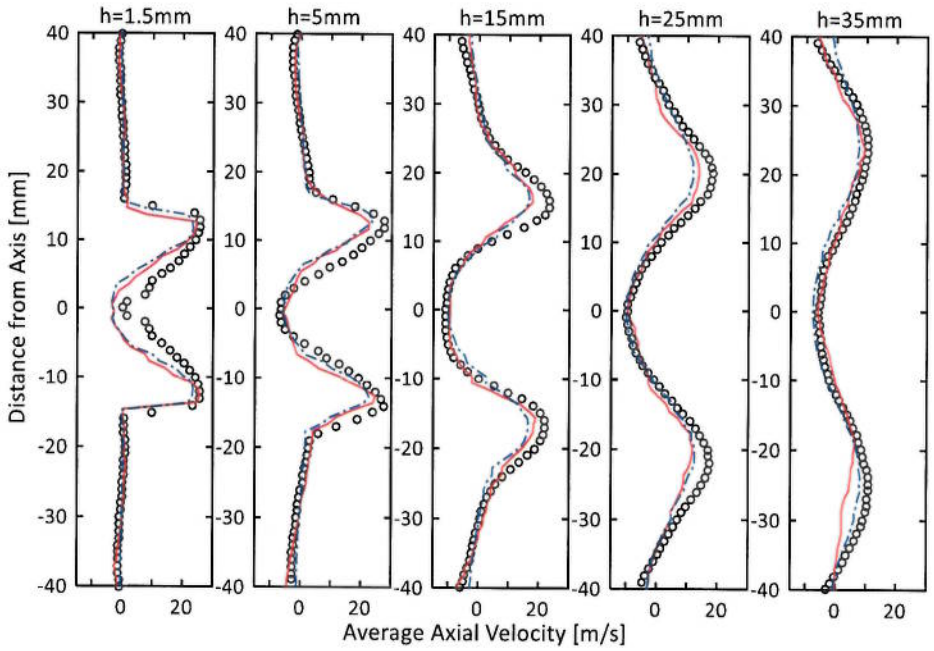

Figure 71 Mean axial velocity obtained by experiment (black dots), LES (red solid line) and RANS method (blue dash dot line)

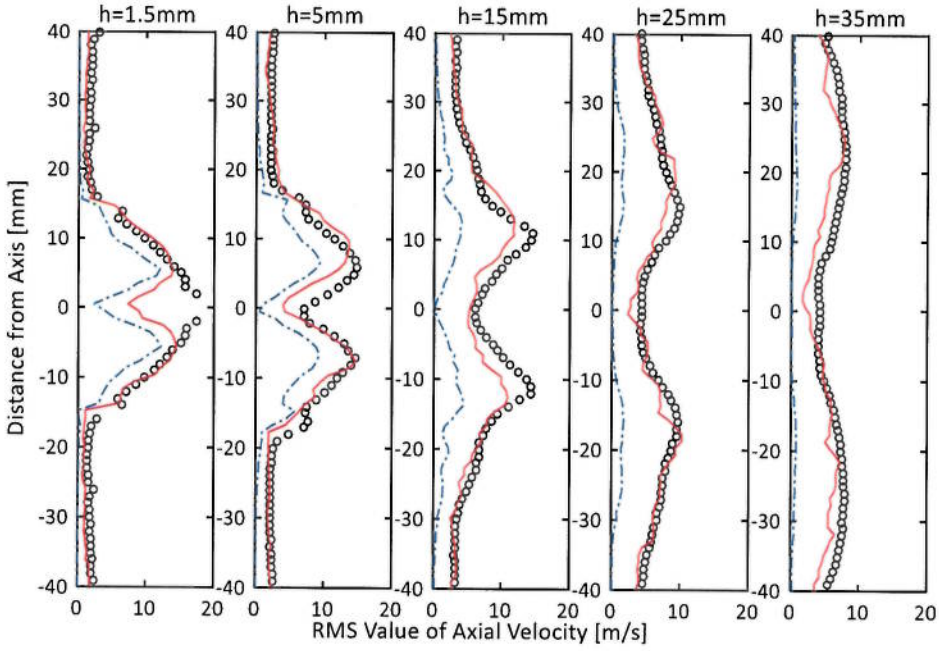

Figure 72 RMS value of axial velocity obtained by experiment (black dots), LES (red solid line) and RANS method (blue dash dot line)

Figure 73 provides the pressure spectrum in the frequency-domain at the bottom corner of the combustor in non-reacting flow situations as shown in Figure 67.

Experimental result shows a very sharp 520Hz peak in the spectrum which is claimed to be due to the precessing vortex core near the swirler exit (Roux et al., 2005). This precessing vortex core induced pressure instability mode is successfully captured in the pressure spectrum obtained by large eddy simulations, however at a slightly lower frequency 480Hz. Large eddy simulation also suggests a secondary instability mode near 200Hz which is very close to the 172Hz mode suggested by the Helmholtz solver (Roux et al., 2005), however this mode was not found in the experiment. Figure 74 illustrates the precessing vortex core captured by large eddy simulations for the cold swirling flows at the swirler exit. The precessing vortex core oscillates around the swirler axis at the frequency of 480Hz in large eddy simulations while the experimentally measured value is 510Hz. This oscillating hydrodynamic structure then leads to oscillating pressure field in the combustor which is shown as a 480Hz acoustic mode in the combustor.

Figure 75 plots the pressure spectrums at a position of 3cm outside the choked exit. The 480Hz instability mode persists here, but its amplitude is only 65% of that at the bottom of combustor. Four perforated liner absorbers which are made of a liner of 3mm effective thickness and a 2.5cm deep cavity are installed on the side walls of the combustion chamber. The porosity of the liner is 1.6% and the liner surface is 60mm×80mm which only covers half of the area of the combustor vertical walls. Cross section of the air cavity is 85mm×114mm which is of the same size with the combustor vertical wall. These perforated liners are treated by the porous media region in CFD simulations. It is shown in Figure 75 that installation of these perforated liner absorbers is able to reduce the fluctuation magnitude of 480Hz instability mode by nearly 50% at the combustor exit and the proposed CFD method is able to represent the attenuation effect of these perforated liner absorbers.

Figure 76 provides similar noise attenuation effect of the same four perforated liner absorbers. However, a mean bias flow is injected through these perforated liners into the combustor. The average orifice Mach number and the temperature of the injected bias flow is $M_b = 0.015$ and $T = 320K$ respectively. Figure 76 shows that the noise reduction effect of these perforated liners in presence of the bias flow is

very similar to that under zero bias flow condition. This may be due to the fact that although the average bias flow is zero when the cavity is closed, local bias flow does exist in the liners due to the local pressure difference across combustor walls. And the noise attenuation effect due to these local bias flows is similar with the attenuation effect generated by the mean bias flow at $M_b = 0.015$.

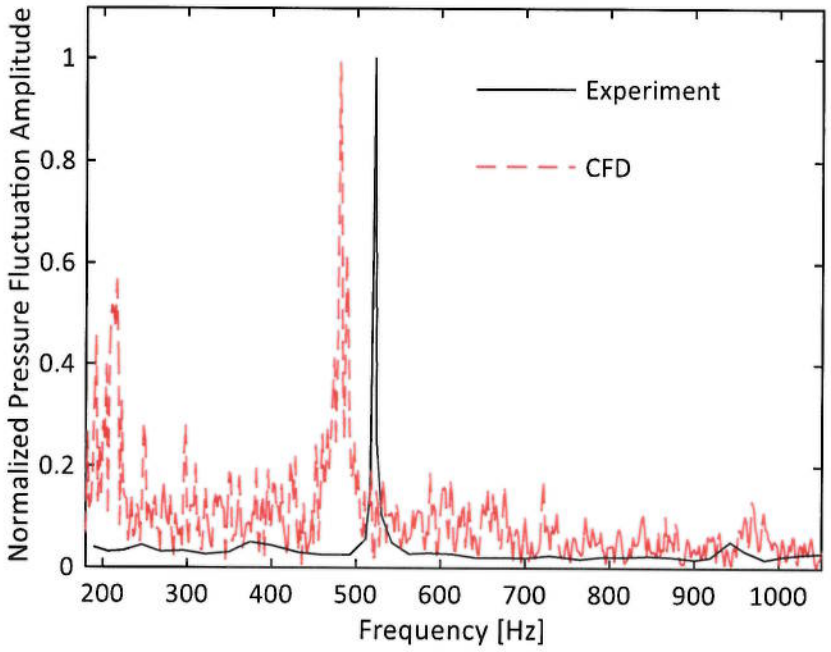

Figure 73 CFD and experimental comparison of normalized pressure fluctuation amplitude in the combustor

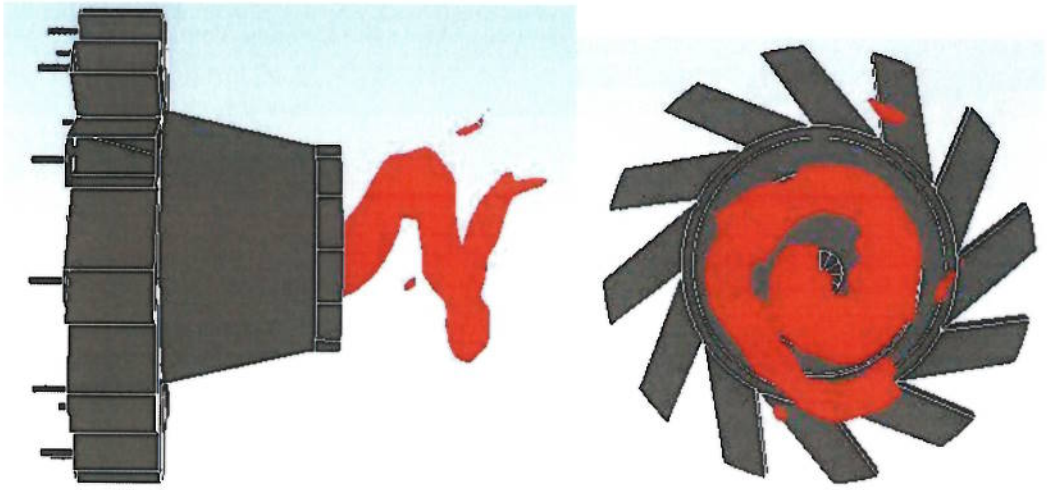

(a) (b)

Figure 74 Visualization of the 490 Hz PVC hydrodynamic instability at the exit of the swirler using an iso-surface of low pressure (p=-400Pa) (a) Side view (b) Top view

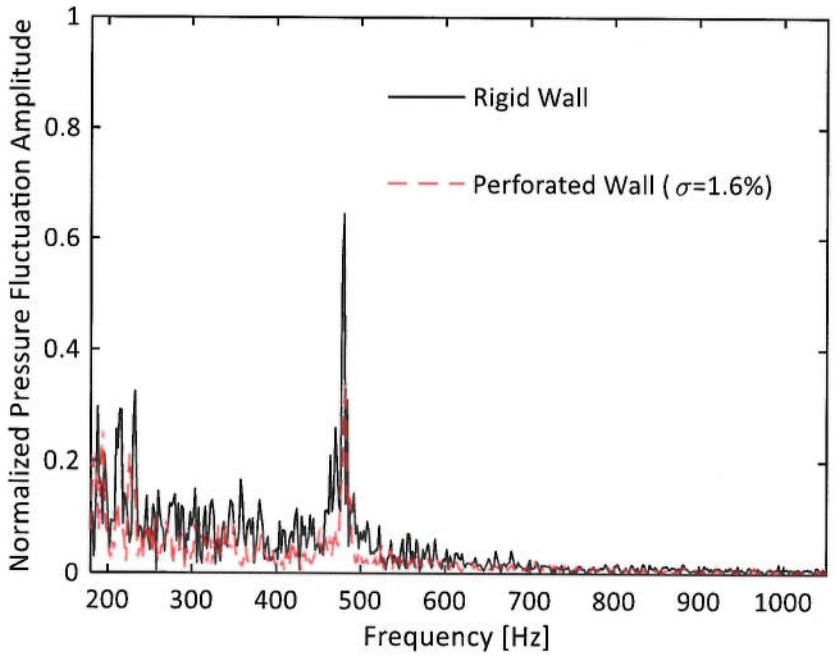

Figure 75 Comparison of normalized pressure fluctuation amplitude at the combustor exit with and without perforated liners under zero bias flow condition

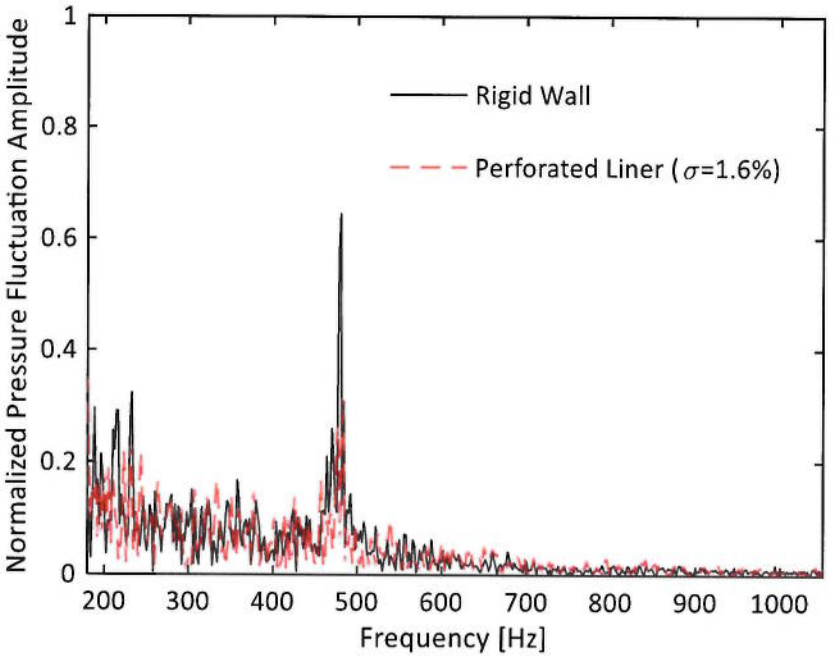

Figure 76 Comparison of normalized pressure fluctuation amplitude at the combustor exit with and without perforated liners under 5m/s bias flow condition

7.3.2 Reacting Flow

Figure 77 and Figure 78 compare the temperature contour in a vertical cross section of the combustor obtained by LES with and without cool bias flow injections. It can be seen that large eddy simulation is able to reflect the wrinkling of flame fronts due to turbulence/flame interactions. Cool bias flow of 450K is supressed into the combustion chamber and the bias flow mass flow rate is 1/10 of the primary air injection mass flow rate. As a consequence, the temperature of the flue gas is reduced from 1900-2000K to 1700-1800K and a lower temperature flow film (approximately 1200K) is formed near the combustor wall. NOx emission will also be noticeably reduced due to the lower reacting temperature.

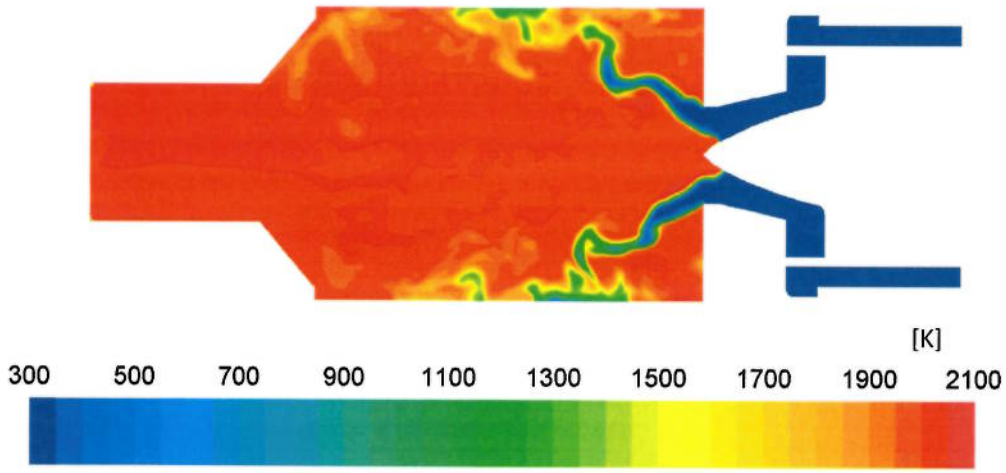

Figure 77 Temperature contour in The PRECCINSTA combustor acquired by LES method at t=0.2s

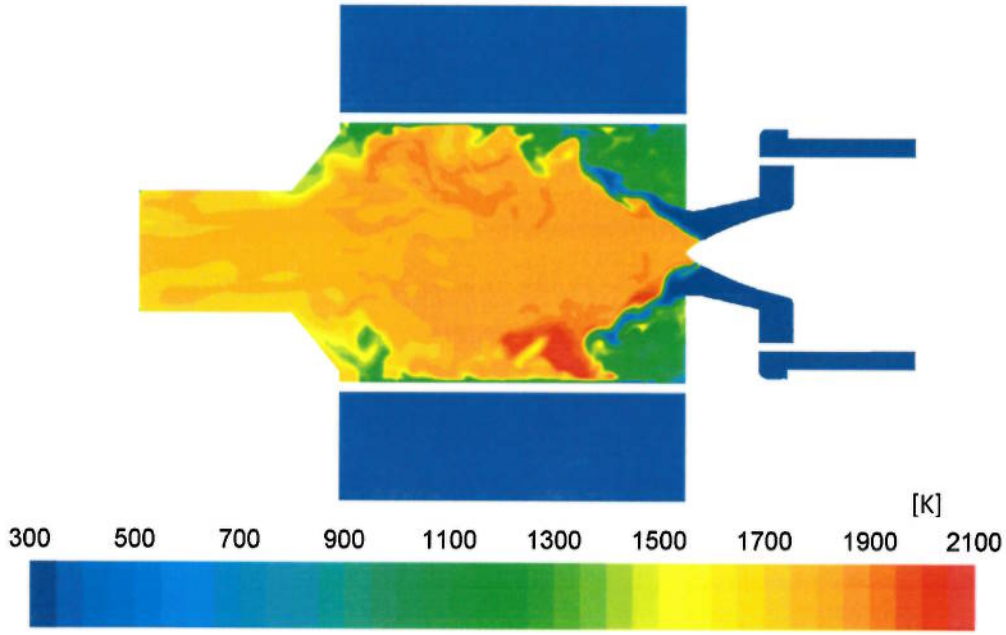

Figure 78 Temperature contour in The PRECCINSTA combustor with designed perforated liner absorber acquired by LES method at t=0.2s

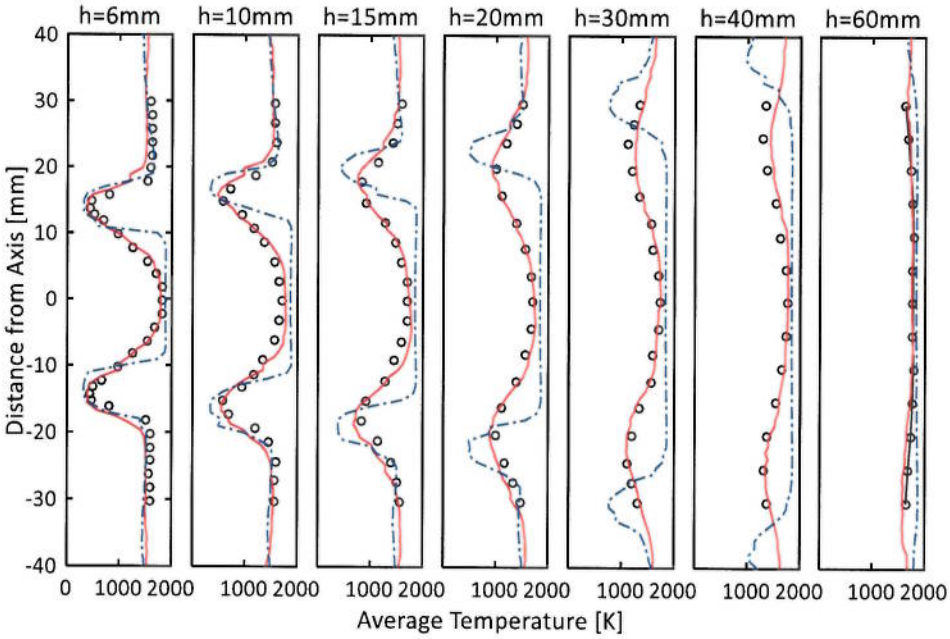

Figure 79 Mean temperature obtained by experiment (black dots), LES (red solid line) and RANS method (blue dash dot line)

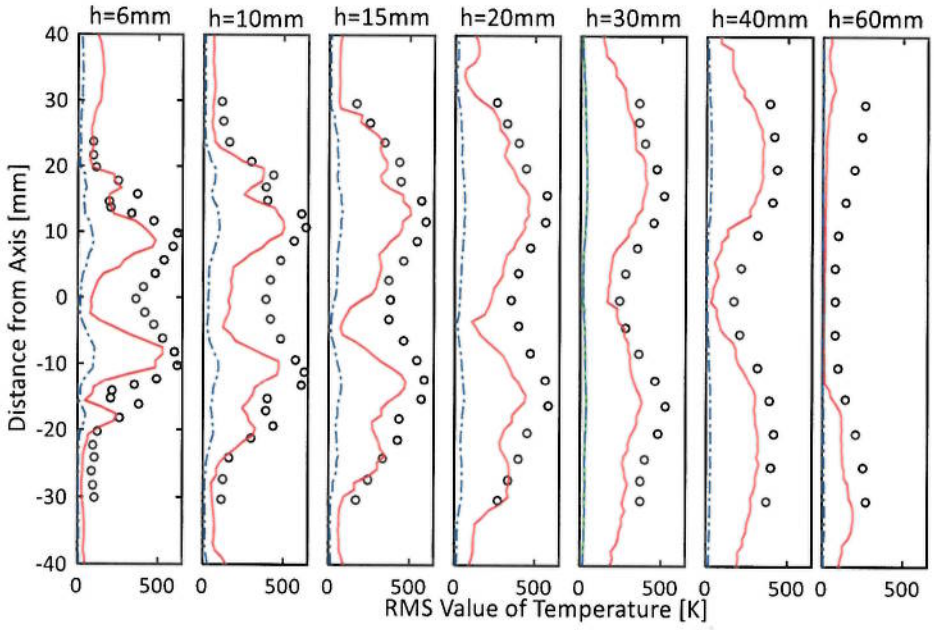

Figure 80 RMS value of temperature fluctuation obtained by experiment (black dots), LES (red solid line) and RANS method (blue dash dot line)

Figure 79 plots the mean temperature profiles at seven heights of the combustion chamber. It is shown that both LES and RANS methods are able to give reasonable prediction about the mean temperature values in those locations. However, LES and experimental results embrace a wider low temperature region in the temperature profiles due to the temperature averaging effect of the oscillating unburnt cool flow regions. Figure 80 indicates that RANS method losses the majority of flow unsteadiness and by contrast, LES generated results provide much closer agreement with experimental results. This suggests that LES is able to resolve the unsteady flow fields in the combustion chamber. Nevertheless, there also exist obvious discrepancies between LES and experimental results which can be caused by a number of sources of errors such as errors due to numerical solution schemes, errors in the sub-grid stress modelling and errors in chemical reaction modelling (Mahesh et al., 2004; Versteeg & Malalasekera, 2007; Garnier et al., 2009).

Figure 81 compares the instability modes captured in the experiments (Roux et al., 2005) and those by large eddy simulations in reacting flows. Experimental test captured two pressure oscillation modes at 300Hz and 570Hz in the combustor.

Large eddy simulations fail to capture the instability mode at 300Hz, but succeeded in getting a 500Hz instability mode. The finding of only one instability mode at 500Hz was also acquired by Roux et al. in their large eddy simulations (Roux et al., 2005; Franzelli et al., 2012). They argued that the inability of LES in capturing both instability modes is due to the absence of air inlet plenum from the calculation domain and the ill-defined acoustic impedance boundaries. In addition to their explanation, other sources of errors are possible as well: the upwind discretization schemes may perform badly in large eddy simulations (Mahesh et al., 2004); the fast and dramatic chemical reactions happens in sub-grid scale and modelling of such process may deteriorate the accuracy of sub-grid stress models (Pitsch, 2006). Despite the prediction errors about the instability modes, large eddy simulation successfully captures the combustion instability mode at 500Hz.

Figure 82 and Figure 83 illustrate how the addition of perforated liner absorbers is able to reduce the pressure fluctuation amplitude at the location 3cm behind the combustor exit. Four perforated liner absorbers which are made of a liner of 3.5mm effective thickness and are backed by 3.5cm deep cavity are installed on the side walls of the combustion chamber. The porosity of the liner is 1% and the liner surface is 60mm×80mm which only covers half of area of the combustor vertical walls. Cross section of the air cavity is 85mm×114mm which is of the same size with the combustor vertical wall. Figure 82 shows that sound attenuation effect by these four perforated liner absorbers is remarkable within 400Hz-600Hz around the design resonance frequency of those perforated liner absorbers and the 500Hz instability mode is well supressed without the mean bias flow injection.

The noise attenuation effect of these four perforated liner absorbers in the presence of mean bias flow is shown in Figure 83. Bias flow of 450K is injected into the combustor at the mass flow rate of 1/10 of the primary air flow rate. Porosity of liners is increased to 2% for a better attenuation effect in the presence of bias flow. Figure 83 displays that the instability mode 500Hz is effectively suppressed by the liner absorbers in the presence of bias flow. However, attenuation effect is not obvious at most other frequencies. This may suggest that the bias flow is not reducing the amplitude of the instability mode due to the attenuation effect of

perforated liner absorbers, it may prevent the occurrence of combustion instability however, by altering the flow dynamics in the combustor (Barbosa et al., 2009).

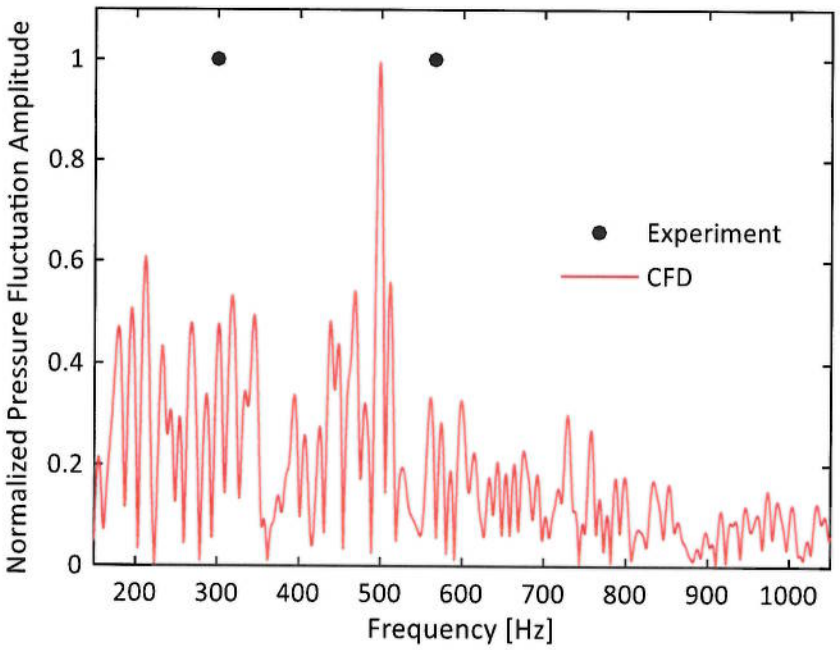

Figure 81 CFD and experimental comparison of normalized pressure fluctuation amplitude in the combustor

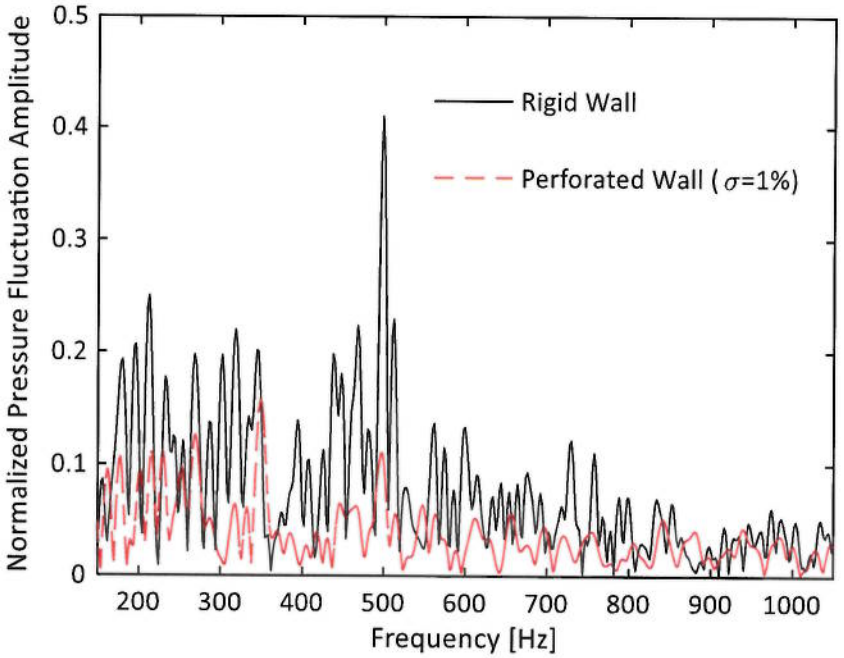

Figure 82 Comparison of normalized pressure fluctuation amplitude at the combustor exit with and without perforated liners under zero bias flow condition

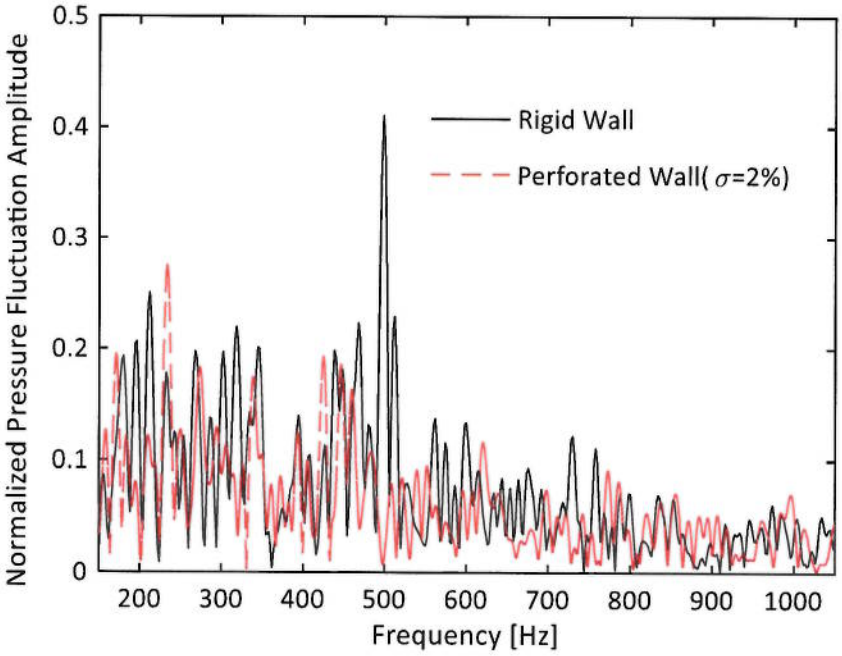

Figure 83 Comparison of normalized pressure fluctuation amplitude at the combustor exit with and without perforated liners under 5m/s bias flow condition

7.4 Summary

Large eddy simulations of flow and acoustic fields in the "PRECCINSTA" combustor are carried out and the numerical results are compared with those experimental results. Satisfactory solution for the mean flow field in both the non-reacting and reacting flow situations are achieved by RANS method and LES method. The unsteadiness strength of the swirling flows is also acquired with acceptable accuracy by LES method. However, unsteady RANS method tends to seriously underestimate the unsteadiness strength when it is applied to calculate self-excited transient flow dynamics and it cannot be applied in the study of combustion instability phenomenon.

Large eddy simulation is demonstrated to be able to capture the instability mode as a result of a precessing vortex core for cold flow conditions. However, LES method also embraces obvious errors in its prediction about pressure instability modes for reacting flow situations. Despite the error, large eddy simulation has successfully showed that the installation of perforated liner absorbers is able to reduce the amplitude of pressure instabilities. In addition, both the film cooling effect and the

noise attenuation effect of bias flow liners are successfully represented by treating perforated liners as porous media regions according to methods established in Chapter 3.

8. Conclusions and Perspectives

8.1 Summary and Conclusions

This thesis proposed a new CFD modelling strategy for noise attenuating gas turbine combustor perforated liners. The perforated combustor liner was treated as an equivalent homogenous porous media region and its acoustic attenuation effect was demonstrated to be representable by a porous media model. Application of this method would be able to significantly reduce the computational cost otherwise needed in resolving the large number of effusion cooling holes. Relevant properties of the equivalent porous media region such as the porosity, thickness and the flow resistance have been carefully defined according to the proposed methodologies. Structured hexahedral meshes were required within the porous media region and numerical discretization schemes were required to be with at least a second order numerical accuracy.

Comprehensive validations of the proposed CFD method have been achieved against both a number of well-established experiments and specifically designed experiments in the University of Hull. Effects of a number of flow and geometry factors on the acoustic properties of perforated liner absorbers were successfully reproduced. These factors included the porosity, the number of liners, the array of liners, liner thickness, sound signal incident angle, sound signal strength, bias flow speed, grazing flow speed, simultaneous bias/grazing flows, temperature of the flow, and acoustic reflection property of boundaries. The proposed CFD method was finally applied in large eddy simulations for the lab-scale combustor "PRECCINSTA" and the porous media model was demonstrated to be able to represent the attenuation effect of perforated combustor liners. A brief summary is provided below.

Porosity: Four perforated panel absorbers from the experiment by Lee and Kwon (2004) and three other panel absorbers experimentally investigated by University of Hull, Acoustic Research Centre were revisited by the proposed CFD method. Porosities of these plates ranged from 0.38% to 7.07%. CFD generated absorption

coefficient curves for these plates agreed very closely with those experimental curves both in terms of the resonance frequencies and the absorption bandwidth.

Multi-layer Panel Absorber: A second layer of perforated liner is often present in gas turbine engines in order to modulate the bias flow rate. A double-layer and a three-layer panel absorbers from the experiment by Lee and Kwon's (2004) were simulated. CFD generated results matched those experimental results very closely. In addition, two three-layer panel absorbers with reverse panel arrays were calculated by the CFD method and it was shown that the CFD method was able to reproduce the effect of panel arrays as well.

Signal Incidence Angle: Serial or parallel connection of a perforated liner absorber could significantly impact the acoustic attenuation effect of the liner absorber. The experiment by University of Hull where three perforated panels were incident by a grazing sound signal was numerically revisited. The proposed CFD method was able to yield acoustic attenuation properties for these three panel absorbers with satisfactory accuracy.

High Sound Pressure Level: The response to high sound pressure levels were numerically revisited for a perforated plate with a large porosity (7.6%) from Melling's work (1973) and an orifice plate with a small porosity (0.5%) from the experiment by Jing and Sun (2002). The experimental response of these two plates to high incident sound pressure levels were successfully reproduced by the proposed CFD method. It was found that plates with smaller porosities and smaller orifice tended to reach the non-linear absorption and attenuation saturation effect at lower sound pressure levels. The acoustic resistance increased linearly with the neck particle velocities at high sound pressure levels.

Bias Flow: Bias flow speed was claimed to the most determining flow factor for acoustic impedance of perforated liners (Rice, 1971; Lahiri, 2014). Three well-acknowledged experiments (Jing & Sun, 1999; Eldredge & Dowling, 2003; Bellucci et al., 2004) and the experiment by University of Hull were numerically repeated. The proposed CFD method managed to reproduce the experimental findings that bias flow of appropriate speed could significantly enhance the noise attenuation effect

of a perforated liner absorber but excessive bias flow could damage the attenuation effect on the other hand. CFD also found that acoustic resistance increased linearly with bias flow Mach number. In addition, the thickness of a liner was demonstrated to be able to affect the resonance frequency and absorption bandwidth of the liner absorber. The validation against the experiment by Eldredge and Dowling (2003) showed that the proposed CFD method was also able to represent the impact of acoustic boundary conditions on the attenuation effect of a liner absorber.

Grazing Flow: The porous media model was firstly demonstrated to be not able to represent the grazing flow induced resistance due to its inability in capturing the local neck flows. An empirical flow resistance term (Heidelberg et al., 1980; Syed et al., 2002) was thus accommodated into the porous media model to remedy this issue. Grazing flow effect on the acoustic impedance of three perforated plates from the experiment by Jing et al. (2001) was then successfully reproduced by this method. It was shown that orifices of larger size were subjected to larger impact of grazing flow than those of smaller size.

Simultaneous Bias/Grazing Flow: Simultaneous flow conditions were treated as bias flow dominant region and grazing flow dominant region according to the relative magnitude of their induced flow resistance. The flow resistance of porous media region in grazing flow dominant regime was supplemented by the difference between grazing flow induced resistance and the bias flow induced resistance. Grazing flow induced resistance was ignored in the bias flow dominant regime. This CFD method has successfully generated satisfactory acoustic impedance results for three perforated panels from Sun's experiment (Sun et al., 2002).

Application in "PRECCINSTA" Combustor: Swirling cold flow field and reacting hot flow field in the "PRECCINSTA" combustor were calculated by large eddy simulations. Both mean flow variables and fluctuation magnitudes of unsteady statistics were acquired with reasonable accuracy by large eddy simulations. A pressure fluctuation mode due to precessing vortex core was captured by large eddy simulations in cold flow situation and the frequency was in close agreement with experimental result. However, large eddy simulations embraced errors in the

prediction about combustion instability modes in reacting flows. Experimental results gave two instability modes at 300Hz and 570Hz respectively while large eddy simulations was only able to capture one instability mode at 500Hz. Despite the error, large eddy simulations were continued to simulate the situations where the combustor wall was mounted with four perforated liner absorbers. The proposed porous media model was applied to represent these perforated combustor liners. It was shown that perforated liner absorbers did exhibit noise attenuation effect and the noise attenuation effect was obtainable by treating perforated liner as a porous media region following the proposed CFD method.

8.2 Outlook and Perspectives

Perforated gas turbine combustor liner has long been a complex issue from simulation point of view. Resolving so large number of small holes requires excessive computational time. Ignoring the bias flow through perforated liners will lead to prediction discrepancy in terms of the temperature of flue gas and the flow dynamics in the combustor. Treating the perorated wall as an open flow inlet will result in unphysical flow field due to the interaction between internal flow and the open flow inlet. A steady state homogenous flow boundary condition is able to obtain the transverse mass flow rate due to a steady pressure drop by defining the discharge coefficient of the liner. However, it is not able to resolve the transient acoustic field near perforated liners and thus is not able to obtain the acoustic attenuation effect of perforated liners.

The currently proposed methodology of applying the porous media model to represent the perforated combustor liners is able to acquire the transverse mass flow rate under a certain pressure drop by numerically resolving bias flow resistance. It is also capable of solving for transient acoustic phenomenon and the acoustic effect of perforated liners in transient CFD calculations. In addition, the amount of computational time will be significantly reduced compared with traditional CFD strategy of resolving hundreds or even thousands of small cooling holes. Last but not least, CFD method has unique advantage over the lengthy case by case experimental investigations that it is able to directly resolve the acoustical

impact of surrounding boundaries, the impact of the angle and strength of incident signals and the impact of relative size of the liner to the combustor. The current CFD modelling strategy of perforated liners is therefore time-saving and economically beneficial and it is a highly feasible approach to be applied in the industry design of noise attenuating perforated liners.

However, there are limitations related to the homogenous porous media model. For example, physical velocity in the liner region, non-linear effect due to high sound pressure levels and inertial effect due to the bias flow are numerically resolvable by the porous media model itself. On the other hand, perforation end correction length and the grazing flow induced resistance are beyond the calculation capability of the porous media model. As a consequence, the current way of defining a porous media region for the representation of a perforated liner still requires empirical input to take into account the acoustic radiation effect and the grazing flow induced resistance.

These drawbacks are predominantly due to the structure homogeneity assumption underlying the porous media model. Therefore, any attempt to optimize the porous media model to take into account inhomogeneous effect requires modification to this underlying homogeneity presumption. On the other hand, the structure homogeneity assumption by ignoring geometry details is also the underlying reason why computational time reduction is achievable. Therefore, change of the structure homogeneity assumption for the porous media model to be able to represent inhomogeneous effects such as perforation end correction length and grazing flow induced resistance is unpromising. These factors due to flow and structure inhomogeneity can only be taken into consideration by empirical methods at current stage of this work.

References

Ahuji, K. K. & Gaeta Jr, R. J. (2000) *Active control of liner impedance by varying perforate orifice geometry*. Atlanta,USA: NASA-GTRI-A5004/2000-1. Available online: https://ntrs.nasa.gov/search.jsp?R=20000067667 [Accessed 01/10/2016].

Albouze, G. (2009) *Simulation aux grandes échelles des écoulements réactifs non prémélangés*. Ph.D Thesis. Institut National Polytechnique de Toulouse.

Anderson, J. D. & Wendt, J. (1995) *Computational fluid dynamics, 206*.Springer.

Andreini, A., Facchini, B., Ferrari, L., Lenzi, G., Simonetti, F. & Peschiulli, A. (2012) Experimental investigation on effusion liner geometries for aero-engine combustors: evaluation of global acoustic parameters, *ASME Turbo Expo 2012: Turbine Technical Conference and Exposition*. Copenhagen, Denmark, 2012. American Society of Mechanical Engineers.

Annaswamy, A. M. & Ghoniem, A. F. (2002) Active control of combustion instability: Theory and practice. *IEEE control systems*, 22(6), 37-54.

Antohe, B. V. & Lage, J. L. (1997) A general two-equation macroscopic turbulence model for incompressible flow in porous media. *International Journal of Heat and Mass Transfer*, 40(13), 3013-3024.

Atalla, N. & Sgard, F. (2007) Modeling of perforated plates and screens using rigid frame porous models. *Journal of Sound and Vibration*, 303(1), 195-208.

Barbosa, S., Scouflaire, P. & Ducruix, S. (2009) Time resolved flowfield, flame structure and acoustic characterization of a staged multi-injection burner. *Proceedings of the Combustion Institute*, 32(2), 2965-2972.

Barrere, M. & Williams, F. A. (1969) Comparison of combustion instabilities found in various types of combustion chambers. *Symposium (International) on Combustion*, 12, 169-181.

Bauer, A. B. (1977) Impedance theory and measurements on porous acoustic liners. *Journal of Aircraft*, 14(8), 720-728.

Bellucci, V., Flohr, P. & Paschereit, C. O. (2004) Numerical and Experimental Study of Acoustic Damping Generated by Perforated Screens. *AIAA Journal*, 42(8), 1543-1549.

Bellucci, V., Paschereit, C. O., Flohr, P. & Magni, F. (2001) On the use of Helmholtz resonators for damping acoustic pulsations in industrial gas turbines, *ASME Turbo Expo 2001: Power for Land, Sea, and Air*. Louisiana, USA, 2001. American Society of Mechanical Engineers.

Benhamadouche, S. & Laurence, D. (2003) LES, coarse LES, and transient RANS comparisons on the flow across a tube bundle. *International Journal of Heat and Fluid Flow*, 24(4), 470-479.

Betts, J. F. (2000) *Experiments and impedance modeling of liners including the effect of bias flow*. Ph.D Thesis. Virginia Tech.

Blokhintsev, D. I. (1956) *Acoustics of a Nonhomogeneous Moving Medium*.National Advisory Committee for Aeronautics Washington, DC.

Bloxsidge, G. J., Dowling, A. P. & Langhorne, P. J. (1988) Reheat buzz: an acoustically coupled combustion instability. Part 2. Theory. *Journal of Fluid Mechanics*, 193, 445-473.

Bodén, H. & Kabral, R. (2015) The effect of high temperatures and grazing flow on the acoustic properties of liners, *EuroNoise2015*. Maastricht, Belgium, 31 May-3 June.

Bolt, R. H., Labate, S. & Ingård, U. (1949) The acoustic reactance of small circular orifices. *The Journal of the Acoustical Society of America*, 21(2), 94-97.

Bothien, M. R., Moeck, J. P. & Paschereit, C. O. (2008) Active control of the acoustic boundary conditions of combustion test rigs. *Journal of Sound and Vibration*, 318(4), 678-701.

Boudier, G., Gicquel, L. Y. M., Poinsot, T., Bissieres, D. & Bérat, C. (2007) Comparison of LES, RANS and experiments in an aeronautical gas turbine combustion chamber. *Proceedings of the Combustion Institute*, 31(2), 3075-3082.

Bulat, G., Jones, W. P. & Marquis, A. J. (2014) NO and CO formation in an industrial gas-turbine combustion chamber using LES with the Eulerian sub-grid PDF method. *Combustion and Flame*, 161(7), 1804-1825.

Candel, S. (2002) Combustion dynamics and control: Progress and challenges. *Proceedings of the Combustion Institute*, 29(1), 1-28.

Candel, S. M. (1992) Combustion instabilities coupled by pressure waves and their active control. *Symposium (International) on Combustion*, 24(1), 1277-1296.

Champoux, Y. & Allard, J. F. (1991) Dynamic tortuosity and bulk modulus in air - saturated porous media. *Journal of Applied Physics*, 70(4), 1975-1979.

Chanaud, R. C. (1994) Effects of geometry on the resonance frequency of Helmholtz resonators. *Journal of Sound and Vibration*, 178(3), 337-348.

Chu, W. T. (1986) Transfer function technique for impedance and absorption measurements in an impedance tube using a single microphone. *The Journal of the Acoustical Society of America*, 80(2), 555-560.

Chung, J. Y. & Blaser, D. A. (1980) Transfer function method of measuring in - duct acoustic properties. I. Theory. *The Journal of the Acoustical Society of America*, 68(3), 907-913.

Cohen, J. M. & Banaszuk, A. (2003) Factors affecting the control of unstable combustors. *Journal of Propulsion and Power*, 19(5), 811-821.

Cook, A. W. & Riley, J. J. (1994) A subgrid model for equilibrium chemistry in turbulent flows. *Physics of Fluids (1994-present)*, 6(8), 2868-2870.

Crandall, I. B. (1954) *Theory of vibrating systems and sound*.D. Van Nostrand Company.

Culick, F. E. & Kuentzmann, P. (2006) *Unsteady motions in combustion chambers for propulsion systems*.NATO Research and Technology Organization.

Culick, F. E. C. & Yang, V. (1995) Overview of combustion instabilities in liquid-propellant rocket engines. *Liquid Rocket Engine Combustion Instability*, 169, 3-37.

Cummings, A. (1984) Acoustic nonlinearities and power losses at orifices. *AIAA Journal*, 22(6), 786-792.

Cummings, A. (1986) Transient and multiple frequency sound transmission through perforated plates at high amplitude. *The Journal of the Acoustical Society of America*, 79(4), 942-951.

Cummings, A. & Eversman, W. (1983) High amplitude acoustic transmission through duct terminations: Theory. *Journal of Sound and Vibration*, 91(4), 503-518.

Dannenberg, R. E., Gambucci, B. J. & Weiberg, J. A. (1956) *Perforated Sheets as a Porous Material for Distributed Suction and Injection*. Washington: NACA.

Dassé, J., Mendez, S. & Nicoud, F. (2008) Large-eddy simulation of the acoustic response of a perforated plate, *14th AIAA/CEAS Aeroacoustics Conference (29th AIAA Aeroacoustics Conference)*. Vancouver,Canada, 05 May - 07 May 2008.

Dean, L. W. (1975) *Coupling of Helmholtz resonators to improve acoustic liners for turbofan engines at low frequency*. East Hartford, CT, United States: NASA. Available online: https://ntrs.nasa.gov/search.jsp?R=19760014122 [Accessed 5/07/2016].

Dean, P. D. (1974) An in situ method of wall acoustic impedance measurement in flow ducts. *Journal of Sound and Vibration*, 34(1), 97-IN6.

Dean, P. D. & Tester, B. J. (1975) *Duct wall impedance control as an advanced concept for acoustic impression*. Marietta, GA, United States: NASA. Available online: https://ntrs.nasa.gov/search.jsp?R=19760014122 [Accessed 8/11/2016].

Dickey, N. S., Selamet, A. & Ciray, M. S. (2001) An experimental study of the impedance of perforated plates with grazing flow. *The Journal of the Acoustical Society of America*, 110(5), 2360-2370.

Dowling, A. P. & Morgans, A. S. (2005) Feedback control of combustion oscillations. *Annual Review of Fluid Mechanics*, 37, 151-182.

Dowling, A. P. & Stow, S. R. (2003) Acoustic analysis of gas turbine combustors. *Journal of Propulsion and Power*, 19(5), 751-764.

Eckert, E. R. G. (1984) Analysis of film cooling and full-coverage film cooling of gas turbine blades. *Journal of Engineering for Gas Turbines and Power*, 106(1), 206-213.

Eldredge, J. D. & Dowling, A. P. (2003) The absorption of axial acoustic waves by a perforated liner with bias flow. *Journal of Fluid Mechanics*, 485, 307-335.

Eliaz, N., Shemesh, G. & Latanision, R. M. (2002) Hot corrosion in gas turbine components. *Engineering Failure Analysis*, 9(1), 31-43.

Elnady, T. (2004) *Modelling and characterization of Perforates in Lined Ducts and Mufflers*. Ph.D Thesis KTH Royal Institute of Technology in Stockholm. Available online: http://www.diva-portal.org/smash/get/diva2:9676/FULLTEXT01.pdf [Accessed 04/08/2016].

Elnady, T. & Boden, H. (2003) On semi-empirical liner impedance modeling with grazing flow, *9th AIAA/CEAS Aeroacoustics Conference and Exhibit.* South Carolina, 12 May - 14 May 2003. American Institute of Aeronautics and Astronautics.

Elnady, T., Bodén, H. & Kontio, T. (2004) Impedance of SDOF perforated liners at high temperatures, *10th AIAA/CEAS Aeroacoustics Conference*. Manchester, GREAT BRITAIN, 10 May - 12 May 2004. American Institute of Aeronautics and Astronautics.

Erlebacher, G., Hussaini, M. Y., Speziale, C. G. & Zang, T. A. (1992) Toward the large-eddy simulation of compressible turbulent flows. *Journal of Fluid Mechanics*, 238, 155-185.

Fan, W. & Guo, L.-X. (2016) An Investigation of Acoustic Attenuation Performance of Silencers with Mean Flow Based on Three-Dimensional Numerical Simulation. *Shock and Vibration*, 2016.

Farmer, G., Brown, D. D. & Rutherford, M. E. (2003) Preferential multihole combustor liner. US: Google Patents-US6655149.

Fiorina, B., Vicquelin, R., Auzillon, P., Darabiha, N., Gicquel, O. & Veynante, D. (2010) A filtered tabulated chemistry model for LES of premixed combustion. *Combustion and Flame*, 157(3), 465-475.

Fluent, A. (2009) 12.0 User's guide. *User Inputs for Porous Media*, 6.

Fok & Brocklesby, M. W. (1941) Theoretical study of the conductance of a circular hole in a partition across a tube. *Doklady Akademii Nauk SSSR*, 31(9), 875-882.

Franzelli, B., Riber, E., Gicquel, L. Y. M. & Poinsot, T. (2012) Large eddy simulation of combustion instabilities in a lean partially premixed swirled flame. *Combustion and Flame*, 159(2), 621-637.

Gaeta, R. J. & Ahuja, K. K. (2016) Effect of orifice shape on acoustic impedance. *International Journal of Aeroacoustics*, 15(4-5), 474 - 495.

Garnier, E., Adams, N. & Sagaut, P. (2009) *Large eddy simulation for compressible flows*.Springer Science & Business Media.

Gerke, H. H. & Genuchten, M. T. V. (1993) A dual-porosity model for simulating the preferential movement of water and solutes in structured porous media. *Water Resources Research*, 29(2), 305-319.

Germano, M., Piomelli, U., Moin, P. & Cabot, W. H. (1991) A dynamic subgrid - scale eddy viscosity model. *Physics of Fluids A: Fluid Dynamics (1989-1993)*, 3(7), 1760-1765.

Ghosal, S. & Moin, P. (1995) The basic equations for the large eddy simulation of turbulent flows in complex geometry. *Journal of Computational Physics*, 118(1), 24-37.

Gibson, M. M. & Launder, B. E. (1978) Ground effects on pressure fluctuations in the atmospheric boundary layer. *Journal of Fluid Mechanics*, 86(03), 491-511.

Gicquel, L. Y. M., Staffelbach, G. & Poinsot, T. (2012) Large eddy simulations of gaseous flames in gas turbine combustion chambers. *Progress in Energy and Combustion Science*, 38(6), 782-817.

Gleeson, B. (2006) Thermal barrier coatings for aeroengine applications. *Journal of Propulsion and Power*, 22(2), 375-383.

Goy, C. J., James, S. R. & Rea, S. (2005) Monitoring combustion instabilities: E. ON UK's experience. *Progress in Astronautics and Aeronautics*, 210, 163.

Grace, S. M., Horan, K. P. & Howe, M. S. (1998) The influence of shape on the Rayleigh conductivity of a wall aperture in the presence of grazing flow. *Journal of Fluids and Structures*, 12(3), 335-351.

Hanks, R. W. (1963) The laminar - turbulent transition for flow in pipes, concentric annuli, and parallel plates. *AIChE Journal*, 9(1), 45-48.

Heidelberg, L. J., Rice, E. J. & Homyak, L. (1980) *Experimental evaluation of a spinning-mode acoustic-treatment design concept for aircraft inlets*. Cleveland, United States: NASA-TP-1613, E.-. Available online: https://ntrs.nasa.gov/search.jsp?R=19800012838 [Accessed 5/09/2016].

Heuwinkel, C., Enghardt, L. & Röhle, I. (2007) Experimental investigation of the acoustic damping of perforated liners with bias flow, *13th AIAA/CEAS Aeroacoustics Conference (28th AIAA Aeroacoustics Conference)*. Rome, Italy, 21 May- 23 May 2007. American Institute of Aeronautics and Astronautics.

Heuwinkel, C., Pardowitz, B., Bake, F., Röhle, I. & Enghardt, L. (2009) On the excitation of a zero mass flow liner for acoustic damping, *15th AIAA/CEAS Aeroacoustics Conference (30th AIAA Aeroacoustics Conference)*. Florida, USA, 2009. The American Institute of Aeronautics and Astronautics.

Houston, B., Wang, J., Qin, Q. & Rubini, P. (2015a) Experimental and numerical investigation of Helmholtz resonators and perforated liners as attenuation devices in industrial gas turbine combustors. *Fuel*, 151, 31-39.

Houston, B., Wang, J., Rubini, P. & Qin, Q. (2015b) *Experimental study of the noise attenuation effect of side branched distributed Helmholtz resonators*. University of Hull, Acoustic Research Centre.

Howe, M. S. (1979) On the theory of unsteady high Reynolds number flow through a circular aperture. *Proceedings of the Royal Society of London. Series A, Mathematical and Physical Sciences*, 366, 205-223.

Howe, M. S. (1998) *Acoustics of fluid-structure interactions*.Cambridge university press.

Huang, H. & Ayoub, J. A. (2008) Applicability of the Forchheimer equation for non-Darcy flow in porous media. *SPE Journal*, 13(01), 112-122.

Huang, Y. & Yang, V. (2009) Dynamics and stability of lean-premixed swirl-stabilized combustion. *Progress in Energy and Combustion Science*, 35(4), 293-364.

Hughes, I. J. & Dowling, A. P. (1990) The absorption of sound by perforated linings. *Journal of Fluid Mechanics*, 218, 299-335.

Ingard, U. (1953) On the theory and design of acoustic resonators. *The Journal of the Acoustical Society of America*, 25(6), 1037-1061.

Ingard, U. (1959) Attenuation and regeneration of sound in ducts and jet diffusers. *The Journal of the Acoustical Society of America*, 31(9), 1202-1212.

Ingard, U. & Ising, H. (1967) Acoustic nonlinearity of an orifice. *The journal of the Acoustical Society of America*, 42(1), 6-17.

Jing, X. & Sun, X. (1999) Experimental investigations of perforated liners with bias flow. *The Journal of the Acoustical Society of America*, 106(5), 2436-2441.

Jing, X. & Sun, X. (2000) Effect of plate thickness on impedance of perforated plates with bias flow. *AIAA Journal*, 38(9), 1573-1578.

Jing, X. & Sun, X. (2002) Sound-excited flow and acoustic nonlinearity at an orifice. *Physics of Fluids (1994-present)*, 14(1), 268-276.

Jing, X., Sun, X., Wu, J. & Meng, K. (2001) Effect of grazing flow on the acoustic impedance of an orifice. *AIAA Journal*, 39(8), 1478-1484.

Johnson, D. L., Koplik, J. & Dashen, R. (1987) Theory of dynamic permeability and tortuosity in fluid-saturated porous media. *Journal of fluid mechanics*, 176, 379-402.

Jones, M. G., Parrott, T. L. & Watson, W. R. (2003) Comparison of acoustic impedance eduction techniques for locally-reacting liners. *AIAA paper*, 3306, 2003.

Jones, M. G., Tracy, M. B., Watson, W. R. & Parrott, T. L. (2002) Effects of liner geometry on acoustic impedance. *AIAA Paper*, 2446, 2002.

Jones, W. P. & Whitelaw, J. H. (1982) Calculation methods for reacting turbulent flows: a review. *Combustion and flame*, 48, 1-26.

Jourdain, G. & Eriksson, L.-E. (2014) Numerical validation of a time domain perforated plate model with nonlinear and inertial effects. *Journal of Computational Acoustics*, 22(04), 1450009.

Jung, S. S., Kim, Y. T., Lee, D. H., Kim, H. C., Cho, S. I. & Lee, J. K. (2007) Sound absorption of micro-perforated panel. *JOURNAL-KOREAN PHYSICAL SOCIETY*, 50(4), 1044.

Kaji, S., Hiramoto, M. & Okazaki, T. (1984) Acoustic characteristics of orifice holes exposed to grazing flow. *Bulletin of JSME*, 27(233), 2388-2396.

Kelsall, G. & Troger, C. (2004) Prediction and control of combustion instabilities in industrial gas turbines. *Applied Thermal Engineering*, 24(11), 1571-1582.

Kerswell, R. R. (2005) Recent progress in understanding the transition to turbulence in a pipe. *Nonlinearity*, 18(6), R17.

Kinsler, L. E., Frey, A. R., Coppens, A. B. & Sanders, J. V. (1999) Fundamentals of acoustics. *Fundamentals of Acoustics, 4th Edition, by Lawrence E. Kinsler, Austin R. Frey, Alan B. Coppens, James V. Sanders, pp. 560. ISBN 0-471-84789-5. Wiley-VCH, December 1999.*, 560.

Kirby, R. & Cummings, A. (1998) The impedance of perforated plates subjected to grazing gas flow and backed by porous media. *Journal of Sound and Vibration*, 217(4), 619-636.

Kolodzie, P. A. & Van Winkle, M. (1957) Discharge coefficients through perforated plates. *AIChE Journal*, 3(3), 305-312.

Kooi, J. W. & Sarin, S. L. (1981) An experimental study of the acoustic impedance of Helmholtz resonator arrays under a turbulent boundary layer, *7th Aeroacoustics*

Conference. Palo Alto,CA,U.S.A., 5 Oct -7 Oct 1981. American Institute of Aeronautics and Astronautics.

Krüger, J. & Quickert, M. (1997) Determination of acoustic absorber parameters in impedance tubes. *Applied Acoustics*, 50(1), 79-89.

Kuttruff, H. (2007) *Acoustics: an introduction*.CRC Press.

Lahiri, C. (2014) *Acoustic performance of bias flow liners in gas turbine combustors*. Ph.D Thesis Technische Universität Berlin. Available online: http://dx.doi.org/10.14279/depositonce-4270 [Accessed 05/1/2016].

Lartigue, G., Meier, U. & Bérat, C. (2004) Experimental and numerical investigation of self-excited combustion oscillations in a scaled gas turbine combustor. *Applied Thermal Engineering*, 24(11), 1583-1592.

Launder, B. E. & Spalding, D. B. (1972) *Lectures in mathematical models of turbulence*. London; New York: Academic press.

Laurens, S., Tordeux, S., Bendali, A., Fares, M. & Kotiuga, P. R. (2013) Lower and upper bounds for the Rayleigh conductivity of a perforated plate. *ESAIM: Mathematical Modelling and Numerical Analysis*, 47(6), 1691-1712.

Lee, D. H. & Kwon, Y. P. (2004) Estimation of the absorption performance of multiple layer perforated panel systems by transfer matrix method. *Journal of sound and vibration*, 278(4), 847-860.

Lee, S.-H. & Ih, J.-G. (2003) Empirical model of the acoustic impedance of a circular orifice in grazing mean flow. *The Journal of the Acoustical Society of America*, 114(1), 98-113.

Lee, S.-H., Ih, J.-G. & Peat, K. S. (2007) A model of acoustic impedance of perforated plates with bias flow considering the interaction effect. *Journal of Sound and Vibration*, 303(3), 741-752.

Lefebvre, A. H. B., Dilip R. (2010) *Gas turbine combustion: Alternative Fuels and Emissions*.CRC press.

Li, G. & Mechefske, C. K. (2010) A comprehensive experimental study of micro-perforated panel acoustic absorbers in MRI scanners. *Magnetic Resonance Materials in Physics, Biology and Medicine*, 23(3), 177-185.

Lieuwen, T., Neumeier, Y. & Zinn, B. T. (1998) The role of unmixedness and chemical kinetics in driving combustion instabilities in lean premixed combustors. *Combustion Science and Technology*, 135(1-6), 193-211.

Lieuwen, T. C. (2002) Experimental investigation of limit-cycle oscillations in an unstable gas turbine combustor. *Journal of Propulsion and Power*, 18(1), 61-67.

Lieuwen, T. C. & Yang, V. (2005) *Combustion instabilities in gas turbine engines(operational experience, fundamental mechanisms and modeling)*. Reston, USA: American Institute of Aeronautics and Astronautics.

Lieuwen, T. C. & Yang, V. (2013) *Gas turbine emissions, 38*. USA: Cambridge University Press.

Lilly, D. K. (1992) A proposed modification of the Germano subgrid - scale closure method. *Physics of Fluids A: Fluid Dynamics (1989-1993)*, 4(3), 633-635.

Liu, C. & Ji, Z. (2014) Computational fluid dynamics-based numerical analysis of acoustic attenuation and flow resistance characteristics of perforated tube silencers. *Journal of Vibration and Acoustics*, 136(2), 021006.

Liu, J. (2011) *Advanced studies on series impedance in waveguides with an emphasis on source and transfer impedance*. Ph.D Thesis University of Kentucky.

Liu, J. & Herrin, D. W. (2010) Enhancing micro-perforated panel attenuation by partitioning the adjoining cavity. *Applied Acoustics*, 71(2), 120-127.

Luong, T., Howe, M. S. & McGowan, R. S. (2005) On the Rayleigh conductivity of a bias-flow aperture. *Journal of Fluids and Structures*, 21(8), 769-778.

Maa, D.-Y. (1996) Microperforated panel at high sound intensity [J]. *Acta Acustica*, 1.

Maa, D.-Y. (1998) Potential of microperforated panel absorber. *the Journal of the Acoustical Society of America*, 104(5), 2861-2866.

Macdonald, I. F., El-Sayed, M. S., Mow, K. & Dullien, F. A. L. (1979) Flow through porous media-the Ergun equation revisited. *Industrial & Engineering Chemistry Fundamentals*, 18(3), 199-208.

MacManus, D. G. & Doran, D. S. (2008) Passive control of transonic cavity flow. *Journal of Fluids Engineering*, 130(6), 064501-1-064501-4.

Mahesh, K., Constantinescu, G. & Moin, P. (2004) A numerical method for large-eddy simulation in complex geometries. *Journal of Computational Physics*, 197(1), 215-240.

Malmary, C., Carbonne, S., Auregan, Y. & Pagneux, V. (2001) Acoustic impedance measurement with grazing flow, *7th AIAA/CEAS Aeroacoustics Conference and Exhibit*. Maastricht,Netherlands, 28 May - 30 May 2001. The American Institute of Aeronautics and Astronautics.

Mazdeh, A. (2012) *Damping parameter study of a perforated plate with bias flow*. Ph.D Thesis University of Dayton.

McAuliffe, C. E. (1950) *The influence of high speed air flow on the behavior of acoustical elements*. Msc Thesis Massachusetts Institute of Technology.

McManus, K. R., Poinsot, T. & Candel, S. M. (1993) A review of active control of combustion instabilities. *Progress in Energy and Combustion Science*, 19(1), 1-29.

Medeiros, A. A. (2015) *On the modelling and characterization of acoustic liners under grazing flow*. MEng. Thesis Universidade Federal de Santa Catarina.

Meier, W., Weigand, P., Duan, X. R. & Giezendanner-Thoben, R. (2007) Detailed characterization of the dynamics of thermoacoustic pulsations in a lean premixed swirl flame. *Combustion and Flame*, 150(1), 2-26.

Melling, T. H. (1973) The acoustic impedance of perforates at medium and high sound pressure levels. *Journel of Sound and Vibration*, 29, 1-65.

Mendez, S. & Eldredge, J. D. (2009) Acoustic modeling of perforated plates with bias flow for large-eddy simulations. *Journal of Computational Physics*, 228(13), 4757-4772.

Mendez, S. & Nicoud, F. (2008) Adiabatic homogeneous model for flow around a multiperforated plate. *AIAA Journal*, 46(10), 2623-2633.

Mercier, R., Moureau, V., Veynante, D. & Fiorina, B. (2015) LES of turbulent combustion: On the consistency between flame and flow filter scales. *Proceedings of the Combustion Institute*, 35(2), 1359-1366.

Miasa, I. M., Okuma, M., Kishimoto, G. & Nakahara, T. (2007) An experimental study of a multi-size microperforated panel absorber. *Journal of System Design and Dynamics*, 1(2), 331-339.

Moureau, V., Domingo, P. & Vervisch, L. (2011) From Large-Eddy Simulation to Direct Numerical Simulation of a lean premixed swirl flame: Filtered laminar flame-PDF modeling. *Combustion and Flame*, 158(7), 1340-1357.

Mualem, Y. (1976) A new model for predicting the hydraulic conductivity of unsaturated porous media. *Water Resources Research*, 12(3), 513-522.

Nicoud, F. & Ducros, F. (1999) Subgrid-scale stress modelling based on the square of the velocity gradient tensor. *Flow, Turbulence and Combustion*, 62(3), 183-200.

Noiray, N., Durox, D., Schuller, T. & Candel, S. (2007) Passive control of combustion instabilities involving premixed flames anchored on perforated plates. *Proceedings of the Combustion Institute*, 31(1), 1283-1290.

Oldfield, R. G. (2006) *Improved membrane absorbers*. Msc. Thesis The University of Salford.

Padture, N. P., Gell, M. & Jordan, E. H. (2002) Thermal barrier coatings for gas-turbine engine applications. *Science*, 296(5566), 280-284.

Paschereit, C. O., Gutmark, E. & Weisenstein, W. (1998) Control of thermoacoustic instabilities and emissions in an industrial-type gas-turbine combustor. *Symposium (International) on Combustion*, 27(2), 1817-1824.

Pierce, A. D. (1981) *Acoustics: an introduction to its physical principles and applications*, *20*.McGraw-Hill New York.

Pierce, C. D. & Moin, P. (1998) A dynamic model for subgrid-scale variance and dissipation rate of a conserved scalar. *Physics of Fluids (1994-present)*, 10(12), 3041-3044.

Pierce, C. D. & Moin, P. (2004) Progress-variable approach for large-eddy simulation of non-premixed turbulent combustion. *Journal of Fluid Mechanics*, 504, 73-97.

Pitsch, H. (2006) Large-eddy simulation of turbulent combustion. *Annu. Rev. Fluid Mech.*, 38, 453-482.

Poinsot, T., Candel, S., Esposito, E., Lang, W. & Bourienne, F. (1989) Suppression of combustion instabilities by active control. *Journal of Propulsion and Power*, 5(1), 14-20.

Poinsot, T. J., amp & Lelef, S. K. (1992) Boundary conditions for direct simulations of compressible viscous flows. *Journal of Computational Physics*, 101(1), 104-129.

Pope, S. B. (1975) A more general effective-viscosity hypothesis. *Journal of Fluid Mechanics*, 72(02), 331-340.

Proscia, W. & Jones, C. D. (2007) Acoustic liner with bypass cooling. Google Patents- US 7311175 B2.

Putnam, A. A. & Dennis, W. R. (1953) A study of burner oscillations of the organ-pipe type. *Trans. ASME*, 75(1), 15-28.

R.Kabral, T. E. (2014) Determination of Liner Impedance under High Temperature and Grazing Flow Conditions, *20th AIAA/CEAS Aeroacoustics Conference*. Atlanta, GA, 16 June -20 June 2014. American Institute of Aeronautics and Astronautics.

Rademaker, E. R., van der Wal, H. M. M. & Geurts, E. G. M. (2011) *Hot-stream in-situ acoustic impedance measurements on various air-filled cavity and porous liners*. Available online: http://reports.nlr.nl:8080/xmlui/bitstream/handle/10921/213/TP-2009-142.pdf?sequence=1 [Accessed 5/09/2016].

Rao, K. N. & Munjal, M. L. (1986) Experimental evaluation of impedance of perforates with grazing flow. *Journal of Sound and Vibration*, 108(2), 283-295.

Rayleigh, J. W. S. (1878) The explanation of certain acoustical phenomena. *Nature*, 18(455), 319-321.

Rayleigh, L. (1940) Theory of Sound, Vol. II, 322 i. Macmillan.

Rice, E. J. (1971) *A model for the acoustic impedance of a perforated plate liner with multiple frequency excitation*. Cleveland, OH, United States: Center, N. L. R. Available online: https://ntrs.nasa.gov/search.jsp?R=19720004979 [Accessed 8/10/2016].

Rice, E. J. (1976) Theoretical study of the acoustic impedance of orifices in the presence of a steady grazing flow. *The Journal of the Acoustical Society of America*, 59(S1), S32-S32.

Rodi, W. (1997) Comparison of LES and RANS calculations of the flow around bluff bodies. *Journal of Wind Engineering and Industrial Aerodynamics*, 69, 55-75.

Ronneberger, D. (1972) The acoustical impedance of holes in the wall of flow ducts. *Journal of Sound and Vibration*, 24(1), 133-150.

Roshko, A. (1961) Experiments on the flow past a circular cylinder at very high Reynolds number. *Journal of Fluid Mechanics*, 10(03), 345-356.

Roux, S., Lartigue, G., Poinsot, T., Meier, U. & Bérat, C. (2005) Studies of mean and unsteady flow in a swirled combustor using experiments, acoustic analysis, and large eddy simulations. *Combustion and Flame*, 141(1), 40-54.

Rupp, J., Carrotte, J. & Macquisten, M. (2012) The use of perforated damping liners in aero gas turbine combustion systems. *Journal of Engineering for Gas Turbines and Power*, 134(7), 071502.

Sadiki, A. & Janicka, J. (2006) Unsteady methods (URANS and LES) for simulation of combustion systems. *International Journal of Thermal Sciences*, 45(8), 760-773.

Scarpato, A. (2014) *Linear and nonlinear analysis of the acoustic response of perforated plates traversed by a bias flow*École Centrale Paris. Available online: https://tel.archives-ouvertes.fr/tel-01126834/document [Accessed 4/7/2016].

Scarpato, A., Ducruix, S. & Schuller, T. (2013) Optimal and off-design operations of acoustic dampers using perforated plates backed by a cavity. *Journal of Sound and Vibration*, 332(20), 4856-4875.

Scarpato, A., Tran, N., Ducruix, S. & Schuller, T. (2012) Modeling the damping properties of perforated screens traversed by a bias flow and backed by a cavity at low Strouhal number. *Journal of Sound and Vibration*, 331(2), 276-290.

Schmitt, F. G. (2007) About Boussinesq's turbulent viscosity hypothesis: historical remarks and a direct evaluation of its validity. *Comptes Rendus Mécanique*, 335(9), 617-627.

Schmitt, P., Poinsot, T., Schuermans, B. & Geigle, K. P. (2007) Large-eddy simulation and experimental study of heat transfer, nitric oxide emissions and combustion instability in a swirled turbulent high-pressure burner. *Journal of Fluid Mechanics*, 570, 17-46.

Scotti, A., Meneveau, C. & Fatica, M. (1997) Dynamic Smagorinsky model on anisotropic grids. *Physics of Fluids (1994-present)*, 9(6), 1856-1858.

Selle, L., Lartigue, G., Poinsot, T., Koch, R., Schildmacher, K. U., Krebs, W., Prade, B., Kaufmann, P. & Veynante, D. (2004a) Compressible large eddy simulation of turbulent combustion in complex geometry on unstructured meshes. *Combustion and Flame*, 137(4), 489-505.

Selle, L., Nicoud, F. & Poinsot, T. (2004b) Actual impedance of nonreflecting boundary conditions: Implications for computation of resonators. *AIAA Journal*, 42(5), 958-964.

Seybert, A. F. & Ross, D. F. (1977) Experimental determination of acoustic properties using a two - microphone random - excitation technique. *the Journal of the Acoustical Society of America*, 61(5), 1362-1370.

Singh, N. K. (2012) *Large eddy simulation of acoustic propagation in turbulent flow through ducts and mufflers*. Ph.D Thesis University of Hull.

Sivian, L. J. (1935) Acoustic impedance of small orifices. *The Journal of the Acoustical Society of America*, 7(2), 94-101.

Smagorinsky, J. (1963) General circulation experiments with the primitive equations: I. the basic experiment*. *Monthly weather review*, 91(3), 99-164.

Smith, P. L. & Van Winkle, M. (1958) Discharge coefficients through perforated plates at Reynolds numbers of 400 to 3,000. *AIChE Journal*, 4(3), 266-268.

Spalart, P. R. & Allmaras, S. R. (1992) A one equation turbulence model for aerodinamic flows, *30th Aerospace Sciences Meeting and Exhibit*. Reno,USA.

Stankowski, T. P., MacManus, D. G., Sheaf, C. T. & Grech, N. (2016) Aerodynamics of aero-engine installation, *54th AIAA Aerospace Sciences Meeting*. San Diego, California, USA, 2016.

Steele, R. C., Cowell, L. H., Cannon, S. M. & Smith, C. E. (2000) Passive control of combustion instability in lean premixed combustors. *Journal of Engineering for Gas Turbines and Power*, 122(3), V002T02A004.

Sullivan, J. W. (1979) A method for modeling perforated tube muffler components. I. Theory. *The Journal of the Acoustical Society of America*, 66(3), 772-778.

Sun, X., Jing, X., Zhang, H. & Shi, Y. (2002) Effect of grazing–bias flow interaction on acoustic impedance of perforated plates. *Journal of Sound and Vibration*, 254(3), 557-573.

Sutera, S. P. & Skalak, R. (1993) The history of Poiseuille's law. *Annual Review of Fluid Mechanics*, 25(1), 1-20.

Syed, A. A., Yu, J., Kwan, H. W., Chien, E. & Jones, M. G. (2002) *The steady flow resistance of perforated sheet materials in high speed grazing flows*. Cincinnati, OH United States: NASA. Available online: https://ntrs.nasa.gov/search.jsp?R=20020065231 [Accessed 25/10/2019].

Tayong, R., Dupont, T. & Leclaire, P. (2010) On the variations of acoustic absorption peak with particle velocity in micro-perforated panels at high level of excitation. *The Journal of the Acoustical Society of America*, 127(5), 2875-2882.

Tidjani, N., Martin, G. H., Schott, G. & Grienche, G. (2001) Développement d'une technologie de chambre de combustion à faibles émissions polluantes pour turbomachines de petite et moyenne puissances, *NOXCONF 2001. International Meeting.* 2001.

Tonon, D., Moers, E. M. T. & Hirschberg, A. (2013) Quasi-steady acoustic response of wall perforations subject to a grazing-bias flow combination. *Journal of Sound and Vibration*, 332(7), 1654-1673.

Versteeg, H. K. & Malalasekera, W. (2007) *An introduction to computational fluid dynamics: the finite volume method*.Pearson Education.

Veynante, D. (2009) Large eddy simulations of turbulent combustion, *Turbulence and Interactions*Springer, 113-138.

Vigran, T. E. (2012) Normal incidence sound transmission loss in impedance tube–Measurement and prediction methods using perforated plates. *Applied Acoustics*, 73(4), 454-459.

Wang, P., Platova, N. A., Fröhlich, J. & Maas, U. (2014) Large Eddy Simulation of the PRECCINSTA burner. *International Journal of Heat and Mass Transfer*, 70, 486-495.

Watson, W., Jones, M. & Parrott, T. (1999) Validation of an impedance eduction method in flow. *AIAA Journal*, 37(7), 818-824.

Watson, W. R. & Jones, M. G. (2013) A comparative study of four impedance eduction methodologies using several test liners. *AIAA Paper*, 2274.

Wilcox, D. C. (1998) *Turbulence modeling for CFD*, *2*.DCW industries La Canada, CA.

Yang, C., Cheng, L. & Pan, J. (2013) Absorption of oblique incidence sound by a finite micro-perforated panel absorber. *The Journal of the Acoustical Society of America*, 133(1), 201-209.

Yunus, A. C. & Cimbala, J. M. (2006) Fluid mechanics: fundamentals and applications. *International Edition, McGraw Hill Publication*, 185-201.

Zhang, Q. & Bodony, D. J. (2012) Numerical investigation and modelling of acoustically excited flow through a circular orifice backed by a hexagonal cavity. *Journal of Fluid Mechanics*, 693, 367-401.

Zhao, D., Ang, L. & Ji, C. Z. (2015) Numerical and experimental investigation of the acoustic damping effect of single-layer perforated liners with joint bias-grazing flow. *Journal of Sound and Vibration*, 342, 152-167.

Zhao, D. & Li, X. Y. (2015) A review of acoustic dampers applied to combustion chambers in aerospace industry. *Progress in Aerospace Sciences*, 74, 114-130.

Zhao, D. & Morgans, A. S. (2009) Tuned passive control of combustion instabilities using multiple Helmholtz resonators. *Journal of Sound and Vibration*, 320(4), 744-757.

Zhong, Z. & Zhao, D. (2012) Time-domain characterization of the acoustic damping of a perforated liner with bias flow. *The Journal of the Acoustical Society of America*, 132(1), 271-281.

Zhu, S., Mizuno, M., Kagawa, Y., Cao, J., Nagano, Y. & Kaya, H. (1999) Creep and Fatigue Behavior in Hi - Nicalon Fiber Reinforced Silicon Carbide Composites at High Temperatures. *Journal of the American Ceramic Society*, 82(1), 117-128.

Zinn, B. T. (1970) A theoretical study of non-linear damping by Helmholtz resonators. *Journal of Sound and Vibration*, 13(3), 347-356.

Zinn, B. T. & Lieuwen, T. C. (2005) Combustion instabilities: Basic concepts. *Combustion Instabilities in Gas Turbine Engines: Operational Experience, Fundamental Mechanisms, and Modeling*, 210, 3-26.